ANISOTROPY IN STRONG GROUND MOTION IN THE 1994 ARTHUR'S PASS EARTHQUAKE

A thesis
submitted in partial fulfilment
of the requirements for the Degree
of
Master of Engineering in Civil Engineering
in the
University of Canterbury
by

Pierre Malan

University of Canterbury
2001

Table of Contents

List of Tables

List of Figures

Abstract

Directivity effects are assessed by examining strong ground motion records from the 1994 Arthur's Pass earthquake in light of evidence presented by past researchers. This thesis focusses primarily on intra site differences in anisotropic ground motion, achieved by analysing different components of ground motion.

Problems are encountered in the selection of a fault plane. It is most likely that the fault plane assumed for analysis is not consistent with the actual fault plane. Despite these problems, some observations of anisotropic behaviour are made at the Arthur's Pass, Flock Hill and Lake Coleridge sites that are consistent with rupture on the assumed fault plane.

The determination of directivity effects is based on analysis of fault normal and fault parallel components of acceleration, velocity and displacement records, in addition to Fourier and response spectra derived from the ground motion acceleration records. A further study is carried out on peak ground accelerations.

Existing directivity research deals primarily with fault normal amplification in forward rupture directivity regions; that is, at sites located in the path of the moving rupture front. The results of a simple model application suggest that in some cases, fault parallel amplification may be significant next to fault planes. This is highlighted in far field Fourier amplitude predictions for the Arthur's Pass Police Station.

Acknowledgements

A work like this is never possible without the aid and assistance of a number of people. Firstly, and most importantly, I must extend my thanks and appreciation to my supervisor, Dr. John Berrill. He sparked my interest in this topic, and guided me on a fascinating journey. Without his support and assistance, this work would not have been possible, and I proffer him my warmest thanks.

No acknowledgement touching upon my time at Canterbury University could be complete without the mention of all of my friends and colleagues, who have supported me during my time in Christchurch. Without them, this work could not have been completed, so thank you for your support. I must also thank my parents for their support and encouragement over the years, and extend them my thanks and appreciation for all that they have done.

1 Introduction

Directivity effects in the 1994 Arthur's Pass earthquake are examined using ground motion records from the event. Directivity effects are important as they have the potential to significantly alter the intensity of shaking at sites around the fault. The agreement of actual Fourier spectra to those predicted by an idealised model of fault rupture is then examined.

Chapter 1 explains what directivity effects are, and the effects that they have at sites. A discussion of New Zealand seismic hazard models is followed by a summary of empirical models predicting directivity effects. Chapter 2 discusses the 1994 Arthur's Pass fault rupture with emphasis on the problems of fixing the fault plane of the rupture. Chapters 3 to 7 analyse and discuss ground motion recorded at three sites during the earthquake. Chapter 8 presents a proposed rupture model, and applies it to the fault plane selected in Chapter 2. The results generated are then compared to those recorded.

1.1 Directivity effects

The movement of a rupture front along a fault plane causes interference in the seismic waves generated during the strain release process. Sites located in the path of the rupture front experience short, intense shaking due to constructive interference of the shear waves. The increase in shaking intensity due to the constructive interference of shear waves is called forward rupture directivity, and has been noticed by researchers for a number of years (Somerville, 1996; Berrill, 1975). Sites that experience these stronger intensities are located in a forward rupture directivity zone. Sites behind the propagating rupture, in the backward directivity zone, experience longer and less intense ground motion. Forward rupture directivity effects increase intensities in the fault normal direction. The fault normal direction is at right angles to the direction of rupture propagation, and is shown in Figure 1-1.

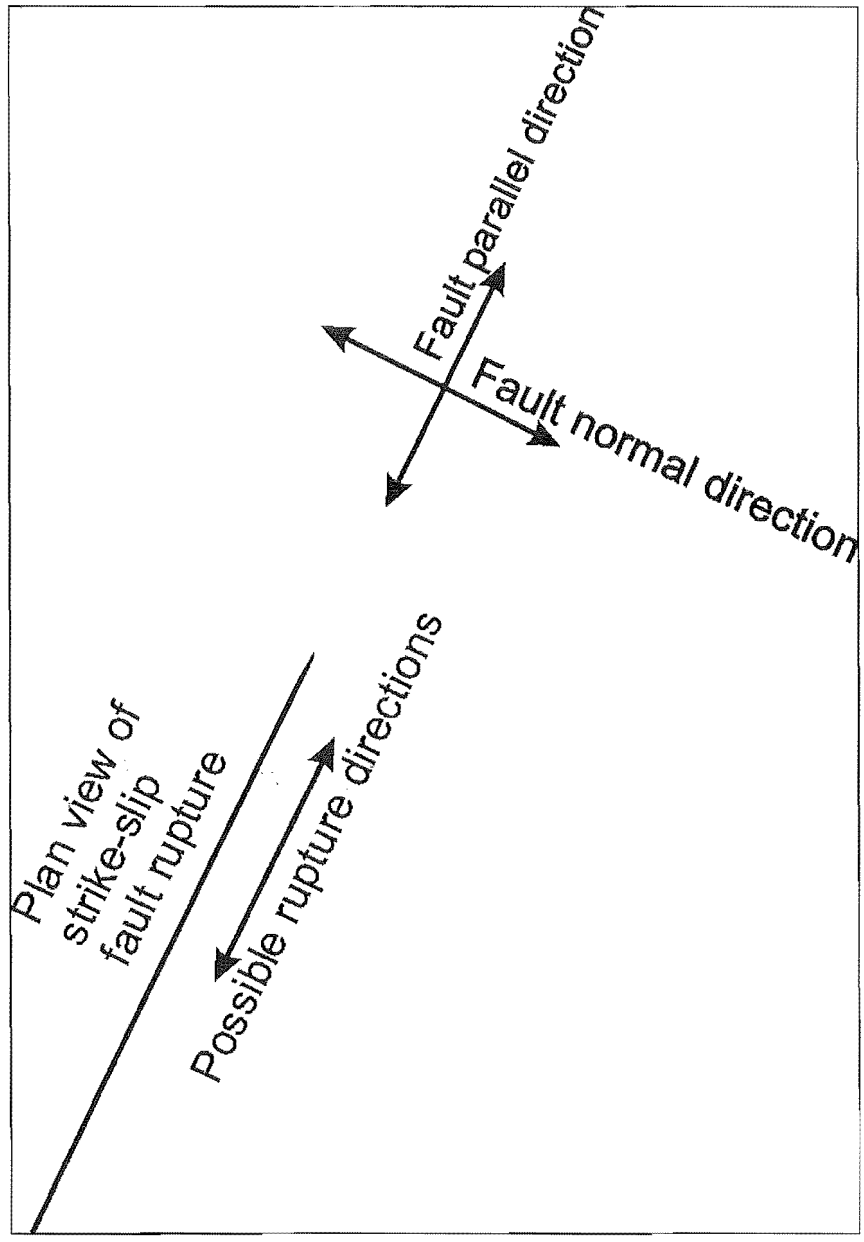

Figure 1-1 Definition of fault normal (FN) and fault parallel (FP) directions

Figure 1-2 shows a plan view of strike-slip faulting during the 1992 Landers earthquake. Recordings from this earthquake are used by Somerville et al. (1997) as examples both of forward and backward directivity effects. Fault normal components of ground motion at two sites near the rupture surface are presented in the figure. The Lucerne record shows forward rupture directivity effects with a high peak velocity (136 cm/s) at the beginning of the record. The Joshua Tree record (peak velocity 43 cm/s) was located in the backward rupture directivity zone and experienced significantly longer and less intense shaking. The differing durations and intensities

at the two sites are due to the position of the sites with respect to the fault plane and the direction of rupture. Section 1.2 summarises the effects of directivity at sites.

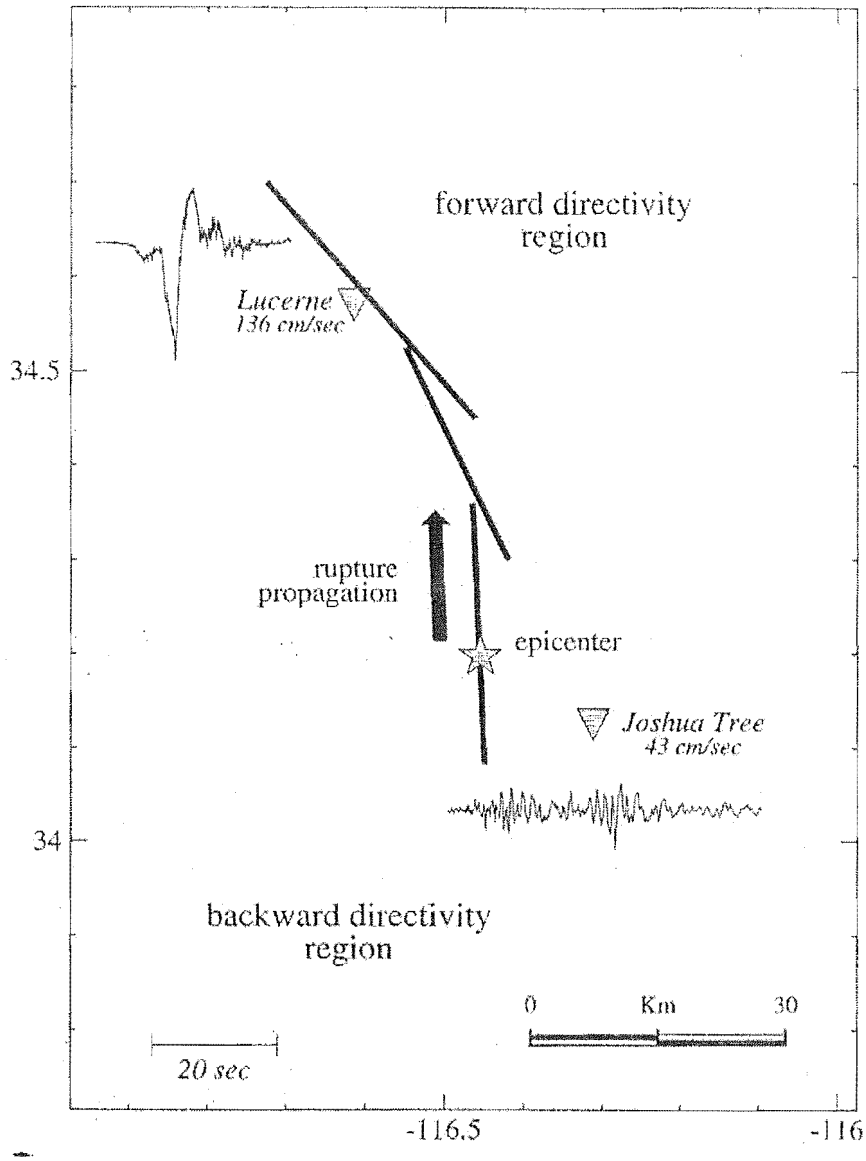

Figure 1-2 1992 Landers earthquake showing regions affected by directivity

Source: Somerville et al. (1997)

As the term is used in this thesis, directivity effects are defined as the intensity variations in horizontal ground motion due to interference caused by movement of a propagating rupture front. Intensity variation in the vertical direction caused by vertical rupture movement is not considered. Seismic waves in the vertical direction are refracted and reflected as they pass through material layering that is inevitably present at sites. This wave alteration affects the interference caused by vertical

rupture propagation and makes isolation of directional effects in a vertical sense very difficult (Lay and Wallace, 1995).

Rupture directivity effects are period dependent (Kasahara 1981; Lay and Wallace, 1995; Somerville, 1996). This dependence implies that the size of both the forward and backward rupture directivity zones vary with varying period. This period dependence also adds another level of complexity to the problem of isolating directional effects in ground motion. Site effects can create variations in intensity that can easily be mistaken for forward rupture directivity effects. The effects of site geometry on ground motion is discussed in section 1.5.3.

The level of interference of seismic waves released during a fault rupture is dependent on the relative speed of rupture and shear wave propagation (Kasahara, 1981; Lay and Wallace, 1995). As the two speeds approach each other the effects of shear wave interference become significant. The theory behind these effects is discussed in Chapter 8.

1.2 Directivity effects in past ruptures

Directivity usually affects both the fault normal (FN) and fault parallel (FP) components of various parameters. (FN and FP directions were shown in Figure 1-1) Intra-site variations in the two directions are highlighted by:

- shape of the acceleration, velocity and displacement ground motion plots
- peak values of ground motion parameters
- duration of strong ground motion (Duration defined in Section 1.2.1)
- differences in Fourier spectra
- differences in response spectra

These differences are also present between sites (inter-site differences). This thesis chiefly examines the intra-site differences in an attempt to isolate directional effects.

The significance of directivity effects can be seen in the comparison of the 1994 Northridge and 1995 Kobe earthquakes. The Northridge rupture was primarily a thrust event that ruptured from underneath the city centre toward a sparsely populated

region north of the city. The Kobe event was a strike-slip rupture, of similar magnitude to Northridge, where the rupture direction was towards the city centre. The Kobe rupture geometry meant that the densely populated city centre was located in the forward rupture directivity zone. High intensity shaking caused by forward rupture directivity effects became significant in the urban centre and resulted in damage costs around 10 times those of Northridge (Somerville, 1996).

1.2.1 Effects of directivity on duration

The duration of strong motion varies significantly in the near field of an earthquake. Sites located in forward rupture zones experience a shorter ground motion duration than other sites. Sites in the backward directivity zone perceive a longer and less intense period of ground motion. Sites that have constant amounts of energy passing through them can experience significant variations in intensity due to differences in perceived duration. Perceived duration is dependant on the location of the site with respect to the fault plane and direction of fault propagation (Kasahara, 1981). The quantification of this perceived duration variation is discussed in Chapter 8.

Strong ground motion duration has been defined in a number of different ways (Kramer, 1996). The definition used for this thesis is the duration between 5% and 95% of the energy passing through the site.

1.2.2 Forward rupture directivity effects on ground motion time histories

Forward rupture directivity effects can be seen in the time histories of ground motion that are presented in Figure 1-3, time histories recorded during the 1994 Northridge earthquake. The 'V' represents the vertical direction. The recording site was located in the path of rupture propagation and shows characteristic shapes associated with forward rupture directivity effects. Both the acceleration and velocity records show a characteristic peak-trough shape in the fault normal component as the shear waves

arrive. The timing and shape of the peak-trough is indicative of forward rupture directivity effects.

Another example of forward rupture directivity is the Parkfield acceleration record, shown in Figure 1-4. The earthquake, magnitude 5.7 generated a peak acceleration in the path of the rupture of nearly 0.5g. This peak acceleration was of a similar magnitude to that generated by the Arthur's Pass earthquake, even though the Parkfield earthquake released only about a tenth of the energy. These records show the potential of rupture directivity effects to significantly affect acceleration recordings.

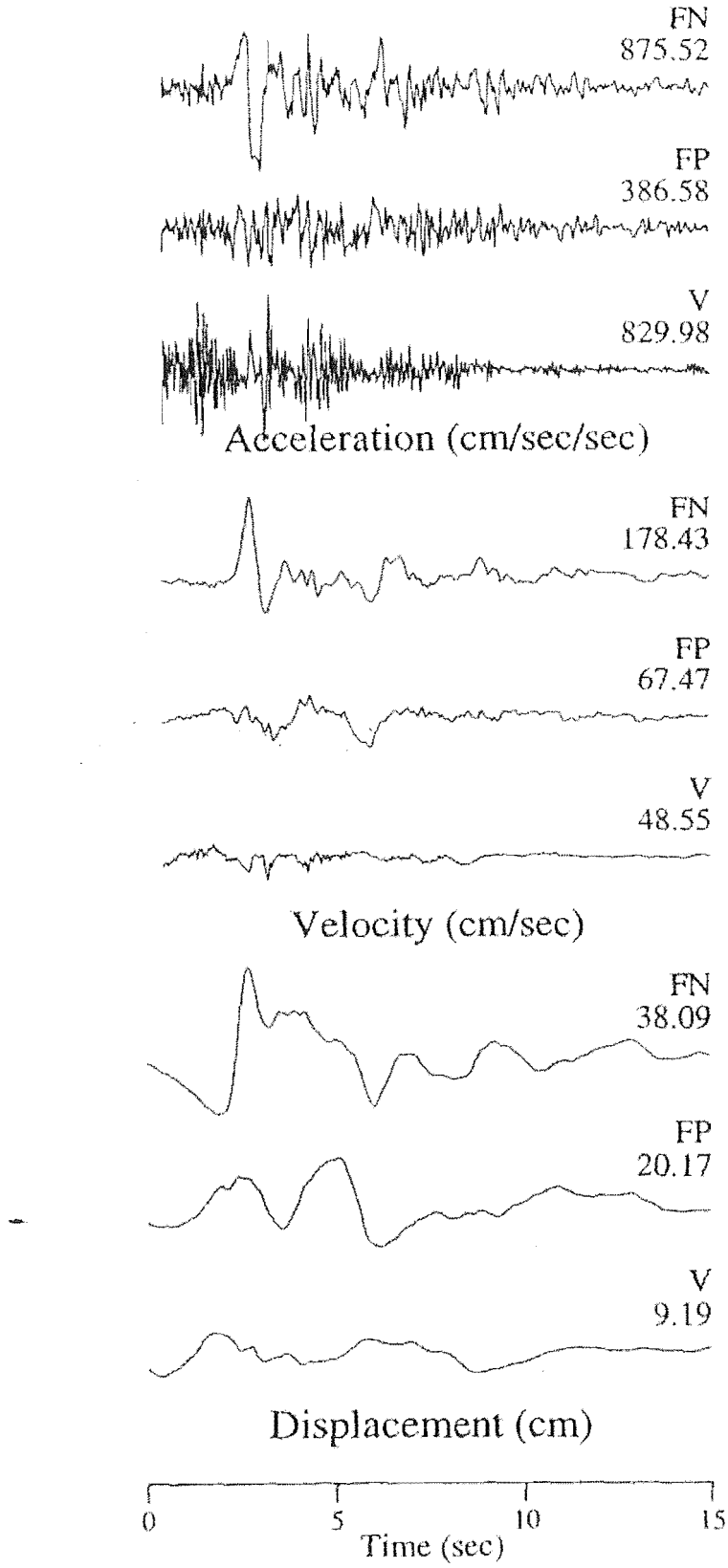

Figure 1-3 Ground motion affected by forward rupture directivity, recorded during the 1994 Northridge earthquake at the Rinaldi site. FN = Fault Normal, FP = Fault Parallel, V = Vertical.

Source: Somerville (1996)

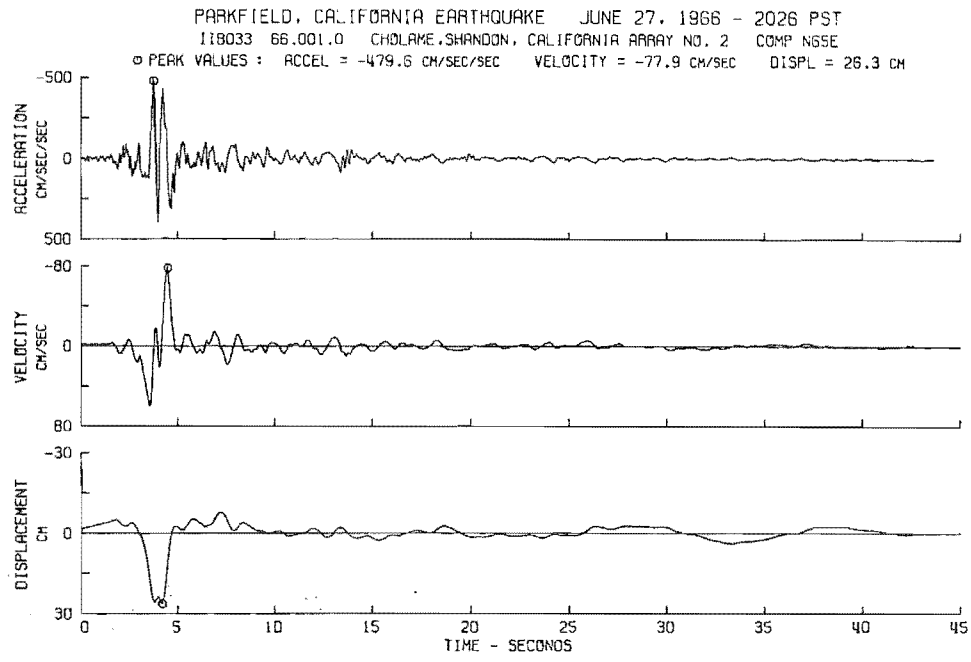

Figure 1-4 Parkfield record demonstrating forward rupture directivity

1.2.3 Forward rupture directivity effects on response spectra

In Figure 1-5, response spectra generated from ground motion records from 4 sites around the 1994 Northridge rupture surface are presented. Amplification of the response spectra fault normal components can be seen in the three sites located in forward rupture directivity zones: Newhall, Rinaldi and Sylmar. A neutral directivity site, Arleta, is presented for comparison. Different periods clearly exhibit varying levels of directivity effects. The increase in spectral acceleration in the fault normal component is consistent with the effects noted in section 1.2.2. Chapter 8 discusses the reasons for period dependence of directivity effects.

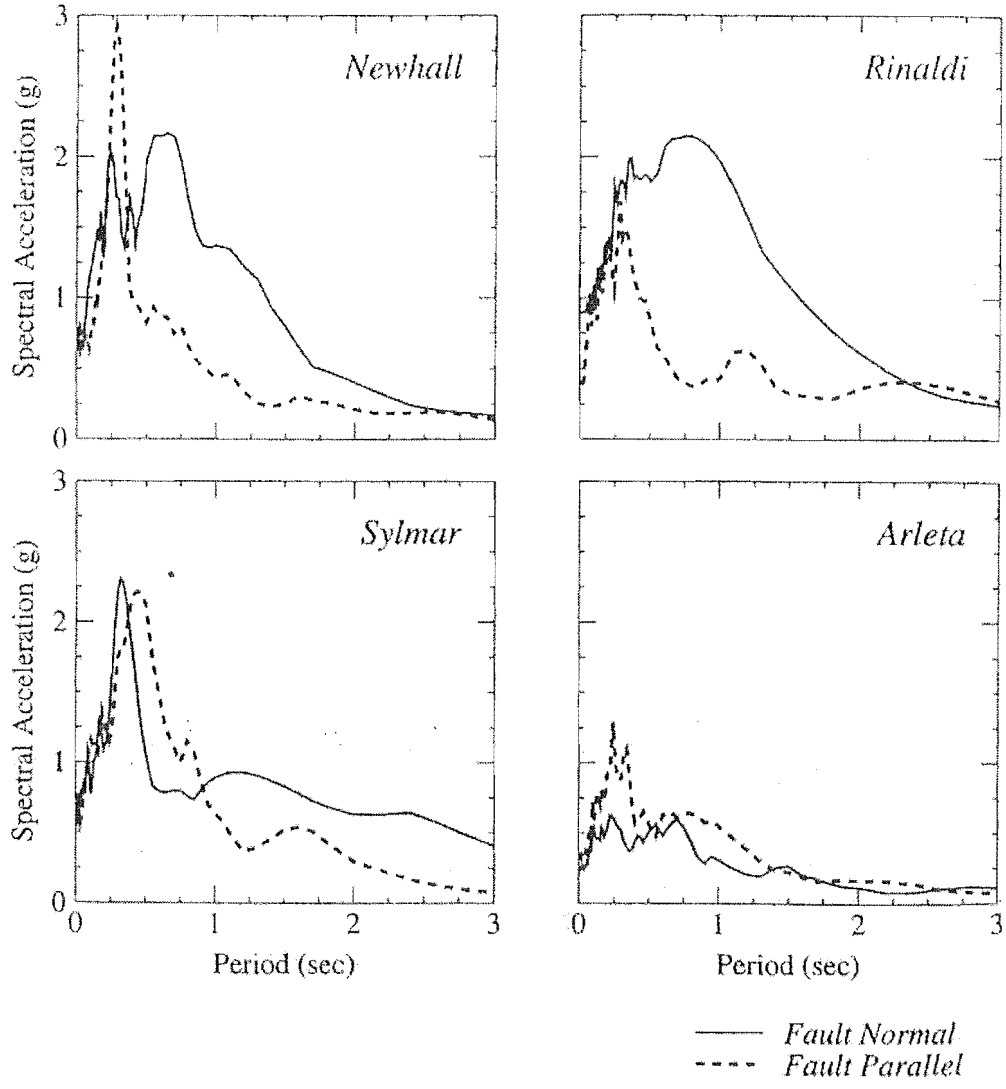

Figure 1-5 Effects of directivity in the 1994 Northridge Earthquake

(Source: Somerville, 1996)

1.3 A history of seismic hazard in New Zealand

Initial seismic hazard assessments of New Zealand were based on the analytical approach first developed by Cornell (1968). Peek (1980) considered New Zealand as 17 regions with varying seismicity with 'fuzzified' boundaries separating them. Smith and Berryman (1983) divided New Zealand into 15 zones of varying seismicity. The seismic hazard at a site therefore varied depending on the zone the site was located in. Zone seismicity was based on historical records and knowledge

of local geology. Based on Smith and Berryman's (1983) seismicity model, and a modified version of Katayama's attenuation model, Matuschka et al. (1985) published a series of maps that showed peak spectral accelerations for a given return period. The peak spectral accelerations were used as the basis for the New Zealand Standard, NZS4203:1992 (Standards Association of New Zealand, 1992), the code of practice for general structural design and design loadings of buildings. All of the above analyses were based on an assumption of homogenous seismicity within delineated zones. Earthquakes are represented in these hazard models as point sources - no allowance is made for ruptures to have a finite length. The most recent seismic hazard model for New Zealand is a probabilistic hazard model developed by Stirling et al. (1999). This model represents seismicity in New Zealand as a combination of point sources representing background seismicity, and known faults. Directivity effects were not considered in the hazard analysis.

1.3.1 New Zealand finite fault length models

Both Smith (1995) and Dowrick and Rhoades (1999) have attempted to quantify near field effects around rupture surfaces by considering finite rupture lengths. Smith assumed an equal rate of energy release over the entire fault. He modelled a series of small point source earthquakes with equal energy distributed over the rupture length. The energy released by the small earthquakes sums to give the energy released during the actual event. Directional effects were not considered.

Dowrick and Rhoades (1999) analysed the ellipticity of modified Mercalli intensity (MMI) isoseismals around New Zealand rupture planes. They noted that isoseismals had pronounced ellipticity around defined fault planes and that the orientation of the principal axis was often along the N40E/S40W bearing, parallel to the strike of the Pacific and Australian plate interaction.

Isoseismal analysis captures the gross characteristics of near fault geometry by representing felt intensity, but, by it's nature, cannot represent anisotropy within recorded ground motion at a site. Isoseimals can represent the intensity variation between sites, but not the ground motion anisotropy within a site that this thesis

examines. Isoseismals also do not clearly show any coherency variation with period that may be present. For these reasons, isoseimal analysis is not considered in this analysis.

1.3.2 Empirical models of directivity effects

Two current models represent the effects of forward rupture directivity at sites. Somerville (1996) presented an empirical model of the effects of forward rupture directivity on response spectra. The model uses epicentral distance, magnitude and period to generate a ratio between fault normal response and average response. Effects were limited to a distance of 50km. No duration effects, or effects on motion in any direction but the fault normal were considered. Near fault geometry was not considered in Somerville's (1996) analysis.

Somerville et al. (1997) published a model affecting three parameters of ground motion:

- average horizontal response spectral acceleration
- average duration of the two horizontal acceleration time histories
- ratio of strike-normal to strike-parallel spectral accelerations

The Somerville et al. (1997) model was designed for use with Abrahamson and Silva's (1997) response spectral acceleration model. It is, however, presented so that it can be used in conjunction with any model that predicts response spectra. At distances of less than 20km the model alters the duration. Amplitudes are altered at distances of less than 50km. Somerville et al. (1997) considered that only periods greater than 0.5 seconds would be susceptible to rupture directivity effects.

1.3.3 Haskell fault rupture model

The Haskell model (Kasahara, 1981; Lay and Wallace, 1995) is a frequency dependent model that predicts Fourier amplitudes generated by a moving fault rupture

with a finite rise time. Chapter 8 describes the application of a modified version of the Haskell model on the assumed fault plane that is selected in Chapter 2.

1.4 Limitations of finite fault length models in seismic hazard

The accurate prediction of directivity effects at a site is clearly dependent on the geometry of the fault plane. Fault plane prediction is therefore critical in the assessment of seismic hazard at sites. An example of a major fault plane that was unknown prior to rupture is the 1994 Northridge surface. In other cases, like the Wellington and Alpine Faults, the fault planes are well defined (Van Dissen and Berryman, 1990; Yetton et al., 1998), and for these two cases it is possible to make some quantifiable estimate of directivity effects at a site.

1.4.1 Alpine Fault

Earthquakes on the Alpine Fault are expected to have a moment-magnitude of around 8.0 (Yetton et al., 1998) The Alpine Fault is primarily strike-slip and is over 600 km long. Directivity effects will be significant during a rupture. While directivity effects are expected to significantly alter ground motion felt around the Alpine Fault, the implications of the increased seismic hazard are not as significant as an increase in hazard around the Wellington Fault. The reason for this is that the Alpine fault is located in an area with low population density, where the potential damage cost is significantly lower than that of Wellington area.

1.4.2 Wellington Fault

The central business district (CBD) of Wellington is located in the path of the fault rupture, and close to the fault plane. This geometry fulfils criteria for significant forward rupture effects to be experienced at sites in the densely populated central city. Ruptures on the Wellington Fault are expected to generate earthquakes with

magnitudes of around M_s = 7.4-7.5 (Van Dissen et al., 1990; Van Dissen et al., 1992). The effects of directivity are not currently considered in routine assessments of seismic hazard in central Wellington.

1.4.3 Knowledge of rupture surfaces

While finite fault length models can generate precise predictions of anisotropic shaking at a site of interest, they are not necessarily accurate. Most differences between predicted and actual ground motion at a site can be attributed to 4 elements, discussed in sections 1.4.3.1 – 1.4.3.4.

- The accuracy of fault surface prediction,
- The random nature of the fault rupture progression,
- Localised site effects
- The varying travel paths of seismic waves.

1.4.3.1 Fault surface prediction

Mapping of potential fault surfaces is extremely important in the accurate assessment of seismic hazard. Figure 1-6 shows the Institute of Geological and Nuclear Sciences, (1999) assessment of expected fault rupture types in areas of New Zealand.

Generally, thrust/reverse events are more difficult to detect than strike-slip as the displacements introduced during an earthquake event are primarily vertical, and hence more susceptible to modification by slope processes (Pettinga, 2000). Thrust/reverse events are more damaging than either strike/slip or normal faults releasing a similar amount of energy (Archuleta, 1999). For New Zealand, the regions associated with certain types of faulting are presented in Figure 1-6 (IGNS study group, 1999). Seismic hazard in regions expected to experience thrust/reverse faulting could be affected by the dual effect of increased difficulty in fault detection, and the increased damage caused by this type of earthquake. The potential effect of this combination could be currently underpredicted by current seismic hazard assessments.

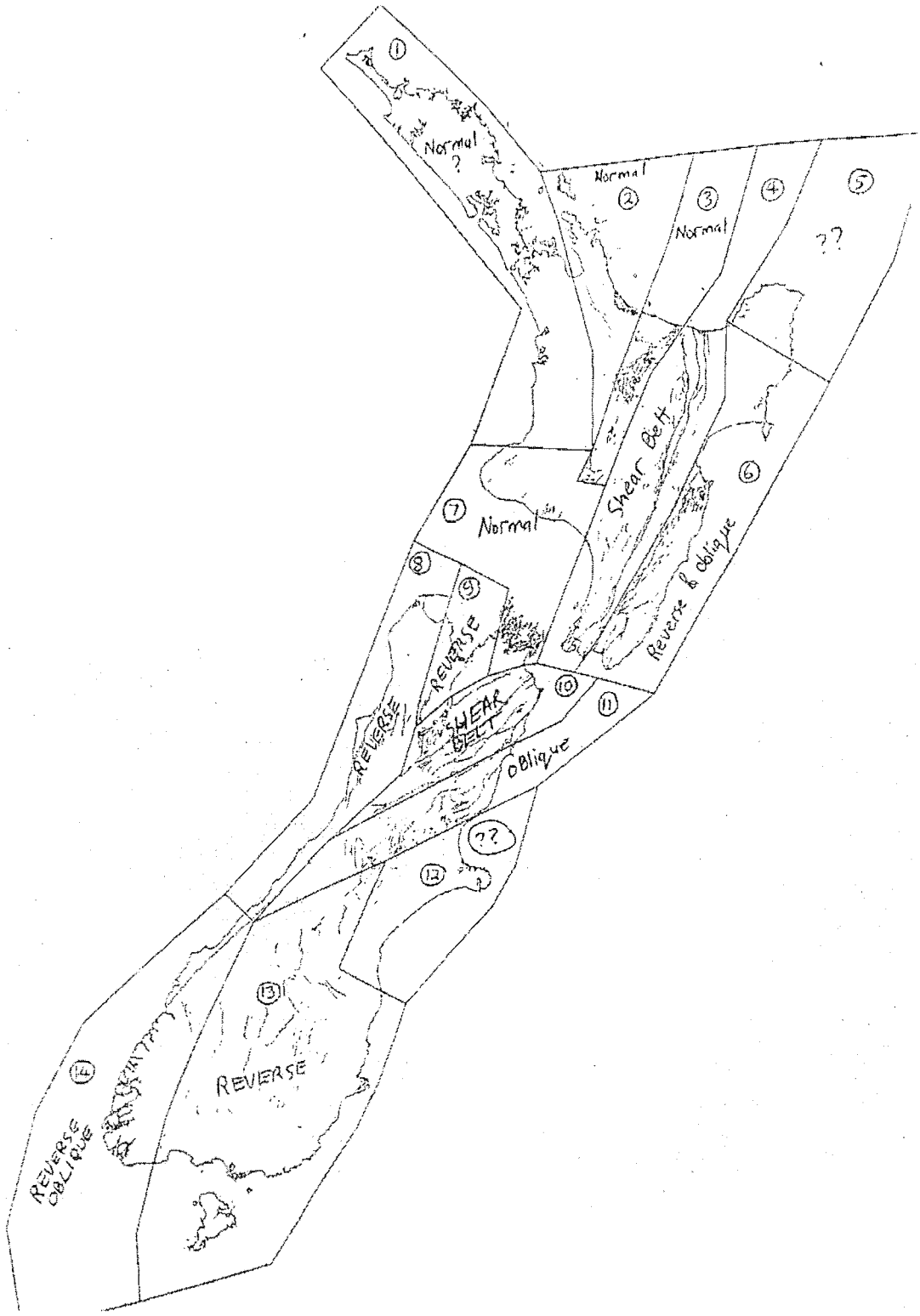

Figure 1-6 IGNS (1999) assessment of likely fault type locations in New Zealand

Source: IGNS study group (1999)

1.4.3.2 Random nature of fault rupture progression

The finite fault length models considered in this thesis assume fault ruptures to be smooth progressions along the slip surface. This assumption is known to be incorrect (Kasahara, 1981; Lay and Wallace, 1995). The actual progression of a fault rupture is a stop-start progression of stress release. Modelling this progression is extremely difficult in past ruptures and becomes almost impossible when a future rupture is being predicted. The stop-start nature of fault rupture progression also creates a significant component of the high frequencies generated during the rupture process as small areas on the fault plane rupture with short rise times. Asperities on the fault plane generate variations in energy release along the fault that are not considered in standard models. These asperities are significant in the near field (Kramer, 1996)

1.4.3.3 Local site effects

Local site conditions can have a significant impact on ground motion. Seismic waves at a site may be affected by the geometry of the surficial layers. Such geometry will have an impact on the recorded ground motion at the site. Sites close to the fault can respond in nonlinear fashion to the large strains induced by the earthquake motion. The significance of site effects on ground motion is discussed in section 1.5.3.

1.4.3.4 Differing travel paths

Differing seismic wave travel paths between the source and the site introduce a significant level of randomness into any ground motion recording. The effect of these varying travel paths is extremely difficult to incorporate into predictive models. The effects of the varying travel paths of seismic waves increase with epicentral distance.

1.5 Directivity effects and site specific seismic hazard

Two methods of seismic hazard assessment that considers individual faults close to sites are in current use. These are:

- Deterministic seismic hazard assessment (DSHA)
- Probabilistic seismic hazard assessment (PSHA)

The effects of directivity can be incorporated into either type of assessment, and this process is discussed in sections 1.5.1 and 1.5.2. Note that the directivity effects considered below pertain chiefly to inter-site differences, and not to anisotropic ground motion within a site.

1.5.1 Consideration of directivity effects in a PSHA

After selection of a fault source in a PSHA, a recurrence relationship for the source is defined. This recurrence relationship consists of a rate at which an earthquake of given magnitude will be exceeded. The rupture magnitude is independent of the site being considered. The attenuation model used in the analysis relates the shaking intensity at a site and the earthquake magnitude.

Since the PSHA considers the combination of magnitude distributions and an attenuation relationship, it would be possible to include the distribution of the earthquake rupture direction. The rupture direction, as a result of directivity effects, may have an effect on shaking intensity at the selected site. Quantifying these effects would allow the strength of shaking to be directly related to the magnitude and direction of rupture, and hence for directivity effects to be included in a PSHA.

If the inclusion of directivity effects in a PSHA were developed further, it would be appropriate to consider these effects where a well defined fault plane is a primary contributor to seismic hazard. The Wellington region, discussed in Section 1.4.2, is one area where these conditions are satisfied.

1.5.2 Consideration of directivity effects in a DSHA

Directivity effects can be considered in a DSHA provided that a fault plane is adequately defined. Since a DSHA considers the maximum possible earthquake on a fault, it is possible to include the effects of rupture direction in the effect felt at sites. The rupture direction that generates the largest response at the site will be the direction that is selected for use in the modelling procedure. The effect at the site can be quantified by the use of a number of models available (eg Somerville, 1996; Somerville et al., 1997). The selection of faults for use in a DSHA can be based on the results of a PSHA with hazard deaggregation.

DSHA can be used to generate maximum credible shaking levels at sites where important structures are to be built. Directivity effects may cause anisotropic shaking at sites. Intensity variations between the sites due to rupture geometry can be quantified and considered in the hazard analysis. This is based on the selection of an appropriate, accurate fault plane, a problem addressed in section 1.4.3.1.

1.5.3 Site effects

A significant source of anisotropy in site response is often due to the properties of material at and around the site of interest (Kramer, 1996). These two-dimensional site effects are not usually considered in models of fault rupture. The Greymouth record presented in Chapter 7 demonstrates that sites can exhibit significant anisotropy in recorded ground motion. While anisotropy at sites can be attributed to the effects of site geometry, the results presented in Chapter 7 suggest that this is not the case at Greymouth. The site effects considered are presented in more detail in Chapter 7.

2 The 18 June 1994 Arthur's Pass earthquake

2.1 Geological background

Arthur's Pass is in the heart of the Southern Alps of New Zealand. The Alps are one of the physical manifestations of the interaction between the Pacific and Australian plates. The plate moves in the order of 40mm/year with components of movement both along, and normal to, the plate boundaries. Northeast of the South Island, the Pacific Plate is subducted by the Australian Plate. To the Southwest of the island, below Haast and Fiordland, the Pacific Plate subducts the Australian Plate. As the crustal material changes from oceanic (permitting subduction) to continental (which does not) extensive uplift occurs in the centre of the island. Uplift along the plate boundary is in the order of 50 mm/year (Yetton et al., 1998).

In the central South Island, strain built up by movement along the plate boundaries is mainly relieved by the Alpine Fault, the largest fault in the area. The Alpine Fault is 650 km long and extends from south of Milford Sound on the Tasman coast to north of Blenheim on the Pacific coast (Yetton et al., 1998). Figure 2-1 shows the Alpine Fault, the only major fault on the West Coast between Inchbonnie and Milford Sound. North of Inchbonnie the fault splits into a number of faults bounded by the Hope Fault and the main branch of the Alpine Fault. These subsidiary faults all contribute to alleviating the strain built up by the relative motion of the plates.

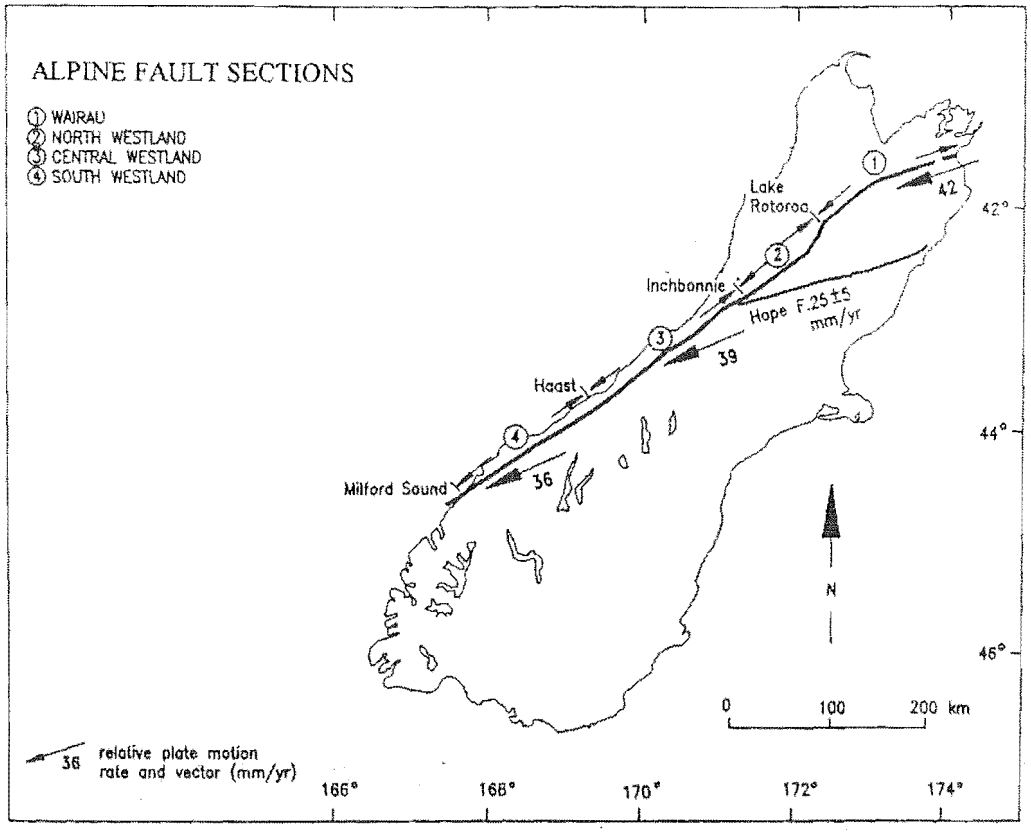

Figure 2-1 Alpine fault and plate movement rates

Source: Yetton et al. (1998)

Historical ruptures on the Alpine Fault have been estimated to have a moment-magnitude of approximately 8.0 (Yetton et al., 1998). The fault, when it ruptures, is expected to cause severe shaking throughout the South Island, with landslides, river siltation and significant structural damage expected.

2.2 Rupture event

The Arthur's Pass rupture event of 18 June 1994 had a moment magnitude of 6.7. Figure 2-2 shows the main shock epicentre located 25 km SE of the Alpine Fault, and the initial Harvard Moment-Tensor (HMT) assessment of the rupture. The earthquake was the largest in the South Island for 65 years (Robinson et al. 1995). Aftershocks from the 1994 rupture were generally oriented in a zone at right angles to the Alpine Fault, with a strike of 343°. Figures 2-2 and 2-3 show the region that the earthquake occurred in, bounded on one side by the Alpine Fault, and the Harper Fault on the

other. Prior to the rupture, the region was not thought to be seismically active (Abercrombie et al., 1998). Portable accelerometers installed in the region immediately after the event recorded information used to deduce aftershock locations (Robinson and McGinty. 1998). Further work has been done by Abercrombie et al. (1998) relocating the aftershocks using both 1-D and 3-D soil models. These relocated aftershocks were used in an assessment of rupture mechanics (Abercrombie et al., 1998; Robinson and McGinty, 1998).

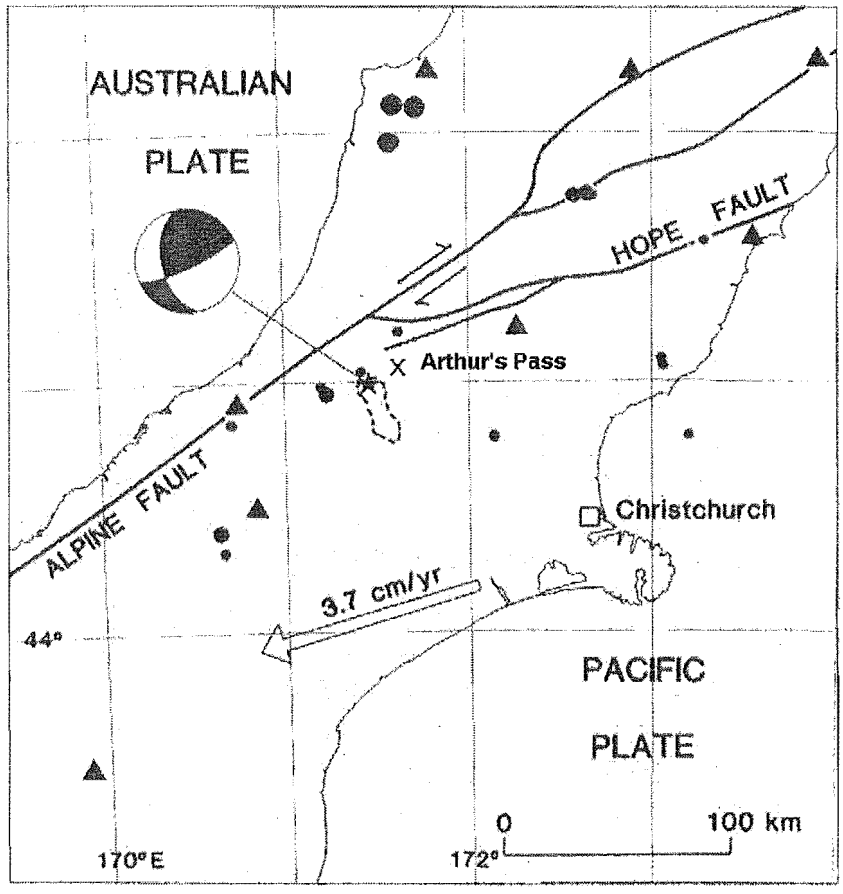

Figure 2-2 Arthur's Pass earthquake showing 1995 HMT solution and epicentre. The star is the epicentre of the 1994 earthquake; the dashed line represents the area of aftershock activity; circles represent earthquakes with a magnitude of 5.0 or greater in the decade prior to the 1994 rupture. Triangles are permanent stations of the New Zealand Seismograph network, and the 'X' denotes the Arthur's Pass township

Source: Robinson et al. (1995)

Figure 2-3 shows the recorded aftershocks that occurred in the region after the event. The largest of these was an M_L = 6.1 strike-slip event that was located southeast of the aftershock sequence. Robinson et al. (1998) consider that the 1995 Cass earthquake

event may have been induced by stress changes associated with the 1994 rupture event.

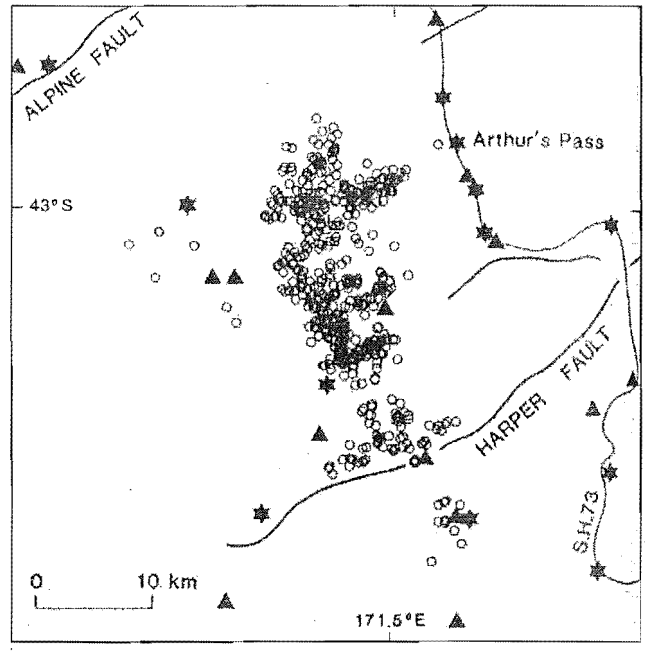

Figure 2-3 The circles show the aftershock epicentres recorded from 25-27 June 1994. Triangles represent portable seismographs; stars show geodetic stations surveyed using GPS in 1992.

2.3 Ground motion recordings

IGNS, a government funded organisation, operates a network of accelerographs throughout the country. Three types of accelerograph are currently in operation: scratch plate, film and digital. During the earthquake the network recorded 16 significant film or digital accelerograms and 17 scratch plate acceleroscope recordings. The Arthur's Pass Police Station instrument recorded a peak ground acceleration of 0.49g at a site 11km from the fault. This is the largest time history acceleration recorded on an accelerograph in New Zealand[1] at the time of writing.

[1] An acceleroscope recording of 0.61g was recorded at Reefton during the 1968 Inangahua earthquake (Magnitude 7.8). The Police Station recording is the largest magnitude acceleration associated with a time history.

2.4 Fault plane

Fixing a fault plane for this particular rupture was not a straightforward process. No surface faulting was observed, despite investigation in the region after the event. The rupture surface of an earthquake is normally defined by aftershocks immediately after the event (Robinson and McGinty, 1998). The shape of the aftershock pattern initially suggested a fault plane striking NNW/SSE and dipping to the SW with equal parts of thrust and strike-slip (Robinson et al. 1995). This assumed fault plane is shown in Figure 2-4, along with instrument locations and orientations close to the fault. Four primary recordings were made, comprising one acceleroscope and three accelerograph recordings. Details of the acceleroscope record and site are presented in Chapter 3; the accelerograph sites and record information is presented in Chapter 4.

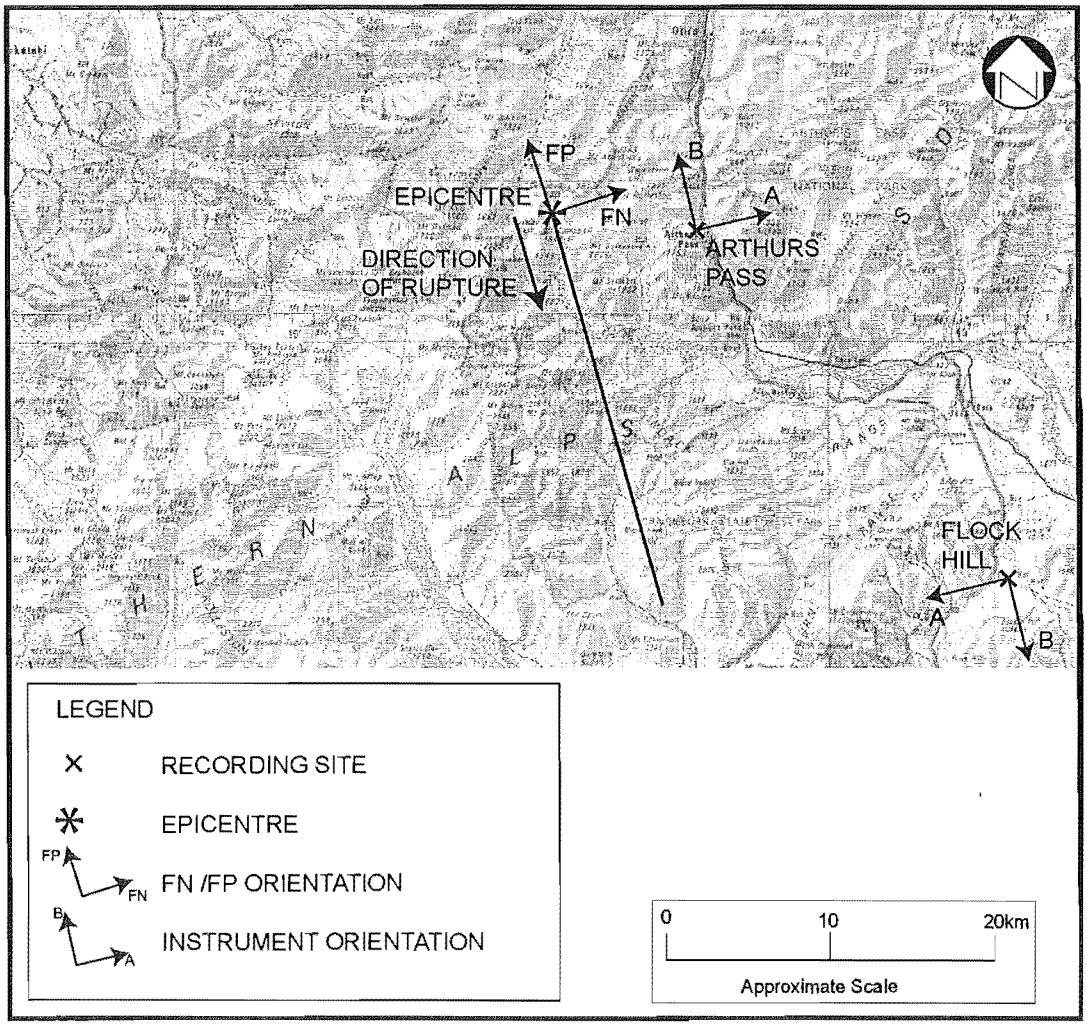

Figure 2-4 Plan view of assumed strike of fault plane with recording sites and orientation of strong ground motion recorders

This type of rupture was initially supported by a stress field analysis carried out by Arnadottir (1998). The stress field analysis carried out suggested that a single slip event did not fit well with observed displacements. The simplest and best fitting dislocation model calculated during her analysis had two different slip patches on a rupture surface striking NNW with a dip of 50° (Arnadottir, 1998). Two separate fault surfaces, modelled as striking NNW and NNE, also agreed with the geodetic measurements. The fault plane shown in Figure 2-4 above has a single slip surface striking NNW, consistent with the initial assessment made by Robinson et al. (1995).

2.4.1 Body wave inversions

Initial far field inversions of body waves using Centroid Moment-Tensor (CMT) and Harvard Moment-Tensor (HMT) solutions generated a number of different solutions. Abercrombie et al. (1998) presented a variety of these solutions to show the significant variations in the results of far field modelling. The rupture mechanisms calculated by the far field inversions varied from strike-slip to pure reverse faulting. A selection of far field CMT and HMT solutions are presented in Appendix 1.

Figure 2-5 shows the varying rupture planes for the earthquake. Robinson et al.'s (1995) rupture plane is shown as a dashed line. The solid line shows the fault plane Abercrombie et al. (1998) concluded was the earthquake rupture. They calculated a predominantly thrust event on a plane oriented NE/SW, striking at 221°, dipping to the NW. The plane is fixed by the aftershock structure extending NE and SW of the epicentre with a centroid depth of 5km. The source rise time was calculated by Abercrombie et al. (1998) to be 5-6 seconds with a rupture propagation velocity that was around 80% of the shear wave velocity. Abercrombie et al. (1998) considered a strike-slip rupture sited along the aftershock backbone to be inconsistent both with body wave modelling and a closer inspection of aftershock patterns. They suggest that the far field analyses initially carried out were flawed, as a fixed depth was assumed during calculation that was deeper than the actual 1-10km aftershock depth.

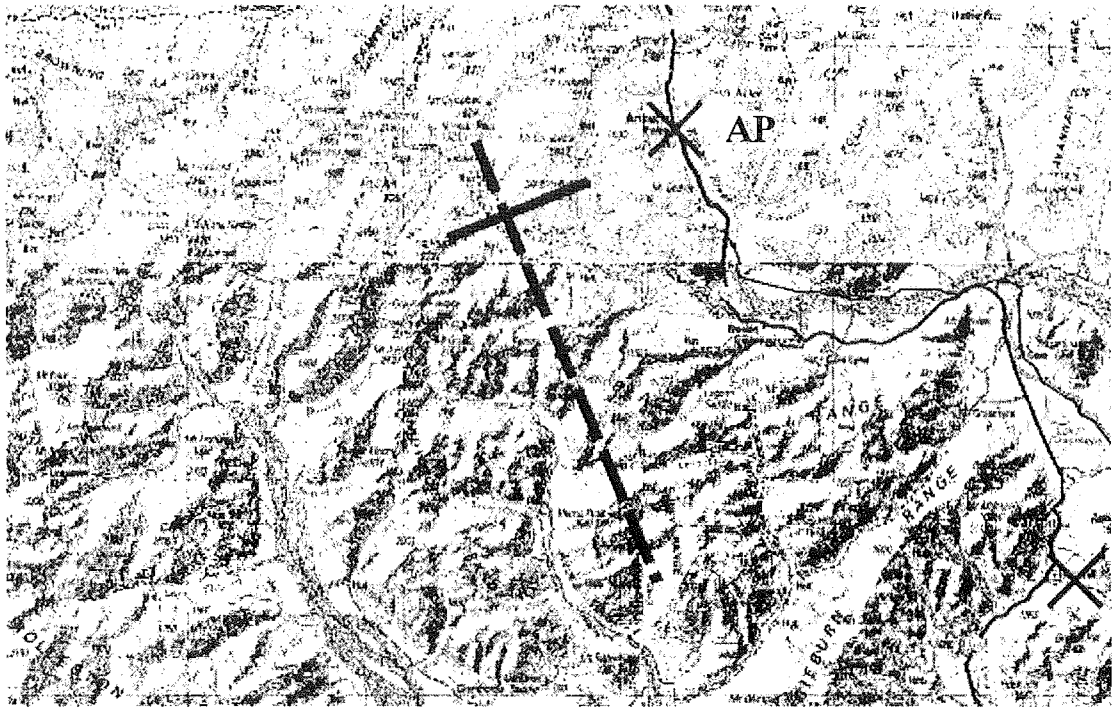

Figure 2-5 Assumed fault plane (dashed line), Abercrombie's (1998) thrust fault plane (solid line).

Robinson and McGinty (1998) postulate that the unusual aftershock locations can be explained by the change in the stress field caused by the earthquake. An investigation they carried out on the Coulomb failure stresses in the region shows that the change in stress could induce aftershocks aligned at right angles to the fault plane. Robinson et al. (1998) conclude that the reason the fault plane is not well defined by the aftershock pattern is a combination of both a high stress drop and a smooth rupture surface. The regional stress field, however, was expected to favour strike-slip faulting with nearly vertical principal axes. This expected type of rupture is very similar to the assumed fault plane. They concluded that the actual event was primarily thrusting. This made the Arthur's Pass earthquake an unusual event in the context of the stress field surrounding the earthquake. They also suggest that the 24 November 1995 Cass earthquake (Magnitude 6.2) may have been induced by the Arthur's Pass event altering the regional stress field.

2.4.2 Fault plane selection

The selection of a fault plane is normally straightforward, with consistent body wave inversions yielding a fault plane that is defined by an aftershock pattern. This rupture sequence was unusual, as different body wave inversions used to orient the rupture plane generated conflicting results. At the time of initial fault plane selection for use in the isolation of directivity effects, the author was not aware of Abercrombie et al.'s (1998) conclusions. The fault plane assumed for rupture analysis is therefore the nearly vertical fault plane initially predicted by Robinson et al. (1995). The idealised, assumed fault plane is shown in Figure 2-4. The fault plane that is assumed, located along the backbone of the aftershock sequence, is consistent both with the earthquakes the regional stress field is thought to induce (Robinson and McGinty, 1998), as well as the initial assessment of the rupture (Robinson et al., 1995).

3 Peak ground acceleration records

Thirty three strong ground motion recordings at ground level were obtained from the 1994 Arthur's Pass earthquake. A selection of these peak ground acceleration (PGA) recordings are analysed for the presence of directivity effects. The peak ground accelerations are sourced from two main classes of recorder; scratch plate acceleroscopes and time history recorders (film or digital instruments). The PGA value used in the analysis is always the largest recorded amplitude, and is independent of direction. Four principal sites , which form part of the PGA dataset, are examined in more detail. The sites, Arthur's Pass, Flock Hill, Greymouth and Lake Coleridge are either situated in a forward rupture directivity zone (Lake Coleridge scratch plate), or are the closest time history recorders with records available for analysis (the other sites). The Lake Coleridge site is addressed in section 3.6, while details of the time history recordings are presented in Chapter 4.

Scratch plate acceleroscopes record horizontal ground accelerations, while film or digital record in three dimensions. For consistency in the data set, this analysis of peak ground acceleration is confined to horizontal acceleration recordings, with a single peak horizontal acceleration value considered from each site. All recordings used in this analysis are sourced from the IGNS network. The University of Canterbury has a film accelerograph sited at the Arthur's Pass DOC headquarters, but this record was not used in the analysis as there was some difficulty in obtaining the record.

3.1 Multiple recordings at sites

At some sites multiple PGA recordings were made. This was either due to the presence of multiple instruments of different types at ground level, or to multiple accelerographs located on different levels of a multi-storey building (the Christchurch Police Station).

3.1.1 Christchurch Police Station

Accelerographs recorded ground motion on multiple levels of this building. Only the ground level recording was included in the data set. Ground level recordings may be influenced by the response of the structure above, but no allowance for these effects are made. Recordings not made at ground level are not been considered in this analysis, and therefore do not appear.

3.1.2 Acceleroscope/accelerograph pairs

Pairs of acceleroscopes (scratch plates) and accelerographs (film or digital) are present at five sites. The sites containing pairs, and peak accelerations recorded by the instruments are tabulated, and presented below, in Table 3-1. It is important to note that a significant disparity between recordings made by different recording devices exists at four of the five sites presented below. This disparity is shown in the third column, 'Ratio', which presents the ratio of the acceleroscope and accelerograph PGA recordings. The ratio of PGA recorded by the two instruments varies significantly both above and below unity. Initial inspection of the data shows that there is no apparent correlation between any of the following factors:

- Instrument type (and hence natural frequency of recording device);
- Site Class
- Epicentral Distance
- PGA amplitude

A more detailed analysis of accelerograph and acceleroscope pairs, specific analysis of instrument properties, the relative location of sites to the earthquake and the nature of the sites on which they are located may allow some conclusions to be drawn regarding the reason why different PGA values were recorded. This analysis falls beyond the scope of this thesis.

Epicentral Distance (km)	Horizontal PGA (g)	Ratio[1]	IGNS Record ID[2]	Instrument Type	Site Class[3]	Site Name
65	0.0476	1.09	K94055A1	Film	B	Greymouth
65	0.052		P94268A1	Scratch Plate	B	Greymouth
111	0.0286	0.66	K94501A1	Film	C	Christchurch Police Station
111	0.019		P94273A1	Scratch Plate	C	Christchurch Arts Centre
124	0.017	1	D94042A1	Digital	C	Hanmer
124	0.017		P94271A1	Scratch Plate	C	Hanmer
140	0.0585	0.94	D94051D1	Digital	C	Westport
140	0.055		P94266B1	Scratch Plate	C	Westport
330	0.0157	1.27	D94044A1	Digital	C	Dunedin
330	0.02		P94292A1	Scratch Plate	C	Dunedin

Table 3-1 Multiple PGA recordings at a site

Notes on Table 3-1:

[1] Ratio $= \dfrac{PGA(ScratchPlate)}{PGA(Accelerograph)}$;

[2] The initial letter of the IGNS record identification also denotes the type of instrument. Thus, D = Digital Accelerograph; K = Film Accelerograph; P = Acceleroscope (Scratch Plate recorder).

[3] Site Class refers to the type of material present at the site. Refer NZS:4203 for more information on these classifications.

3.2 Peak ground acceleration (PGA)

The horizontal peak acceleration data set is shown in Figure 3-1 with corresponding epicentral distances. There is a clear trend of decreasing peak acceleration with increasing distance. This amplitude decrease is clearly shown in Figure 3-2 where the decrease generally follows a linear decrease on a log PGA-epicentral distance chart.

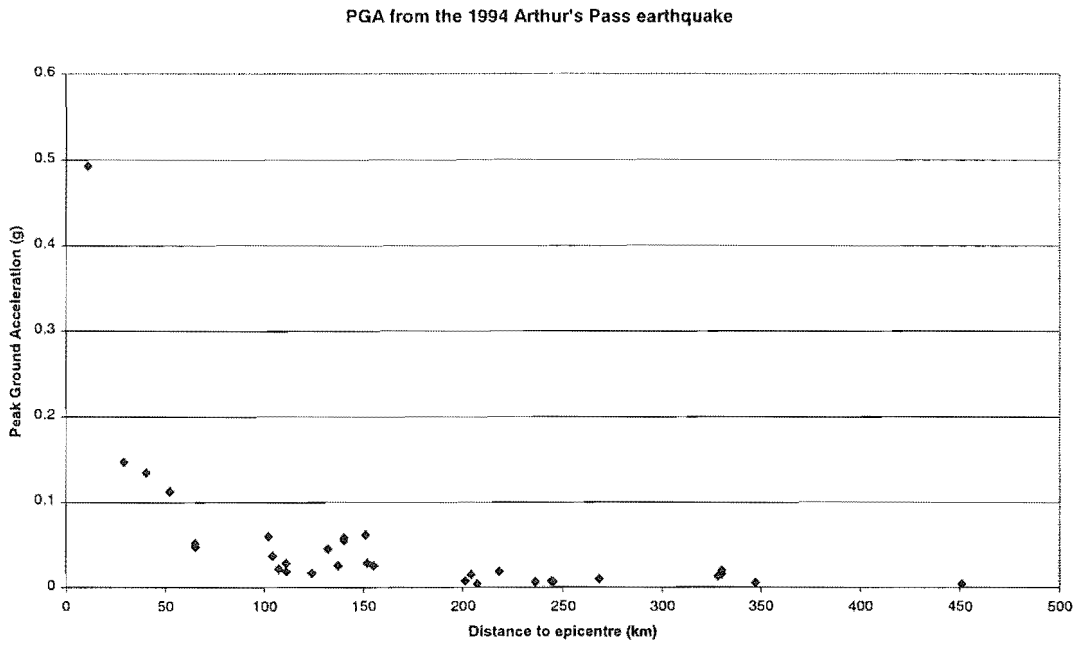

Figure 3-1 PGA from the 1994 Arthur's Pass earthquake

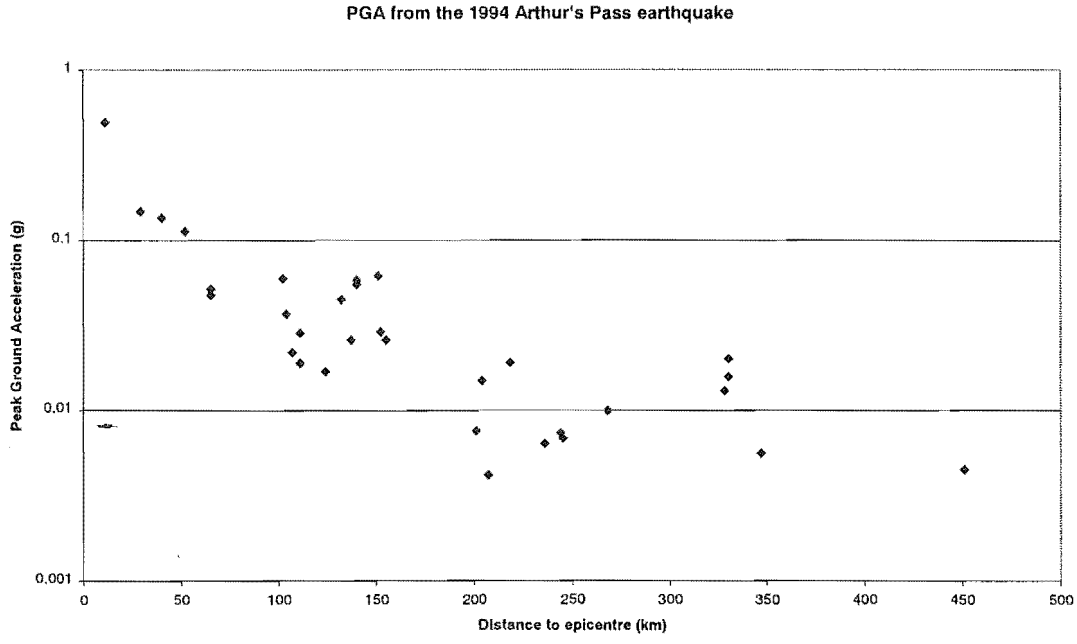

Figure 3-2 log(PGA) showing amplitude decay with distance

An attenuation model is selected to normalise the data set. This allows direct assessment of sites in terms of their amplification of peak accelerations, if applicable. In order to normalise the peak accelerations an attenuation model must be selected. A

number of peak ground acceleration attenuation models are currently available. Three generic international models are considered, along with New Zealand and earthquake specific models. The models considered are:

- Joyner and Boore (1981)
- Sabetta and Pugliese (1987)
- Fukushima and Tanaka (1990)
- McVerry et al. (1993) (NZ generated model)
- Earthquake specific model (Fitted to the PGA dataset from the earthquake)

Equation 3-1 shows the form of the earthquake specific model, which was fitted to the dataset generated by the earthquake. The initial C_1 and C_2 values are 5.48 and 0.0023 respectively. The values of the constants are found by fitting a curve in the form of Equation 3-1 to the 28 data points in PGA-Epicentral distance form. The origin of the constants are explained further in Section 3.4

$$PGA = \frac{C_1}{r} \times e^{(-C_2 * r)} \qquad \text{Equation 3-1}$$

Where:

PGA = peak ground acceleration (g)

C_1 = Constant = 5.48 [g*km]

C_2 = Constant = 0.0023 [1/km]

r = epicentral distance [km]

3.3 Measure of spread

To objectively assess the quality of each attenuation model, a statistical measure of the spread of the PGA dataset is presented. Note that this measure of spread differs from the spreading term used to refer to energy transmission through soils. The numerical difference between the selected attenuation model and the recorded PGA is squared. The sum of the squares represents the spread of the data for the attenuation model. As the quality of fit increases, the measure of spread decreases. In addition to this, the significance of the Arthur's Pass acceleration recording is presented. It is the proportion of the sum of squares due to the acceleration recording. This result, as well as the measure of spread for each attenuation model, is presented in Table 3-2.

Table 3-2 shows, not surprisingly, that the earthquake specific attenuation model has a measure of spread that is four times lower than any other model investigated. There is also a relationship between the contribution of the initial (Arthur's Pass) point, and the measure of spread. Generally, the more accurate the prediction of the Arthur's Pass PGA, the lower the calculated measure of spread. The contribution of the Arthur's Pass PGA to the quality of fit is again shown by the sensitivity study carried out on the earthquake specific attenuation model.

Model	*Measure of spread*	*Proportion**
Joyner and Boore	*0.0465*	*0.71*
Sabetta and Pugliese	*0.0335*	*0.80*
Fukushima and Tanaka	*0.0274*	*0.24*
McVerry et al.	*0.022*	*0.56*
Earthquake specific model	*0.0060*	*0.01*

Table 3-2 Accuracy of attenuation models

* *The proportion measurement is the ratio of the contribution of the initial point to the total sum of squares.*

3.4 Earthquake specific attenuation model

The earthquake specific attenuation model, presented in Equation 3-1, is expanded on and a sensitivity study to the significance of distance is carried out. Various distances are weighted differently in the sum of squares assessment, which shows that the coefficients used are the best fitting.

3.4.1 Geometric spreading

The first part of equation 3-2, C_1/r, corresponds to the geometric spreading of energy around the earthquake source. Two types of spreading are possible, 2 and 3 dimensional. The rate of geometric energy spreading for the terms is $1/\sqrt{r}$ and $1/r$ for 2-dimensional and 3-dimensional respectively. In order to analyse the nature of spreading occurring, the PGA data set was regressed with the values of c and α in the term c/r^{α}. A value of α close to 1.0 was calculated for the best fit, corresponding to 3-dimensional spreading. The first term is therefore selected as C_1/r.

3.4.2 Material losses

The second term in the model, $e^{-C_2 r}$, corresponds to natural or frictional losses. It is analogous to the inverse of the specific attenuation constant of the material, 'Q'. Brune (1970) used the 'Q' value to represent material damping. The C_2 value in the equation therefore represents material losses due to damping in the material. While Brune dealt with the prediction of far field Fourier Spectra rather than peak acceleration, this representation enhances the accuracy of the model.

3.4.3 Fitting attenuation model to data

The quality of fit of any particular model is assessed using the measure of spread stated in section 3.3. The sensitivity of the model to variation in the data set becomes clear in section 3.5.

3.5 Distance classes

Figure 3-3 shows the data divided into 4 distance classes: Close, Medium-Close, Medium and Far field data. The sum of squares from each class is weighted to reflect its relative importance in the fitting of the best-fit model. This will allow the significance of each class in the fitting of the model to be analysed.

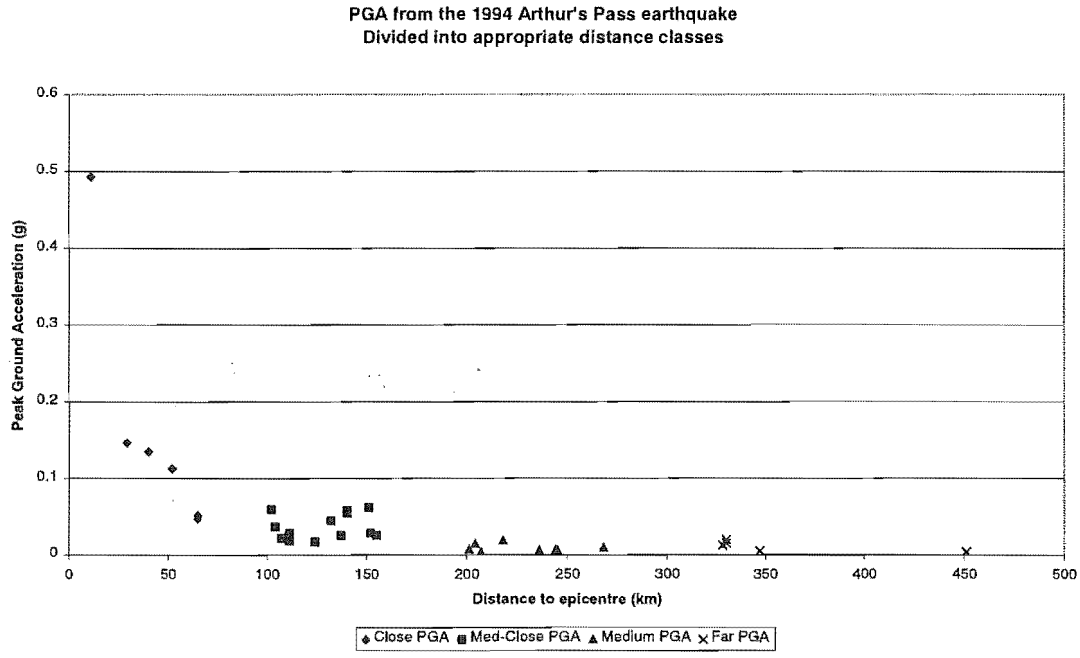

Figure 3-3 Division of PGA into distance classes

3.5.1 Unweighted data set

This standard weighting, shown in Table 3-3, is used as the benchmark for data evaluation. All variations are compared with these results. This benchmark analysis does not consider variations between distance classes. The significance of different distance classes is considered throughout this section.

Field	*Weighting*
Close	*1*
Med-Close	*1*
Medium	*1*
Far	*1*

Table 3-3 Weightings used for unweighted data set

$C_1 = 5.48$ $C_2 = 0.0023$ *Sum of squares,* $\Sigma(x_i - \overline{x_i})^2 = 0.005971$

Equation is $PGA = \frac{5.48}{r} \times e^{(-0.0023*r)}$ Equation 3-2

3.5.2 Weighting emphasising near field data

An accurate fit in the near field is important as this is the critical area of interest, where directivity effects are most significant. Near field peak accelerations have been the controlling influence on structural design in the past. Weighting the far field data, shown in Table 3-4, results in no significant difference to the benchmark assessment, implying that near field data controls the shape and position of the best fit line.

Field	*Weighting*
Close	*1*
Med-Close	*0.75*
Medium	*0.25*
Far	*0.10*

Table 3-4 Weightings used to emphasise near field importance

$C_1 = 5.47$ $C_2 = 0.0021$ *Sum of squares,* $\Sigma(x_i - \overline{x_i})^2 = 0.005976$

Equation is $PGA = \frac{5.47}{r} \times e^{(-0.0021*r)}$ Equation 3-3

3.5.3 Removal of medium and far field data

Table 3-5 shows the significance of the medium and far field data. Removing the far and medium data results in a significant change in C_2 (0.0035 vs 0.0023), but little change in the sum of the squares or in C_1 (5.58 vs 5.48). C_1 is the more critical constant in this model as it controls the near field predictions.

Field	*Weighting*
Close	*1*
Med-Close	*0.1*
Medium	*0*
Far	*0*

Table 3-5 Removal of medium and far field data

$C_1 = 5.58$ $C_2 = 0.0035$ *Sum of squares,* $\Sigma(x_i - \overline{x_i})^2 = 0.006296$

Equation is $PGA = \frac{5.58}{r} \times e^{(-0.0035*r)}$ Equation 3-4

3.5.4 Removal of initial point from data set

The significance of the initial point in terms of model fit has been demonstrated in section 3.3. If the initial point has been altered by directivity effects then this will have a significant impact on the calibration of the best fit line. Since the best fit line is used for data normalisation it would be inappropriate to use a line that does not represent the actual data recorded. The sum of squares, without the initial point, for both best fit lines, are compared to assess the impact of the initial point, and the weightings used for this analysis are presented in Table 3-6.

Field	*Weighting*
Close	*1.00*
Med-Close	*0.75*
Medium	*0.25*
Far	*0.10*

Table 3-6 Removal of initial point from data set

$C_1 = 4.77$ $C_2 = 0.00053$ *Sum of squares,* $\Sigma(x_i - \overline{x_i})^2 = 0.009532$

Equation is $PGA = \frac{4.77}{r} \times e^{(-0.00053*r)}$ Equation 3-5

Table 3-7 shows the sum of the squares of the benchmark line, and the truncated line where the initial point is removed from the dataset. The benchmark line sum of squares, in this instance, ignores the contribution from the initial point. There is little

difference between the two values, implying that the benchmark line fits well over the entire data set.

	Sum of Squares
Benchmark line	0.005922
Truncated line	0.005750

Table 3-7 Sum of squares excluding initial point

3.5.5 Summary of variations

Table 3-8 shows the summary of the varying earthquake models assessed. The benchmark line used generated the lowest sum of squares in the analysis. It most accurately represents the attenuation occurring in this earthquake and will be used to normalise the data set for further analysis. The equation selected for the normalisation of peak ground accelerations is shown in Equation 3-6.

$$PGA = \frac{5.48}{r} \times e^{(-0.0023*r)}$$

Equation 3-6

Best Fit Line	*Sum of Squares*	C_1	C_2
Raw data	*0.005971*	*5.48*	*0.0023*
Near field weighting	*0.005976*	*5.47*	*0.0021*
Removal of far field data	*0.006296*	*5.58*	*0.0035*
Removal of initial point	*0.009532*	*4.77*	*0.00053*

Table 3-8 Summary of various earthquake specific models assessed

3.6 Lake Coleridge scratch plate

The Lake Coleridge site is aligned with the assumed fault rupture plane and in the direction of slip. It is therefore located in the forward rupture directivity zone of the assumed fault plane. Records that are strongly affected by forward rupture directivity generally have larger than expected peak accelerations, with amplification in the fault normal direction (Somerville, 1996).

Figure 3-4 shows the acceleroscope record from Lake Coleridge. Figure 3-5 shows the same record, magnified, with a rectangle (Breadth to width ratio of 1.6) overlaid. The rectangle highlights the anisotropic nature of the horizontal ground motion at the site. Leaving aside the single peak excursion, the shape of the record aligns well along fault normal and fault parallel lines, which are also shown on the figure. This anisotropy could be considered indicative of the site being located in a forward rupture directivity zone of the assumed fault rupture surface.

The peak acceleration, 0.13g, was at a bearing of 339°, in the fault parallel direction. This is at right angles to the expected (fault normal) direction of peak acceleration that is expected if forward rupture directivity effects are significant at the site. A peak acceleration of 0.17g is predicted at the site by the earthquake specific attenuation model. This lower than predicted peak ground acceleration, oriented in the fault parallel direction is inconsistent with forward rupture directivity effects.

Chapter 7 of this thesis assesses the effect of the orientation of softer surficial layers on recorded ground motions. While no definite conclusion is drawn on the influence of these layers on ground motion, the orientation of the valley at the site is presented in Figure 3-5. The orientation of sediment is also presented on the site plans for the Arthur's Pass Police Station and Greymouth. The valley does not align with either the fault normal, or the fault parallel direction. It is therefore unlikely that valley orientation had significant effects on recorded ground motion at the site.

A number of conflicting directivity indicators are present in the Lake Coleridge record. While the record shows significant anisotropy in recorded accelerations,

oriented in a fashion consistent with forward rupture directivity effects, the amplitude and direction of the peak acceleration belies the anisotropic nature of the record.

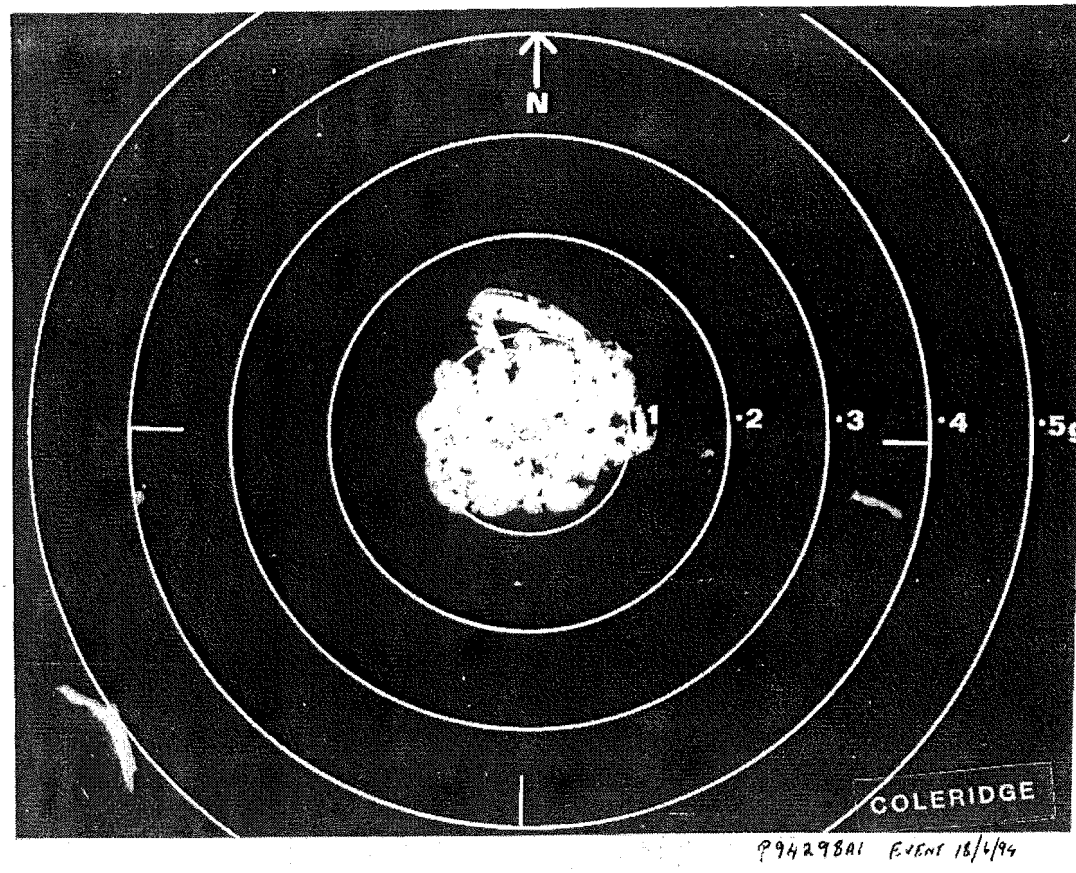

Figure 3-4 Lake Coleridge acceleroscope recording

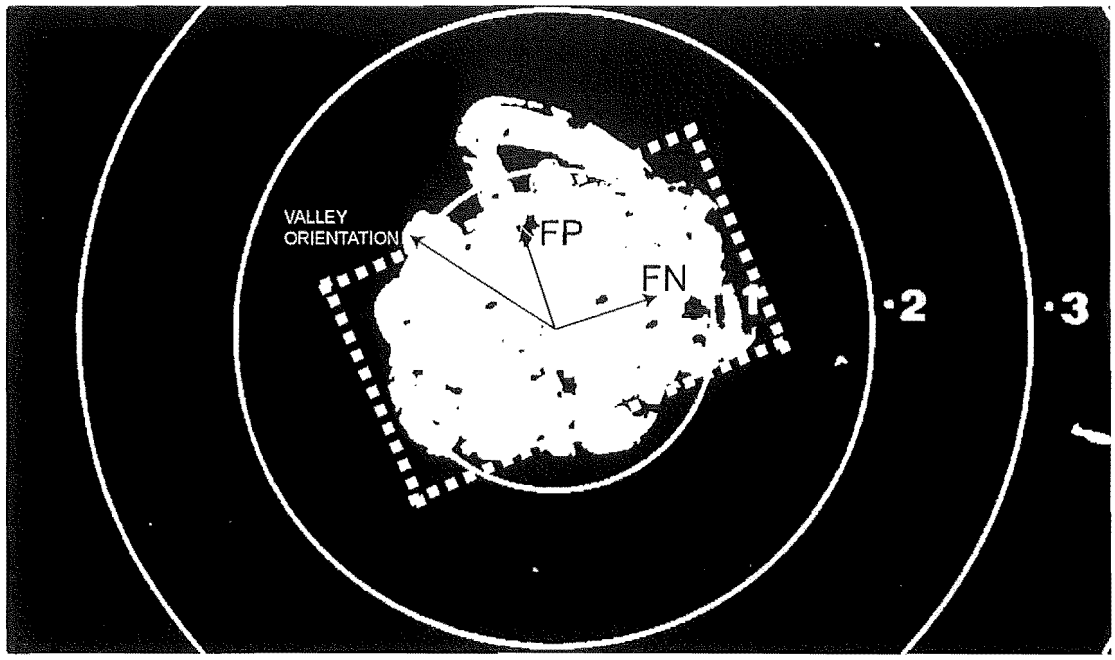

Figure 3-5 Lake Coleridge acceleroscope record

3.7 Hokitika scratch plate

The Hokitika acceleration record, shown in Figure 3-6, has a peak acceleration of 0.11g. No appreciable anisotropy is noted in the Hokitika record. The peak acceleration is marginally smaller than that recorded at Lake Coleridge. Hokitika's epicentral distance (53km) is similar to Lake Coleridge's (40km). The similarity in recorded peak ground acceleration between the Lake Coleridge and Hokitika acceleroscopes is inconsistent with the Lake Coleridge acceleroscope being situated in a forward rupture zone.

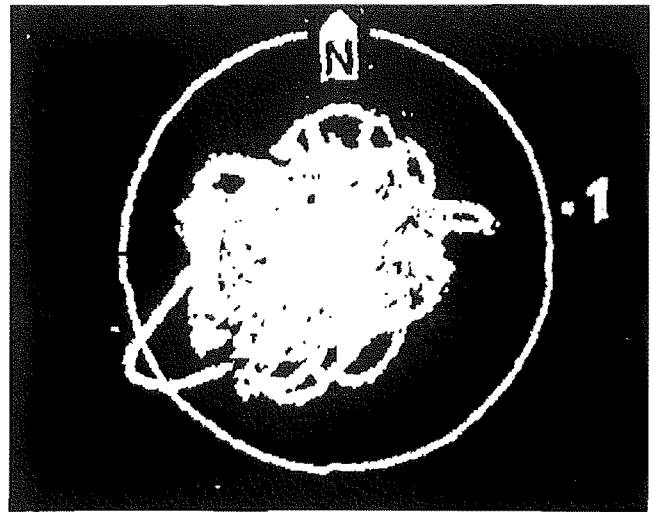

Figure 3-6 Hokitika acceleroscope record

4 Time history recordings

Time history recordings from the Arthur's Pass Police Station, Flock Hill and Greymouth are examined and analysed in this chapter. Figure 4-1 reproduces the aftershock pattern on a topographical map, as well as depicting the location of the Arthur's Pass and Flock Hill recording sites. Figure 4-2 shows the location of sites considered, as well as Lake Coleridge and Hokitika, the location of the two scratch plate acceleroscopes. The time history recordings comprise corrected acceleration, velocity and displacement records, sourced from Volume 2 of IGNS's data disk. These are then transformed to fault normal and fault parallel components using the equations presented in Section 4.1. The transformed records are then analysed for the presence of directivity effects manifesting as anisotropic ground motion. A summary of recording details from the three closest accelerograph instrument locations is presented in Table 4-1. The aftershock pattern from the earthquake is shown in Figure 4-1, along with the Arthur's Pass and Flock Hill stations (denoted by the large X's). The transformation equations used, instrument orientation, and FN/FP orientation are presented in Table 4-2.

Site	Epicentral Distance	IGNS Record Number	Instrument Type
Arthur's Pass Police Station (AP)	11	D94505A1	Digital
Flock Hill (FH)	26	K94112A1	Film
Greymouth (GM)	69	K94055A1	Film

Table 4-1 Details of accelerograph recordings used in analysis

The previous studies described in Chapter 1 (Somerville, 1996; Somerville et al. 1997; Somerville et al., 1997), were confined to forward rupture directivity effects. Based on the conclusions of theses studies, the effect of forward rupture directivity effects on the fault normal and fault parallel components of ground motion are summarised below.

Acceleration Time History Recordings:

- Peak FN greater than Peak FP
- Peak acceleration located at the initial arrival of seismic shear waves
- Shorter FN duration than FP

Velocity Time History Recordings:

- Peak FN greater than Peak FP
- Peak velocity located at the initial arrival of seismic shear waves

Displacement Time History Recordings:

- Peak FN greater than Peak FP
- Peak displacement located at the initial arrival of seismic shear waves

4.1 Time History Records

Figure 4-2 shows the relative location of the three accelerograph sites with time history recorders. The orientations of each accelerograph's two principal recording directions is shown, along with FN and FP directions. The transformation process comprised vector addition of recorded components using the equations presented in Table 4-2. It is apparent from Table 4-2 and Figure 4-2 that both the Arthur's Pass and Flock Hill sites are closely aligned to the fault normal and fault parallel directions. The Greymouth site does not align with either the fault normal or fault parallel directions.

Site	Bearing Site to Epicentre	Principal Direction		Transformation Equations	
		A	B	FN (=N72E)	FP (=N18W)
AP	232	N77E	N13W	ACos5 + BSin5	ASin5 – Bcos5
FH	290	S76W	S14E	-ASin4 + BCos4	-ACos4 – Bsin4
GM	160	N00E	N90E	ASin18 – Bcos18	-ACos18 – Bsin18

Table 4-2 Accelerograph sites and equations used in transformation

From the three time history recording sites closest to the fault, the Arthur's Pass Police Station, Flock Hill and Greymouth, accelerations, velocities and displacements are compared in the fault normal and fault parallel directions. The three sites used in this analysis were selected based on record availability. While they are not in ideal locations, they are the only sites available that contained accelerographs. Figure 4-2 presents a plan view of the locations of two recording sites, as well as the assumed rupture plane.

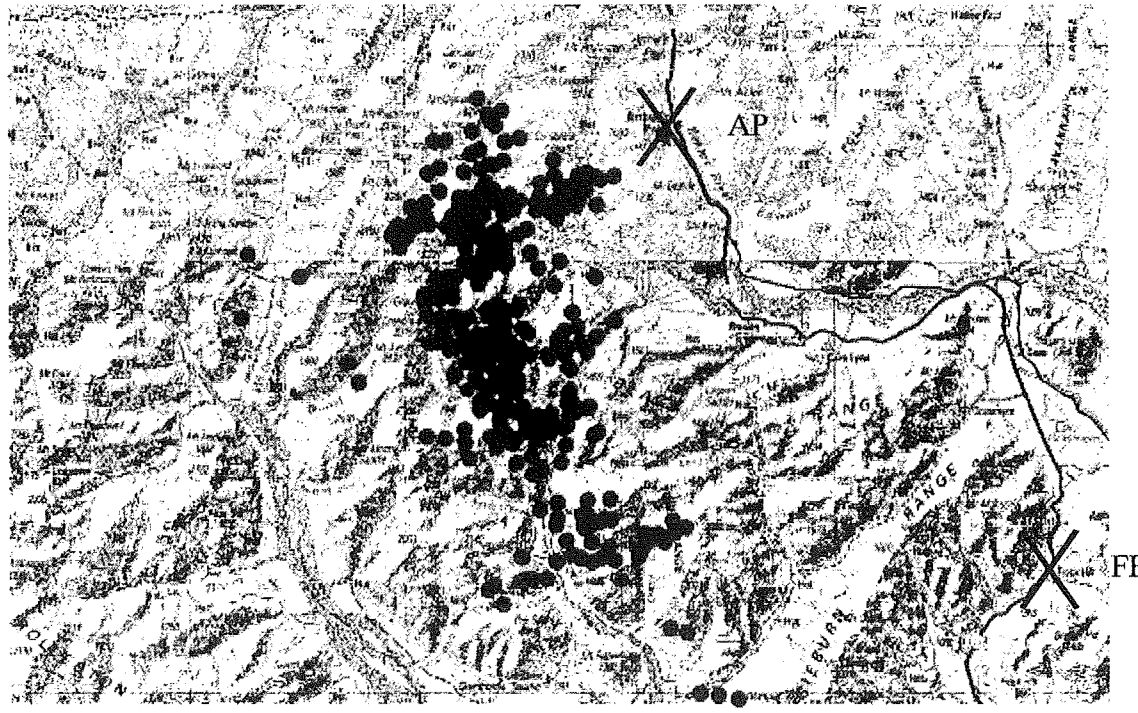

Figure 4-1 Localised aftershocks and the location of Arthur's Pass and Flock Hill

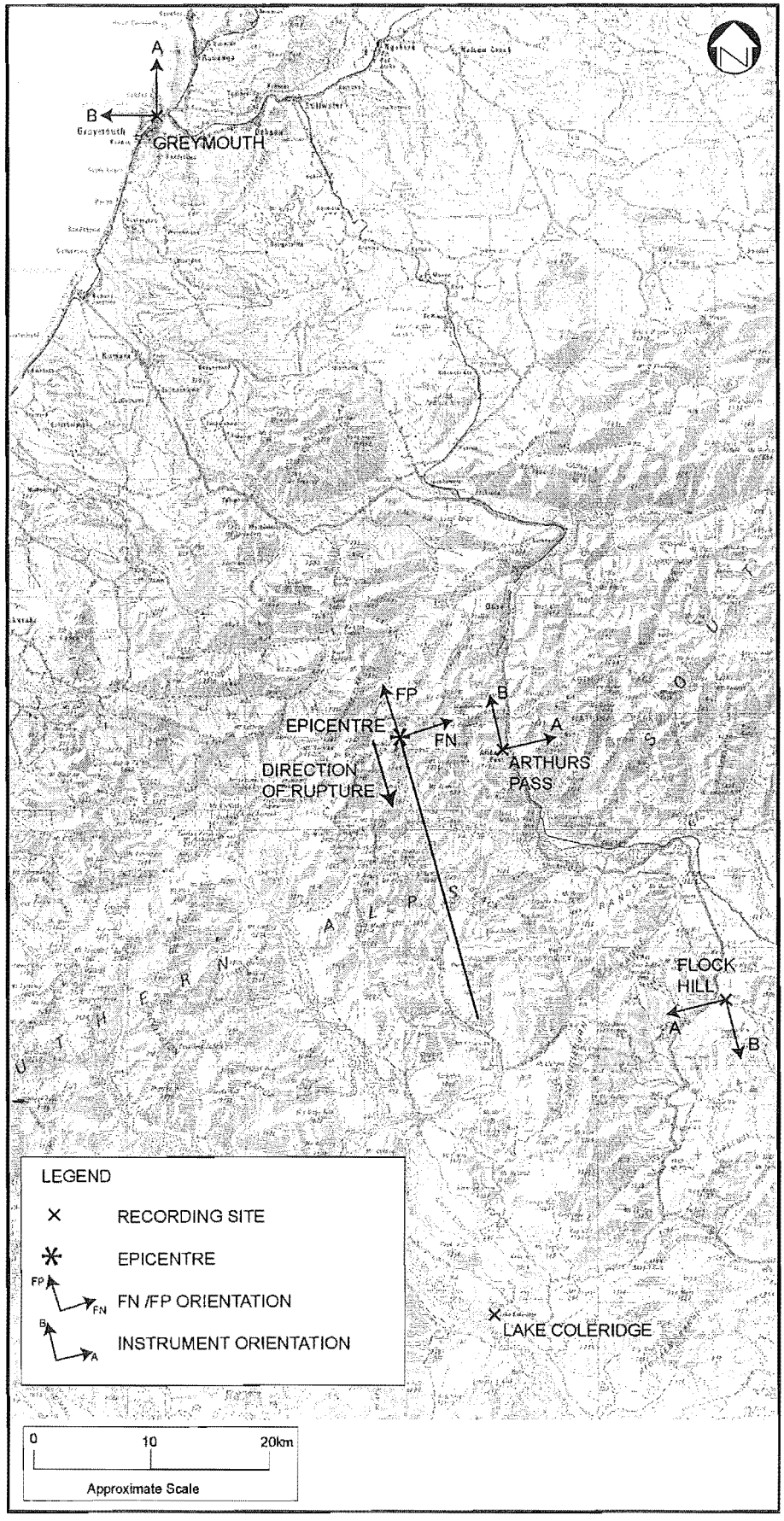

Figure 4-2 Plan view of assumed rupture and site locations

4.2 Local topography of sites used in analysis

In Figures 4-3 to 4-5, X marks the location of the recording instrument, and the arrow shows the orientation of any overlying soft layers in the local region. The orientation of the overlying soft layers has the potential to affect ground motion at sites (Kramer, 1996). For this reason the orientation of soft layers is shown in the figures, and discussed in the analysis of the region.

4.2.1 Arthur's Pass Police Station

The Arthur's Pass site was located to one side of the assumed rupture, and approximately 11km from the epicentre. Forward rupture directivity effects were not expected at the site as it was not located in the path of the assumed rupture front. High levels of ground motion were recorded at the site, however, a reflection of the proximity of the site to the epicentre. If the NE/SW striking thrust event predicted by Abercrombie et al. (1998) had occurred, then some directivity effects could have been present at the site, but these were not observed.

Figure 4-3 shows the topography around the Arthur's Pass site. The site was situated at the base of a valley that is oriented in the fault parallel direction. Any effect that a two dimensional orientation of soft material may have on the site would therefore be in the fault normal direction.

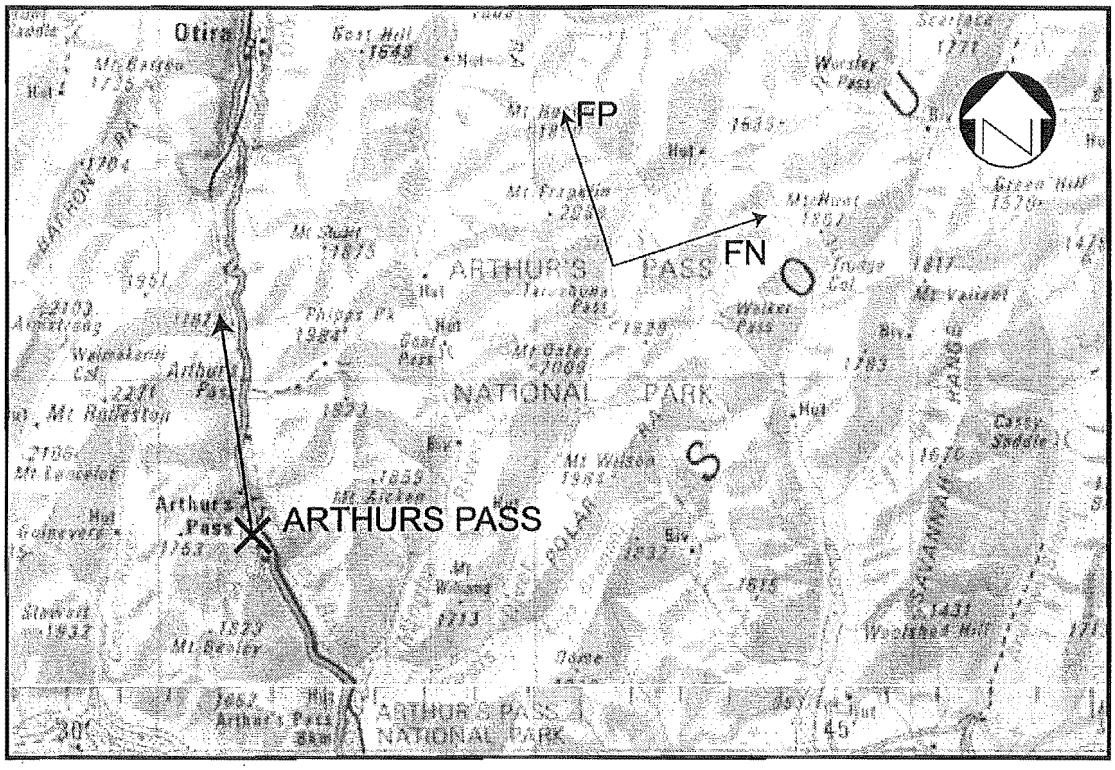

Figure 4-3 Arthur's Pass site location, with valley orientation and FN/FP directions

4.2.2 Flock Hill

The Flock Hill station was 26km from the epicentre. The assumed rupture direction initially made an angle of 30 degrees with the Flock Hill site. The site was located further from the fault than the Arthur's Pass Police Station, and therefore experienced lower intensity shaking. If the source geometry was as assumed, then fault geometry suggests that some directivity effects would be noticed at the Flock Hill station. These effects are expected to be more noticeable at longer periods due to the period dependence of the theoretical mechanics (Kasahara, 1980; Lay and Wallace, 1995), which are discussed more fully in Chapter 8.

Figure 4-4 shows the Flock Hill site is situated at the junction of three valley systems. No clear orientation of surficial material can therefore be presented.

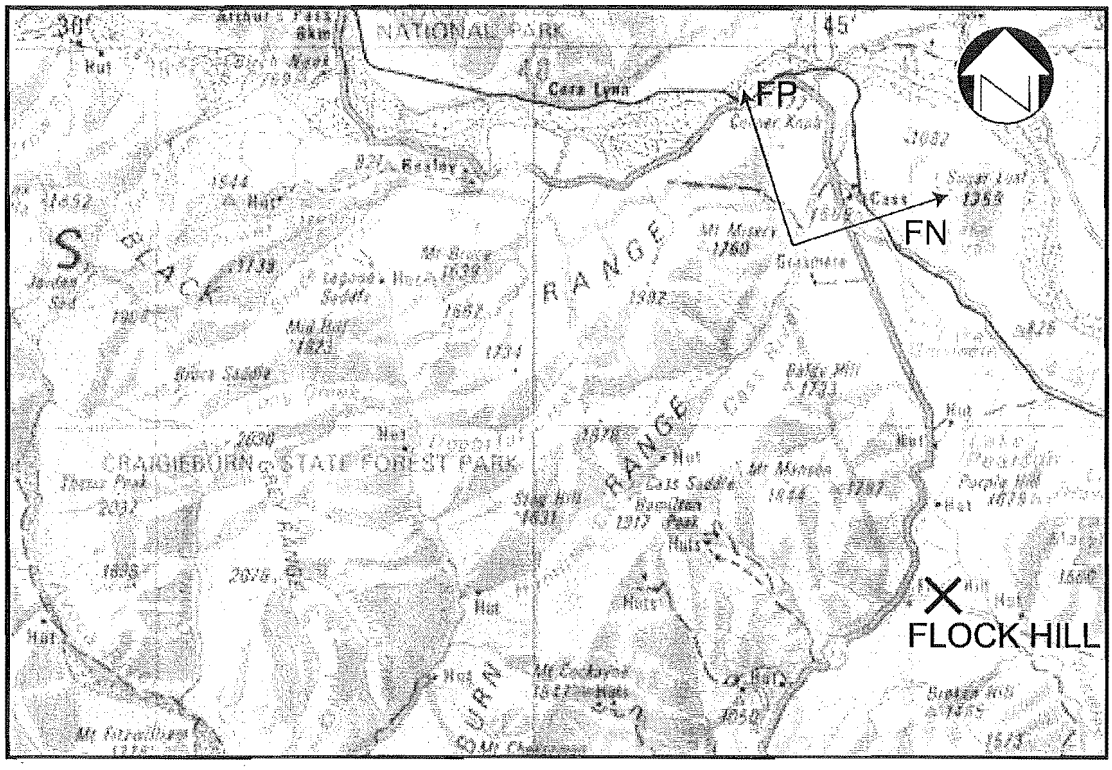

Figure 4-4 Flock Hill site location with FN/FP directions

4.2.3 Greymouth

Greymouth, the third site considered, was located off the back of the assumed fault and is shown in Figure 4-5. The ground motion recorder is located in the Telecom building in the centre of Greymouth. Fault geometry was not expected to be significant as the site was located 69km from the epicentre. The soft layers at the site are oriented parallel to the shoreline. Initially, the surficial soil layers were thought to have some impact on the ground motion recordings made at the site, and this is discussed in Chapter 7. The anisotropy of the ground motion recordings at this site was the basis for examining the orientation of soft layers at the Arthur's Pass and Flock Hill sites.

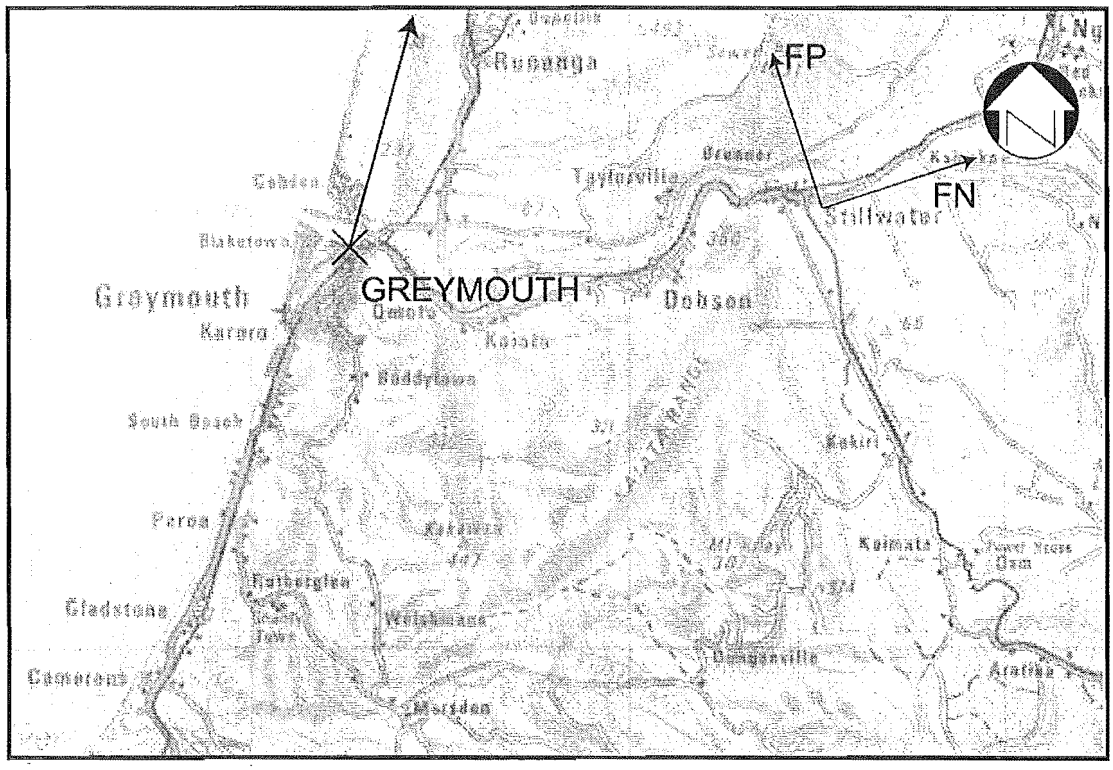

Figure 4-5 Greymouth site location with soft layer orientation and FN/FP directions

4.3 Arthur's Pass Police Station recordings

4.3.1 Acceleration records

Figures 4-6 and 4-7 show peak accelerations of 3180 mm/s/s and 4340 mm/s/s in the fault normal and fault parallel directions respectively. These peaks occur at times of 14.52 and 13.82 seconds from the start of recording, well into the main body of the record. Somerville (1996) notes that forward rupture directivity effects are characterised by large, brief pulses of ground motion. The peaks in these records are located at, or very close to, the beginning of the ground motion time history. A significantly higher peak acceleration in the fault normal direction at the start of the record is therefore indicative of forward rupture directivity effects. The peak acceleration in the Arthur's Pass record is neither at the start of the record, nor in the fault normal direction, leading to the conclusion that the record is not exhibiting evidence of forward rupture directivity effects.

The plan view of the assumed rupture, combined with the assumed rupture and shear wave velocities, shows that the peak acceleration occurs at a time that was inconsistent with arrival of shear waves from the closest approach of the moving rupture front. If the peak recorded acceleration is due to the closest approach of the rupture, then this discrepancy is another indicator that the assumed fault plane may not represent the actual fault plane.

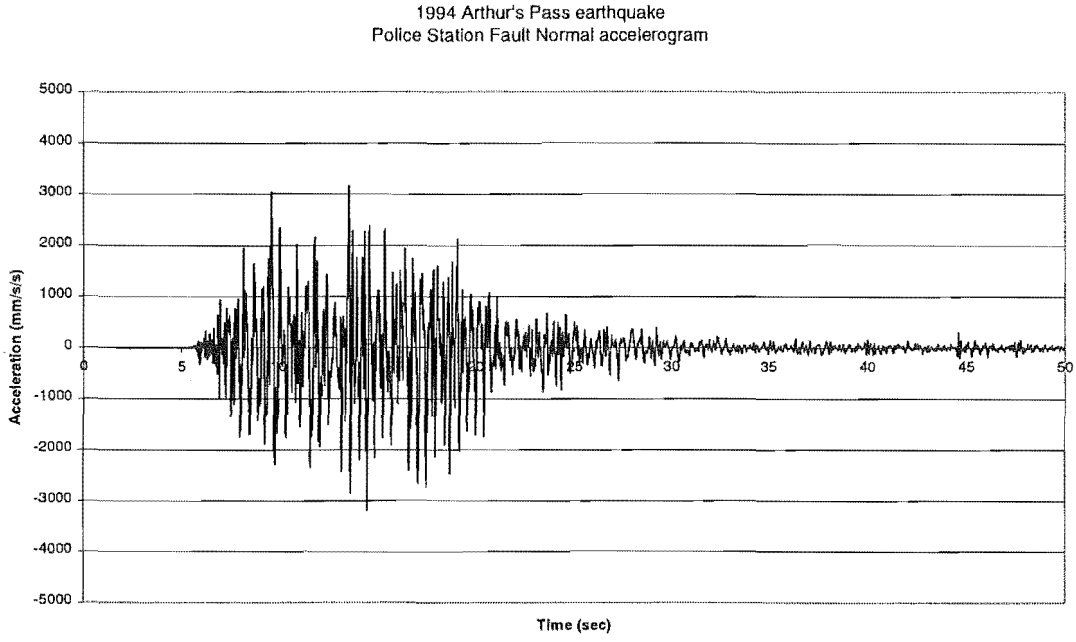

Figure 4-6 Arthur's Pass fault normal acceleration record

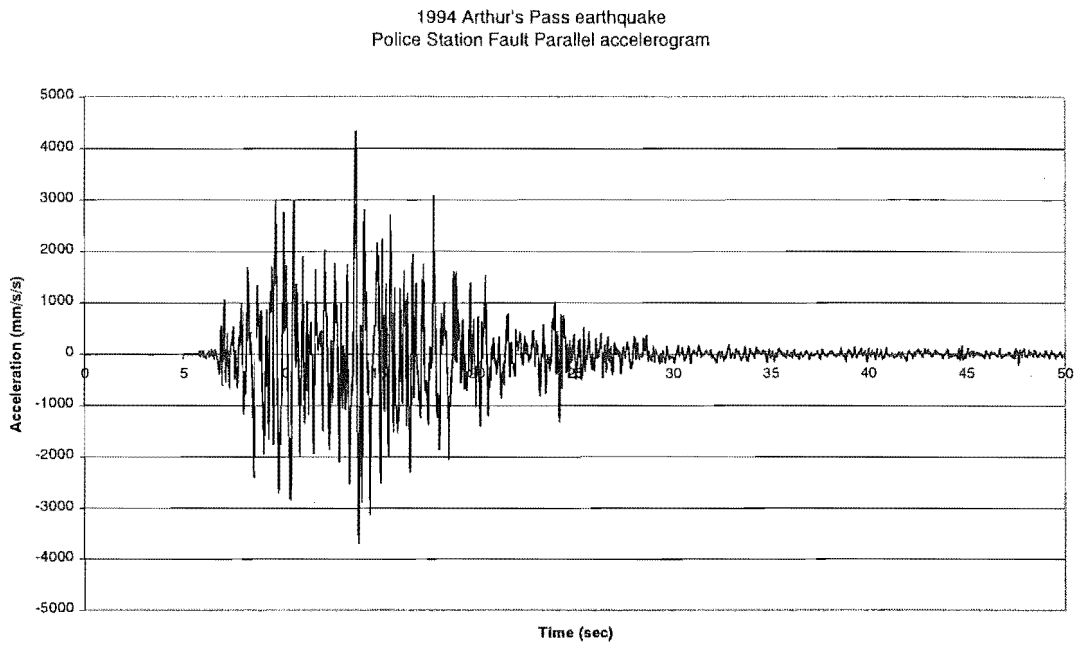

Figure 4-7 Arthur's Pass fault parallel acceleration record

Another method used in the assessment of anisotropy at a site is the comparison of acceleration amplitudes in orthogonal directions. Since the fault normal direction is expected to show larger acceleration amplitudes, this effect should be shown when the data is sorted. The amplitude of each recorded acceleration point is therefore listed, sorted, and the first 1500 values presented.

The sorted fault parallel acceleration amplitudes, shown in Figure 4-8, show that the fault parallel amplitudes are larger than amplitudes in the fault normal. This observation is inconsistent with classical forward rupture directivity effects. Sites further down the assumed fault, such as the Lake Coleridge scratch plate, are expected to exhibit more significant directivity effects, if any are present.

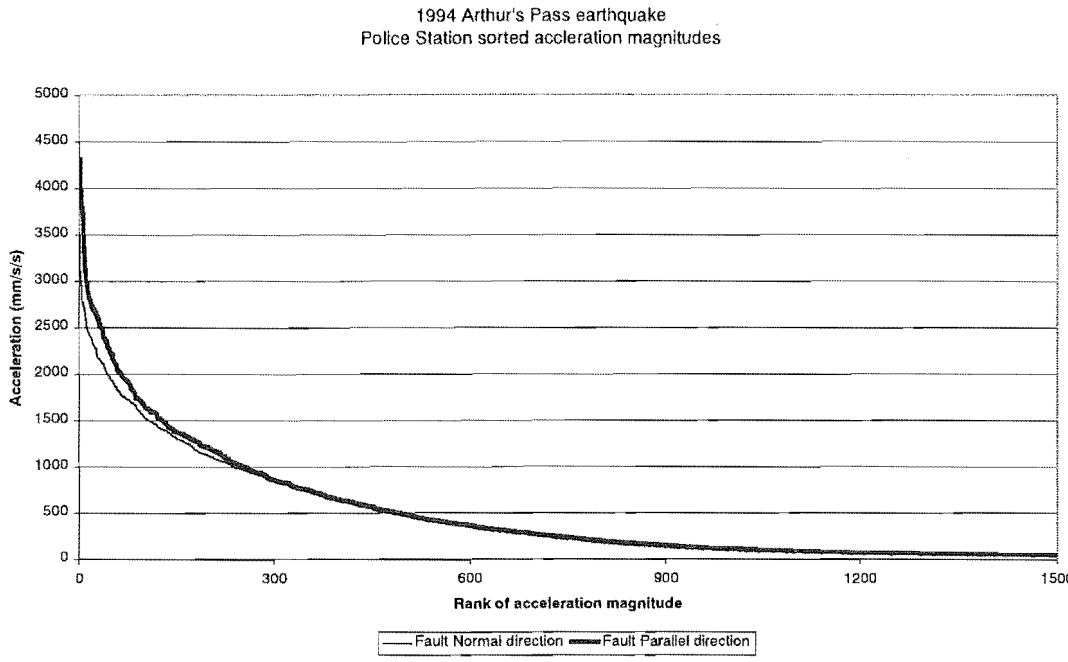

Figure 4-8 Arthur's Pass sorted acceleration amplitudes

4.3.2 Velocity records

Figures 4-9 and 4-10 show that the peak velocity in the fault parallel direction is significantly greater than the peak velocity in the fault normal. Peak velocities in the fault normal and fault parallel directions are 236 mm/s and 314 mm/s respectively, at times of 16.54 and 13.86 seconds.

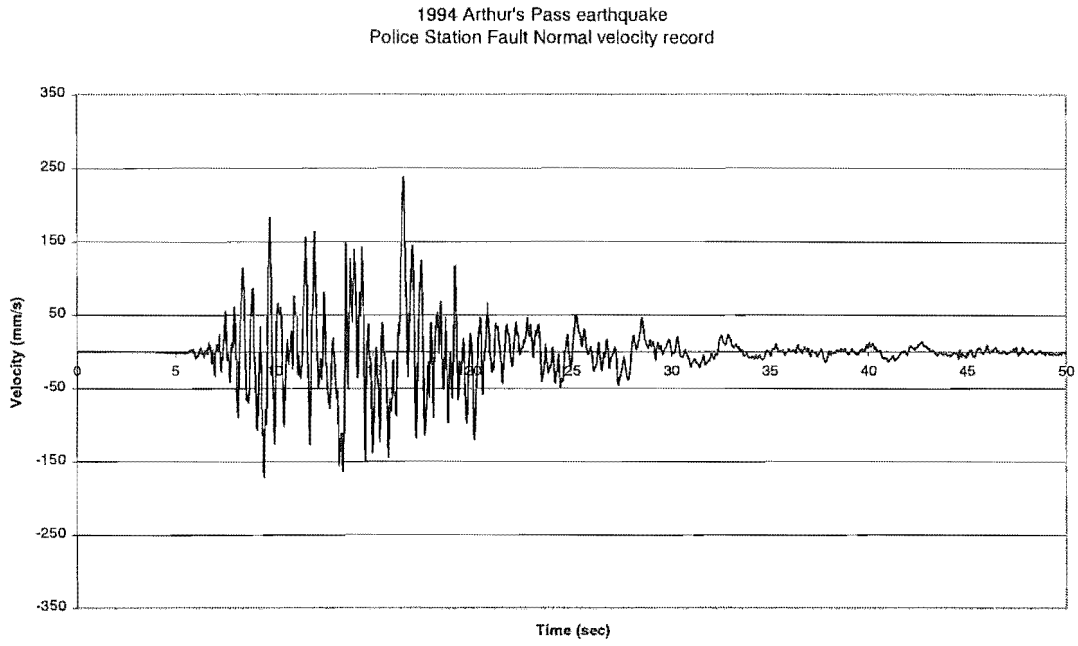

Figure 4-9 Arthur's Pass fault normal velocity record

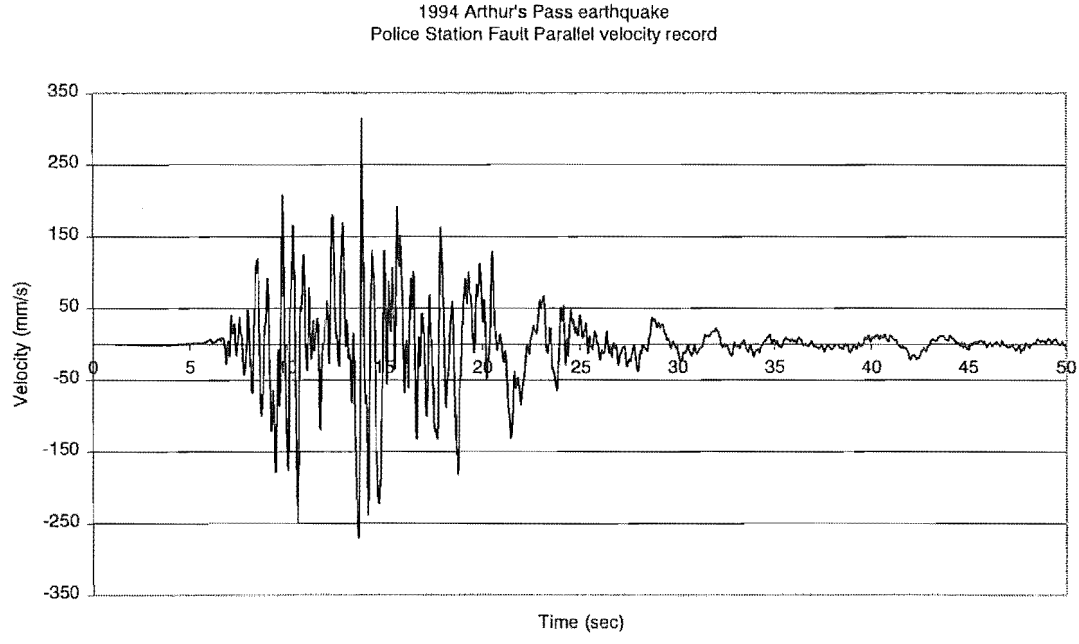

Figure 4-10 Arthur's Pass fault parallel velocity record

Figure 4-11 shows that velocity amplitudes are significantly smaller in the fault normal direction. This is consistent with results from the sorted acceleration

amplitudes. At this site there are significant differences in the amplitudes of recorded velocity in the two directions.

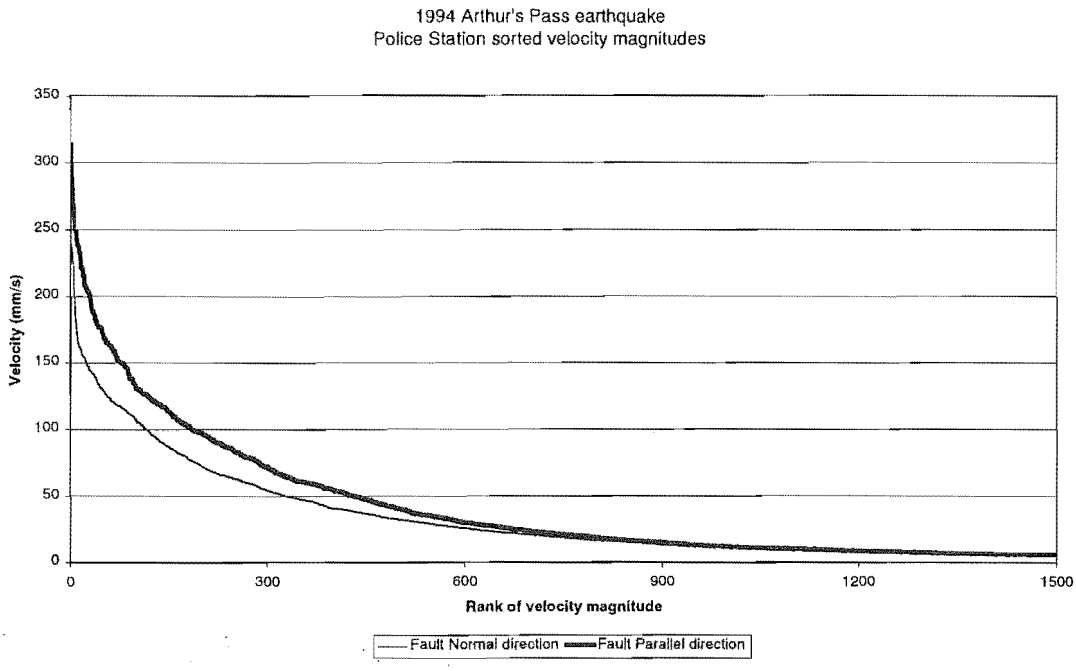

Figure 4-11 Arthur's Pass sorted velocity amplitudes

4.3.3 Displacement records

The two displacement components, presented in Figure 4-12, exhibit significantly different behaviour throughout the main body of the record. Peak displacements in the two directions are very similar; 53.4 mm and 54.4 mm in the fault normal and fault parallel directions. The fault parallel direction has another significant peak of 53.4 mm and exhibits consistently larger amplitudes than the fault normal.

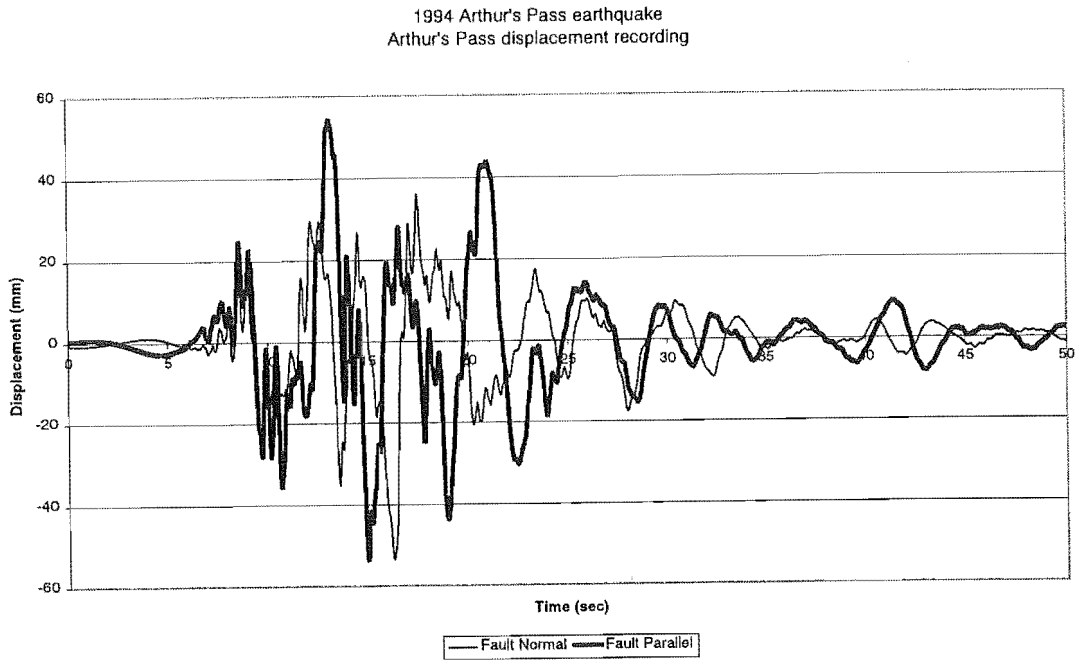

Figure 4-12 Arthur's Pass displacement records

4.3.4 Strong motion duration

Variations in strong motion duration between sites are indicative of directivity effects (Somerville 1996, Somerville et al. 1997). As well as the variation between sites, durations in varying directions at sites were calculated. Duration differences in the fault normal and fault parallel directions at sites exist and are consistent with the variation in intensities predicted by the fault rupture model applied in Chapter 8.

Table 4-3 presents the durations calculated for three components of recorded acceleration: fault normal, fault parallel and the vector sum of fault normal and fault parallel acceleration amplitudes (total). The cumulative energy is represented by the component's acceleration amplitude, squared, with a cumulative sum calculated for each acceleration value. Each cumulative sum is converted to a percentage of the total, and the length of time between 5% and 95% is presented as the strong ground motion duration. Table 4-3 shows that the duration of strong ground motion in the fault normal direction is longer than in the fault parallel. The shorter duration in the fault parallel direction is consistent with the higher intensity records in that direction.

Component	FN	FP	Total
Duration (sec)	12.2	11.5	11.9

Table 4-3 Arthur's Pass strong motion duration

4.3.5 Summary of Arthur's Pass records

The Arthur's Pass Police Station site is located part-way down the assumed fault rupture. It was not in the path of the rupture front. For these two reasons, forward rupture directivity effects were not expected to be significant in the ground motion recordings. The peak acceleration and velocity records were both in the fault parallel direction. The duration was shorter in the fault parallel direction, corresponding to higher intensity motion. Both the fault normal and fault parallel displacement records exhibit similar amplitude peaks. Application of the fault rupture model used in Chapter 8 results in higher predicted Fourier amplitudes in the fault parallel direction, consistent with what is observed at the site.

4.4 Flock Hill

4.4.1 Acceleration records

Figure 4-13 shows a pronounced peak at the beginning of the fault normal acceleration record. This peak, at time of 9.32 seconds, is due to the arrival of the seismic shear waves. Both the large amplitude, and the location of the peak are consistent with forward rupture directivity effects (Somerville, 1996). The peak accelerations, from Figures 4-13 and 4-14 are 1382 mm/s/s at 9.36 seconds and 1201 mm/s/s at 9.32 seconds in the fault normal and fault parallel directions respectively, located at the beginning of the strong motion recordings. The sorted acceleration amplitudes, shown in Figure 4-15, show that the largest peak accelerations are in the fault normal direction, but that, aside from the largest 150 amplitudes, the fault parallel amplitudes are slightly larger through the rest of the record.

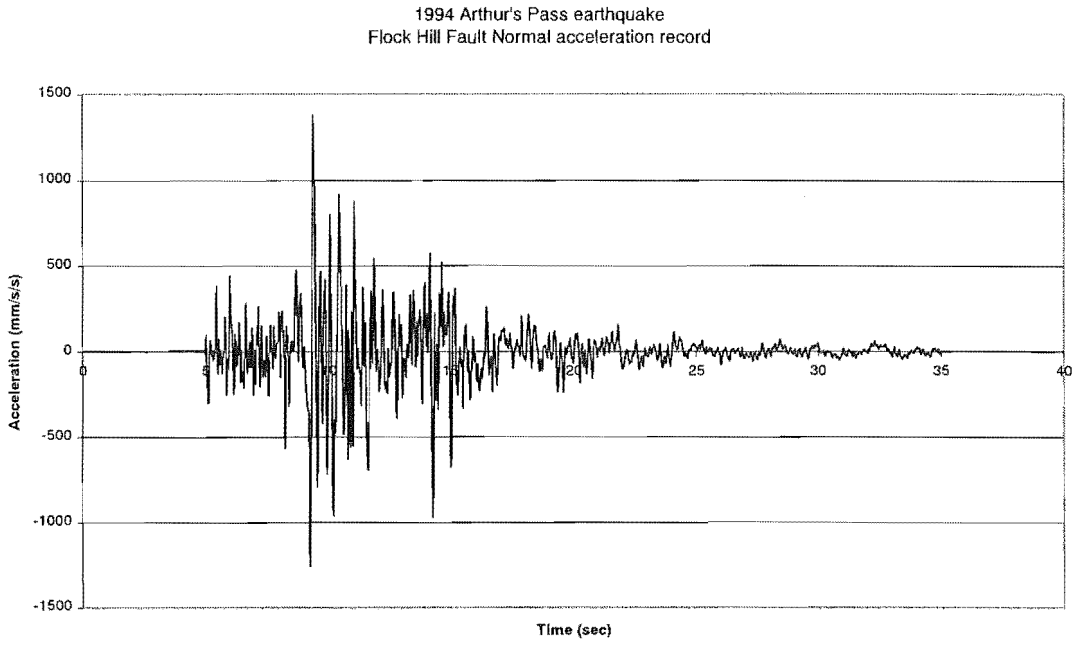

Figure 4-13 Flock Hill fault normal acceleration record

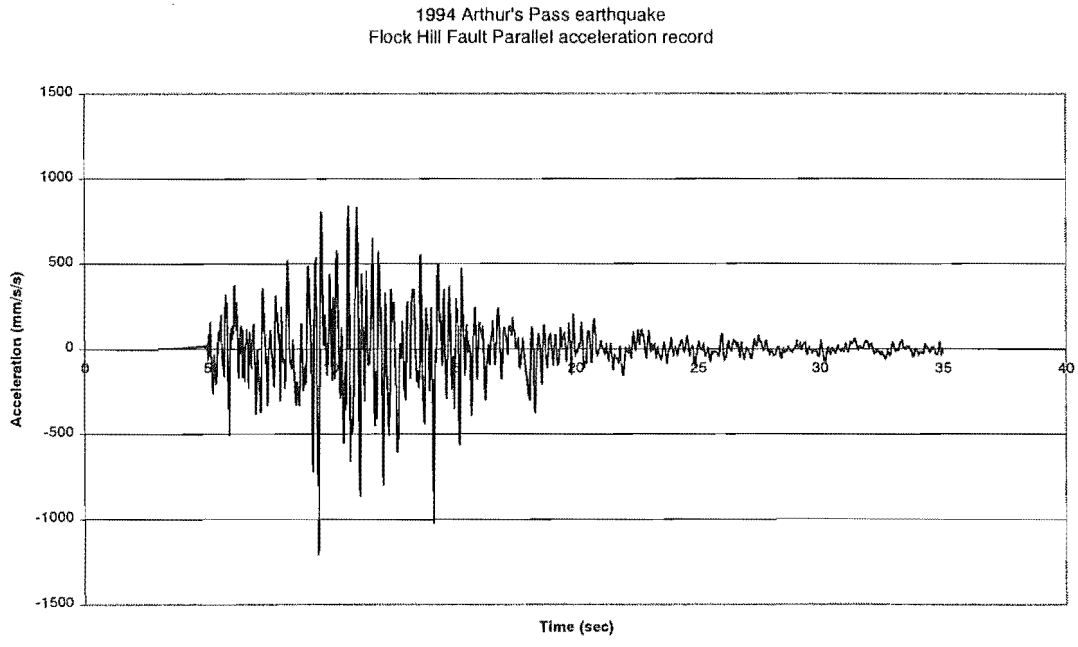

Figure 4-14 Flock Hill fault parallel acceleration record

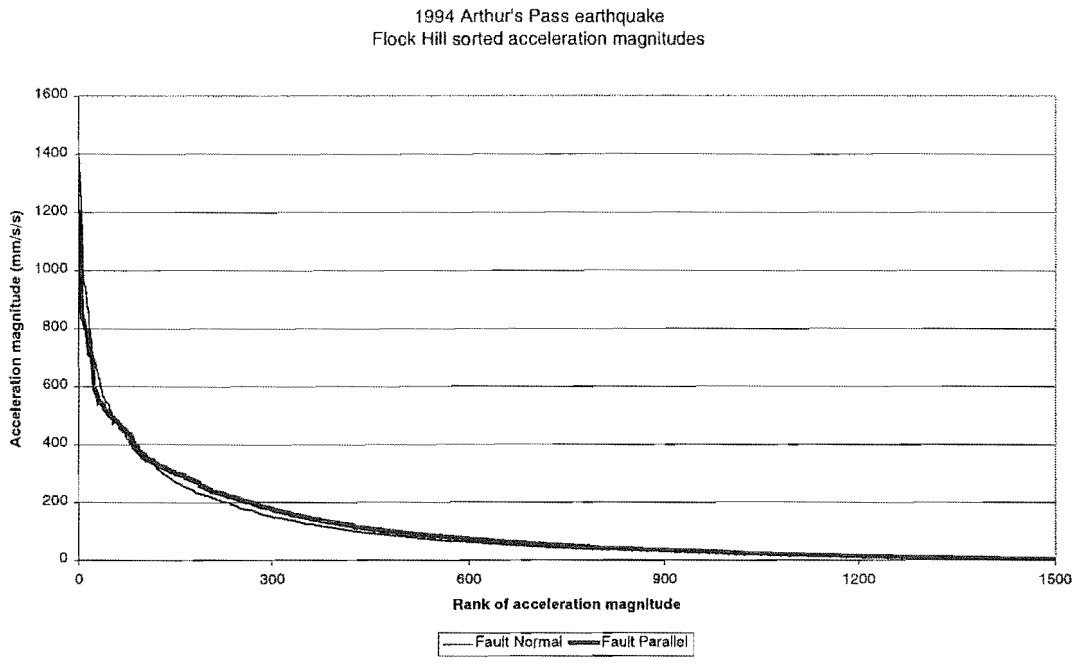

Figure 4-15 Flock Hill sorted acceleration amplitudes

4.4.2 Velocity records

Like the acceleration record, the velocity peaks are again located at the beginning of the strong motion part of the record, consistent with the presence of forward rupture directivity effects (Somerville 1996). Figures 4-16 and 4-17 show that the fault normal peak, 86 mm/s at 9.32 seconds that is smaller than the fault parallel peak of 101 mm/s at 9.58 seconds. Forward rupture directivity effects are expected to generate larger amplitudes in the fault normal direction; the peak velocity in the fault parallel direction is inconsistent with the presence of forward rupture directivity effects at the site.

Examination of the acceleration recordings show that, at the time of the peak fault parallel velocity, accelerations in the fault parallel direction have lower amplitudes than those in the fault normal. The fault parallel accelerations at the time are consistently in one direction, however, and this produces the peak velocity. This peak velocity may not therefore be due to rupture directivity effects, but to the coherency in the fault parallel accelerations. The Fourier spectra presented in Chapter 5 show that

the longer period fault parallel Fourier amplitudes at the Flock Hill site are significantly greater than the fault normal, consistent with a larger peak velocity in the fault normal direction.

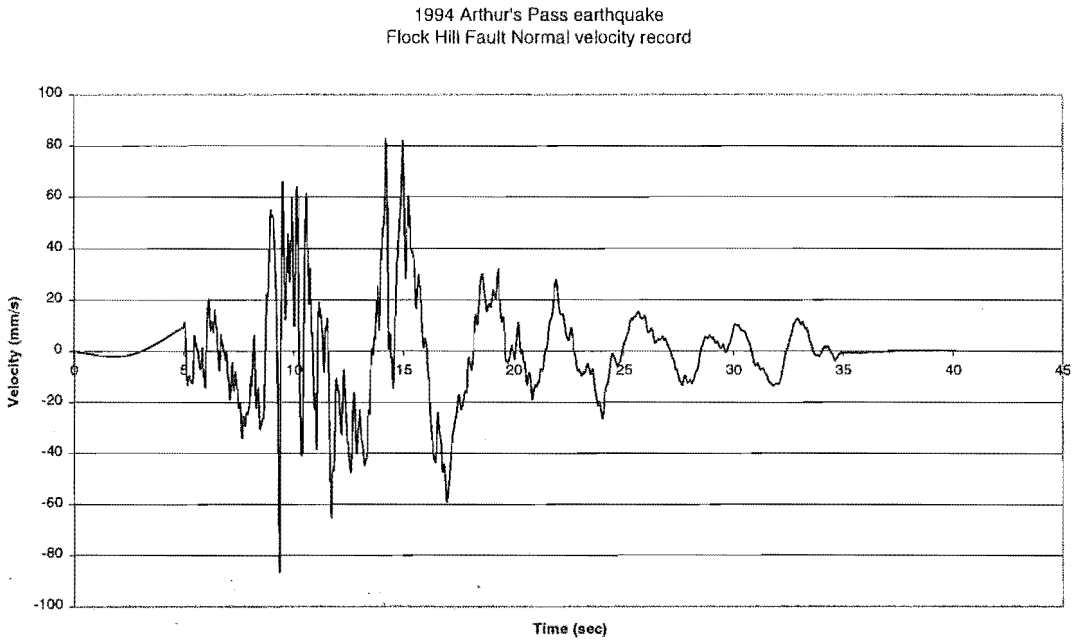

Figure 4-16 Flock Hill fault normal velocity record

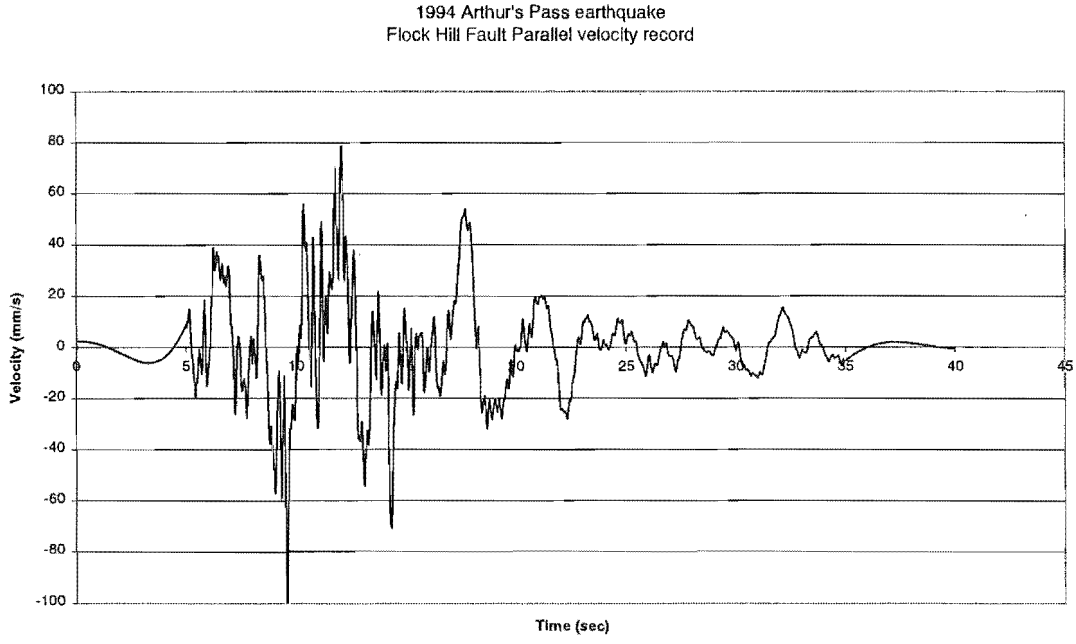

Figure 4-17 Flock Hill fault parallel velocity record

From Figure 4-18, it is apparent that the four largest fault parallel velocity amplitudes are greater than those in the fault normal direction. Aside from these initial points, the fault normal direction exhibits consistently larger velocity amplitudes than the fault parallel. This is a similar pattern to that observed in Figure 4-15, the sorted acceleration amplitudes, but with the directions reversed. Here, the fault parallel direction exhibits the largest values, but the fault normal shows larger values over most of the record.

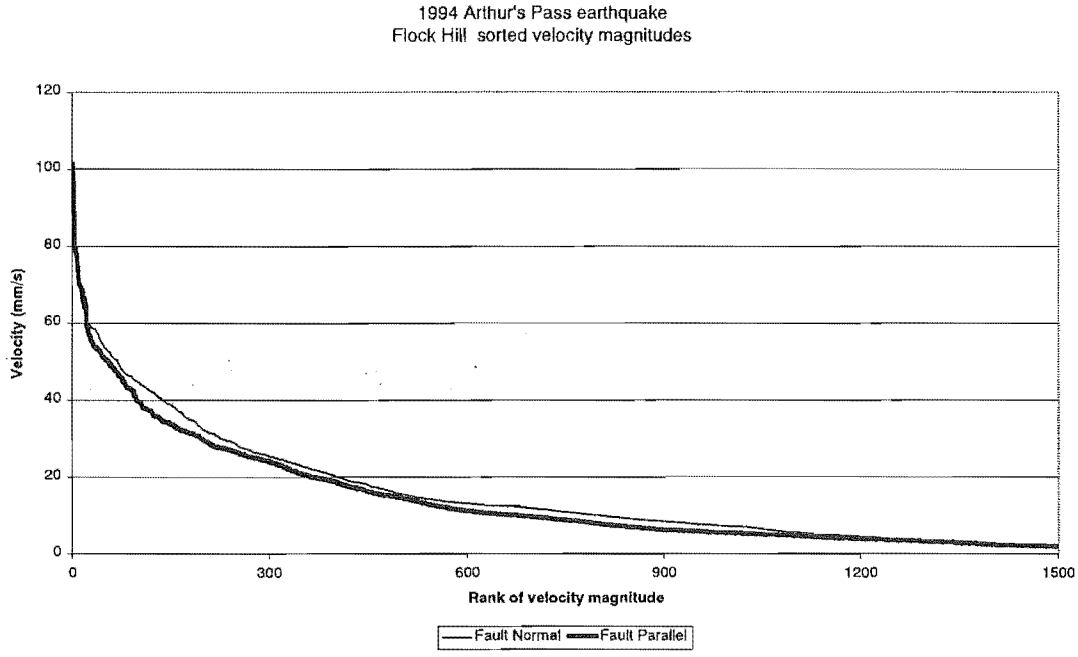

Figure 4-18 Flock Hill sorted velocity amplitudes

4.4.3 Displacement record

Peak displacements occur late in the displacement recording, shown in Figure 4-19. The fault normal peak was 36 mm at 16.06 seconds, the fault parallel peak was 32 mm at 12.78 seconds. Ground displacements have exhibited evidence of forward rupture directivity effects in past earthquakes, but this is not the case here as the peaks are not in the initial ground motion. Displacements recorded at the site are not characteristic of forward rupture directivity effects, even though the peak displacement is in the fault normal direction (which is expected).

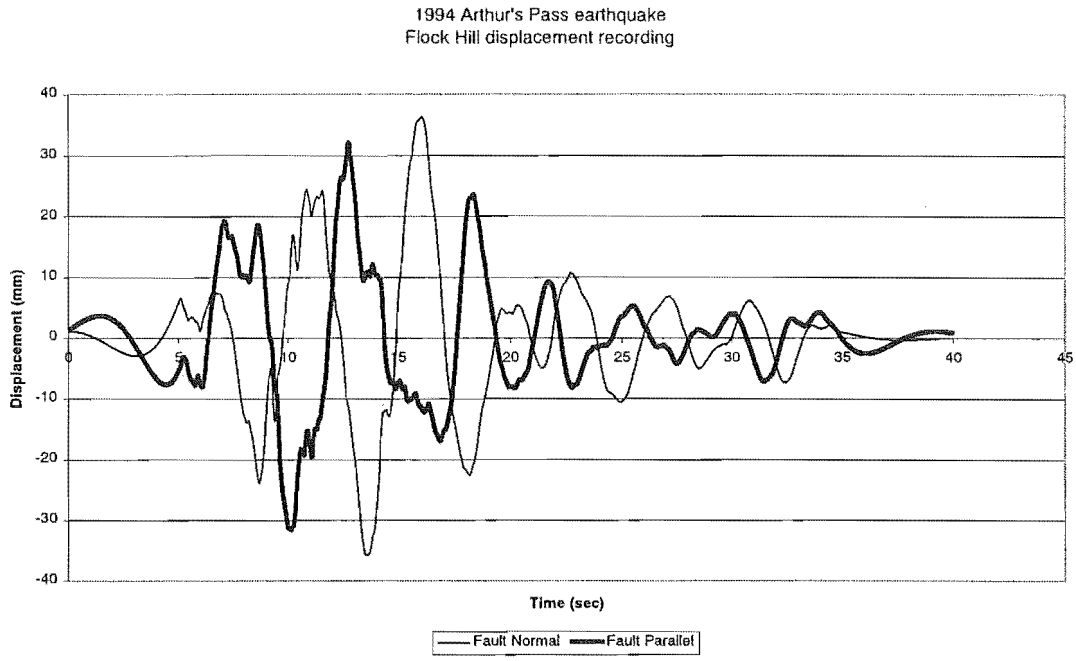

Figure 4-19 Flock Hill displacement recordings

4.4.4 Strong ground motion duration

Table 4-4 shows that there is a significant difference in the strong ground motion duration in the two directions. The fault normal duration is significantly shorter than the fault parallel, an observation that is consistent with the site being affected by forward rupture directivity effects. This is also consistent with the fault normal direction exhibiting a significantly larger peak acceleration than the fault parallel. As well as this, the duration of the strong motion is less than that recorded at Arthur's Pass.

Component	FN	FP	Total
Duration (sec)	8.32	11.14	9.92

Table 4-4 Flock Hill strong motion duration

4.4.5 Summary

Some of the observations made at the Flock Hill site may be construed to be evidence of forward rupture directivity effects caused by rupture on the assumed fault plane. These effects are the large fault normal acceleration peak at the beginning of the strong motion part of the record, the significantly shorter duration in the fault normal direction, and the duration of strong ground motion with respect to the Arthur's Pass recording. The large peak in the fault parallel direction at the beginning of the velocity record, and the displacement records, however, are inconsistent with forward rupture directivity effects (Somerville, 1996).

4.5 Greymouth

4.5.1 Acceleration records

Because of the distance from the site to the epicentre (69km), Greymouth was to be an example of a site that was not affected by rupture geometry and that should exhibit isotropic ground motion. This was not the case, as the recorded motion at the site was anisostropic. The anistropy of ground motion is probably due to the nature of the soft layers at the site, which are oriented in a long strip parallel to the shoreline. The wedge of sediment could amplify ground motion parallel to the shoreline, an effect that is discussed in more detail in Chapter 7.

Figures 4-20 and 4-21 show the acceleration records from Greymouth. The peak accelerations in the fault normal and fault parallel directions are 457 mm/s/s and 430 mm/s/s at times of 12.16 seconds and 22.16 seconds respectively. Despite their similar peak accelerations, records from the two directions are quite different. The sorted acceleration records, in Figure 4-22 show a very significant difference between the two directions. Apparent differences in the two directions are magnified as the ground motion amplitudes are low.

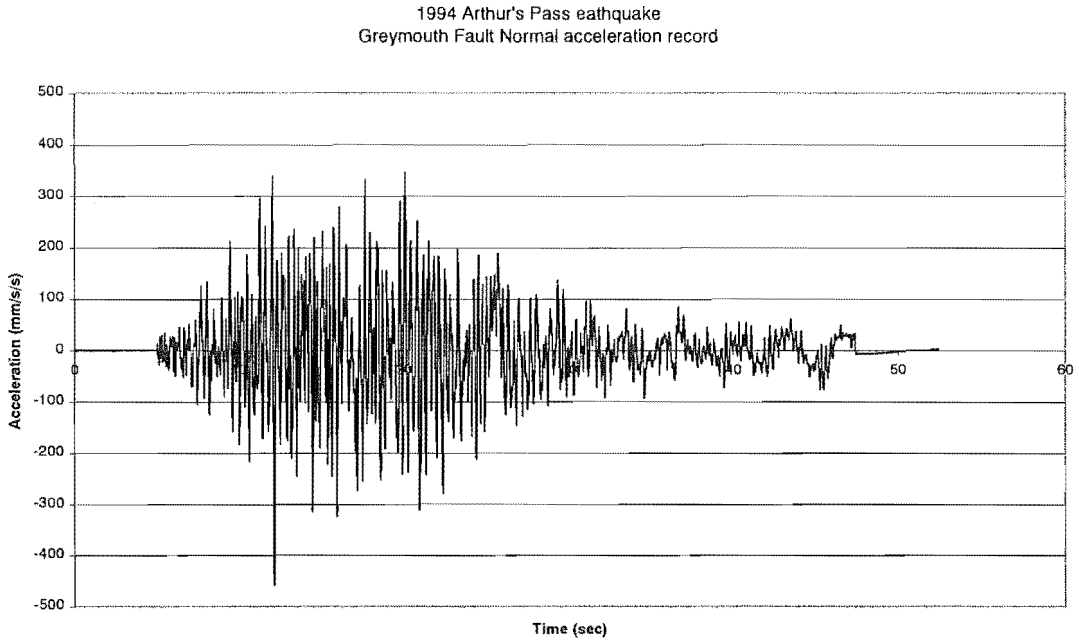

Figure 4-20 Greymouth fault normal acceleration record

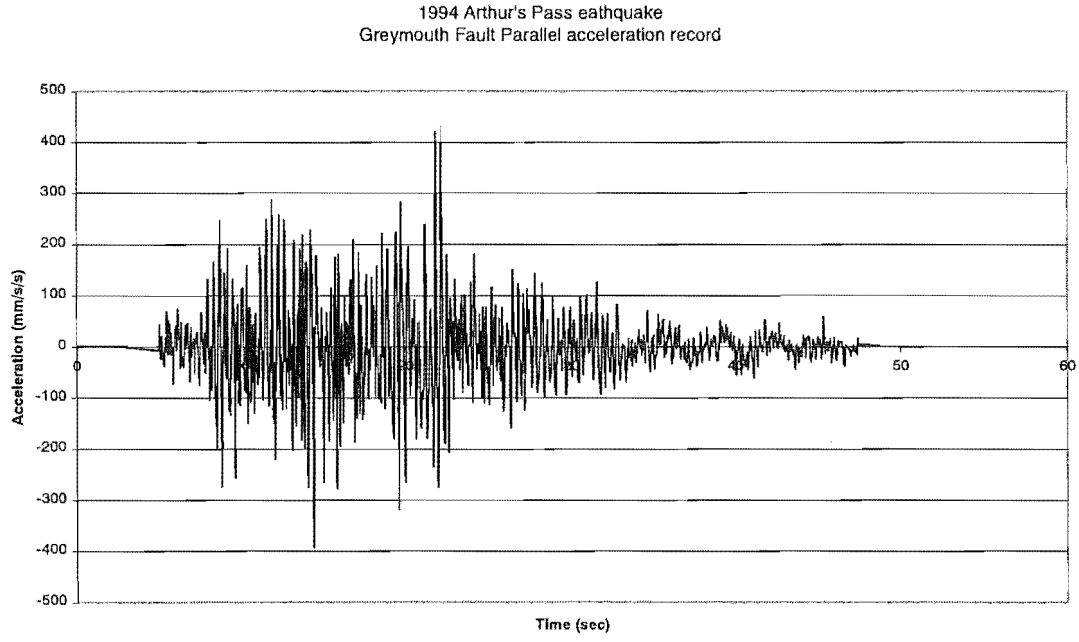

Figure 4-21 Greymouth fault parallel acceleration record

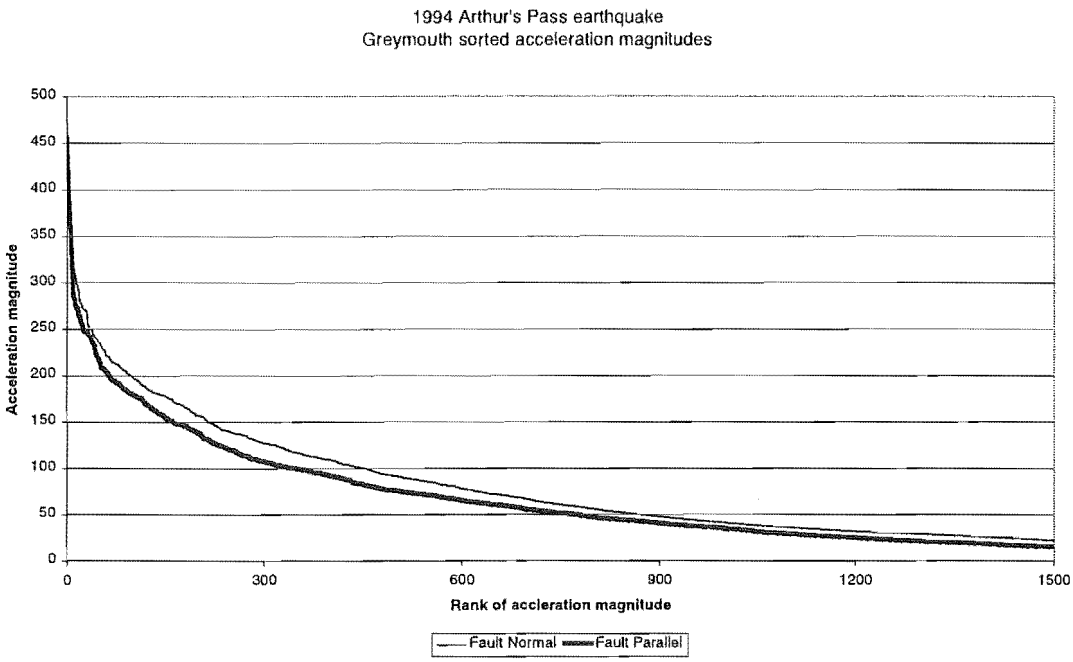

Figure 4-22 Greymouth sorted acceleration amplitudes

4.5.2 Velocity records

Figure 4-23 shows that at the tail end of the fault normal velocity record there is a peak-trough shape, between 44 and 47 seconds, that is significantly larger in amplitude than other velocities around that time. Inspection of Figure 4-20, the acceleration-time plot, does not identify any noticeable shape that may have caused this. Fault normal accelerations at the time of the peak-trough shape are neither noticeably coherent, nor excessively large in amplitude. The peak-trough shape is unusual both in the coherency of the shape, and the amplitude of the peaks, and is not present in Figure 4-24, the fault parallel velocity record.

Figure 4-25 shows that the fault normal velocities are significantly greater than the fault parallel. While the peak fault normal velocity, 42 mm/s at 26.08 seconds, is similar to the fault parallel peak of 37 mm/s at 22.10 seconds, the two records are shaped differently.

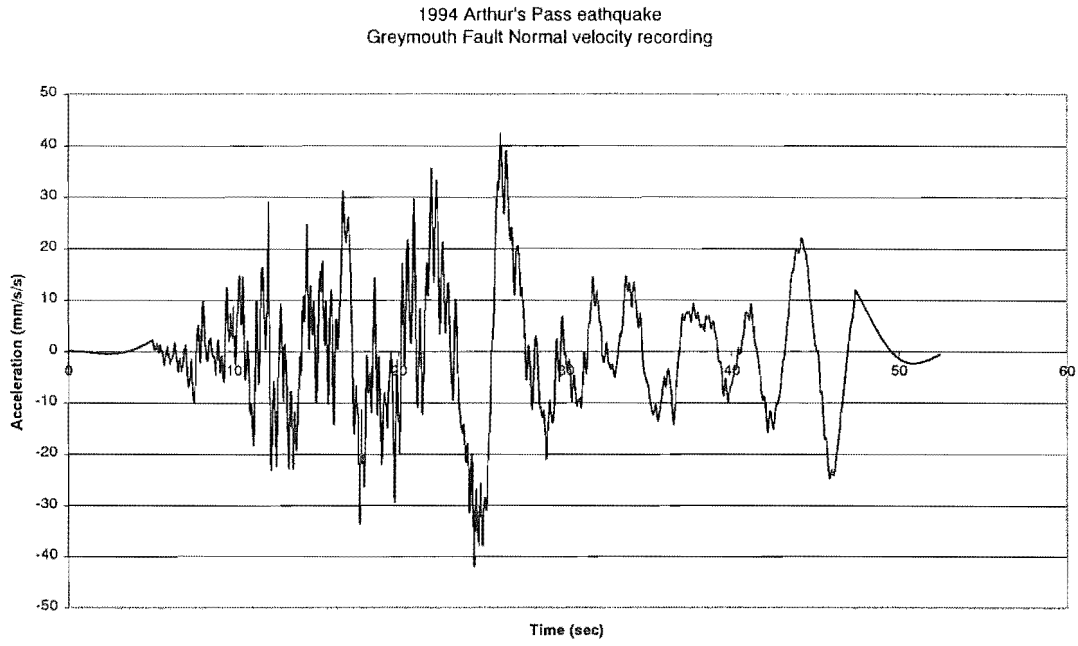

Figure 4-23 Greymouth fault normal velocity recording

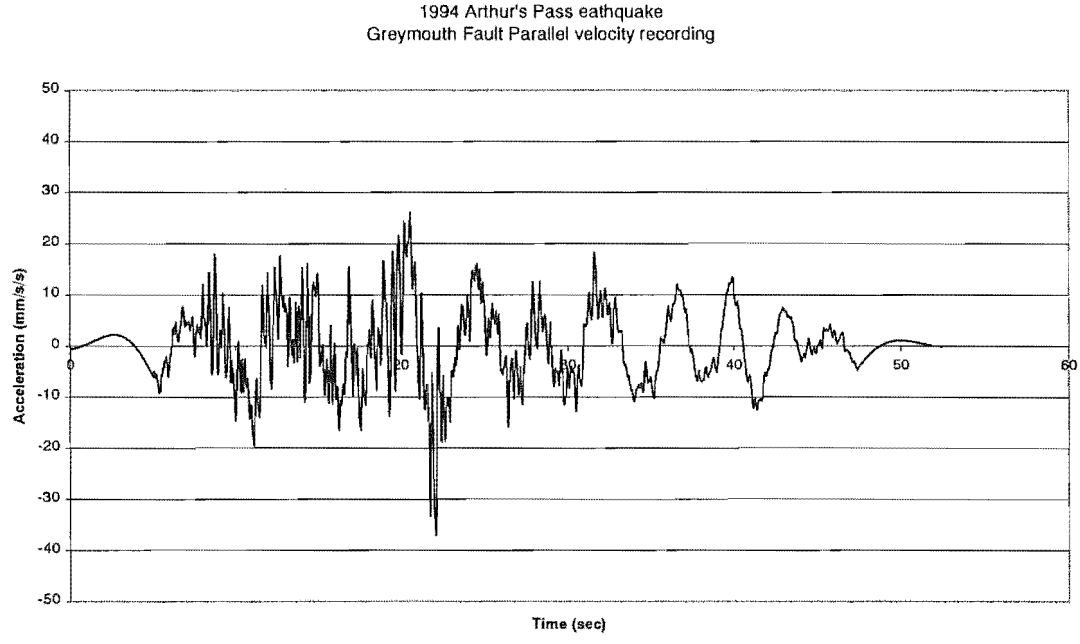

Figure 4-24 Greymouth fault parallel velocity recording

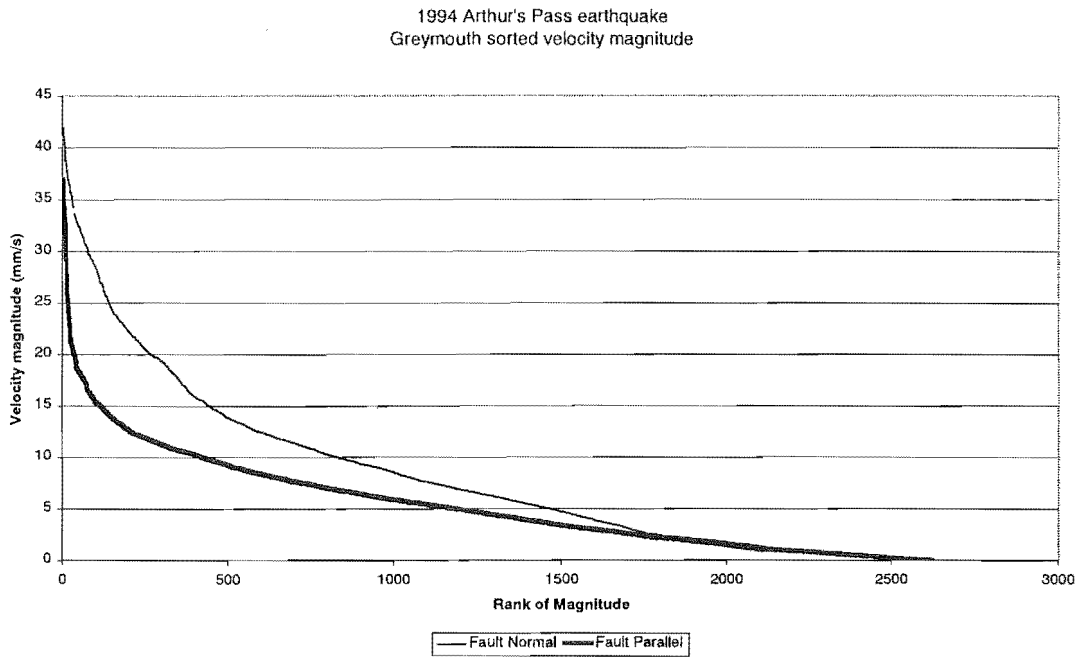

Figure 4-25 Greymouth sorted velocity amplitudes

4.5.3 Displacement records

Figure 4-26 shows the peak displacement, 28.8 mm at 25.7 seconds in the fault normal direction, is significantly larger than the peak fault parallel displacement, 14.5mm at 21.08 seconds. Significant differences in the two directions are highlighted in this chart. The large peak at 25 seconds in the fault normal direction dominates the record, coinciding with the peak velocity in the fault normal direction. The peak-trough shape that was noted in the fault normal velocity recording is again present in Figure 4-26.

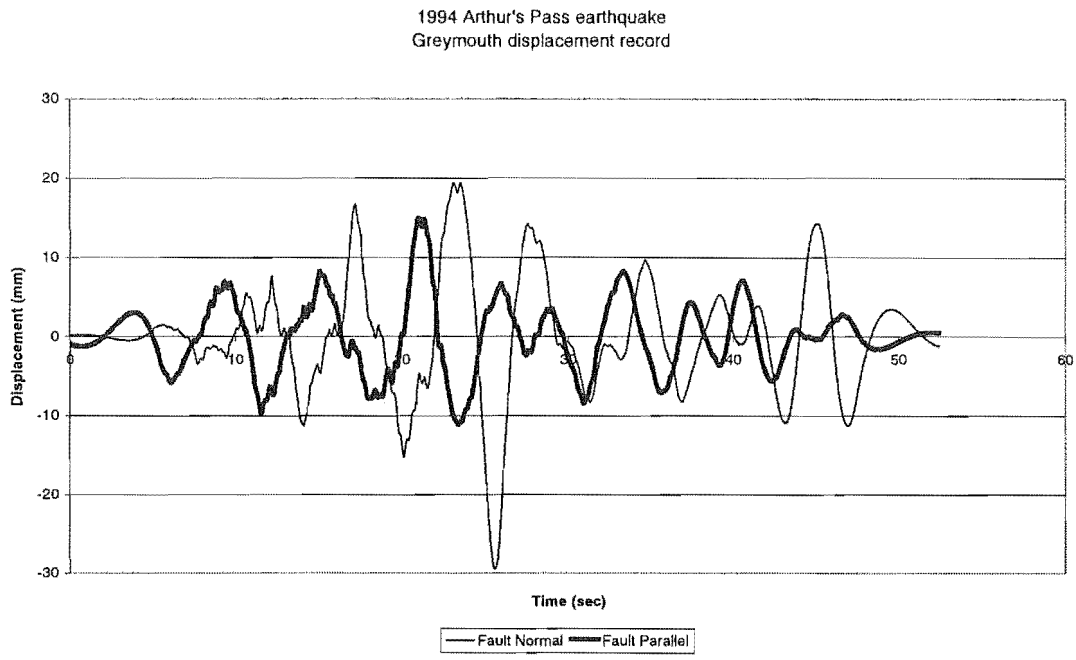

Figure 4-26 Greymouth displacement records

4.5.4 Summary

The Greymouth recordings are not affected by the fault rupture geometry due to their distance from the fault (Somerville, 1996, Somerville et al., 1997). The significant differences in the two directions are therefore due to another effect, possibly due to the orientation of the soft layers at the site, an effect that is discussed in more detail in Chapter 7.

5 Fourier Spectra

Forward rupture directivity effects are expected to become significant at periods longer than 0.5 seconds (Somerville, 1996) or 1.0 seconds (Somerville et al., 1997). Resolution of earthquake waveforms into their harmonic components by Fourier analysis should show the effects of this long period coherency by depicting differences in the two directions. This coherency is expected to increase with increasing natural period (Kasahara, 1981; Lay and Wallace, 1995). Because of this coherency, Fourier amplitudes are presented as a function of period rather than frequency. Forward rupture directivity effects are again expected to boost the fault normal intensities (Somerville, 1996), and hence the Fourier amplitudes. A Fourier analysis was therefore carried out on acceleration records in the fault normal and fault parallel directions.

The Fourier analysis used was the fast Fourier variant of the discrete Fourier transform. The discrete Fourier equation used is presented as Equation 5-1, the frequency in Equation 5-2, and the period presented as Equation 5-3. The Fast Fourier Transform tool, part of Microsoft Excel 97 SR-2, was used to analyse the ground motion records.

$$X(\omega_n) = \Delta t \sum_{k=1}^{N} [x(t_k)\cos(\omega_n t_k) - ix(t_k)\sin(\omega_n t_k)] \qquad \text{Equation 5-1}$$

$$\omega_n = n\Delta\omega = \frac{2\pi n}{N}\Delta t \qquad \text{Equation 5-2}$$

$$T = \frac{2\pi}{\omega_n} = \frac{N}{n\Delta t} \qquad \text{Equation 5-3}$$

Where:

$\Delta t = 0.02$ seconds;

$x(t_k)$ = Acceleration recording (mm/s/s)

$X(\omega_n)$ = Fourier output (in $a+bi$ form)

5.1 Arthur's Pass Police Station

When the fault normal and fault parallel Fourier amplitudes shown in Figures 5-1 and 5-2 are presented in linear-log form, differences in the two directions are hard to differentiate. Both have peaks at around the same period (0.6 seconds), although the amplitude of the two peaks is different, with the fault parallel being larger. The two plots are combined in Figure 5-3 to directly show the relationship between the two components.

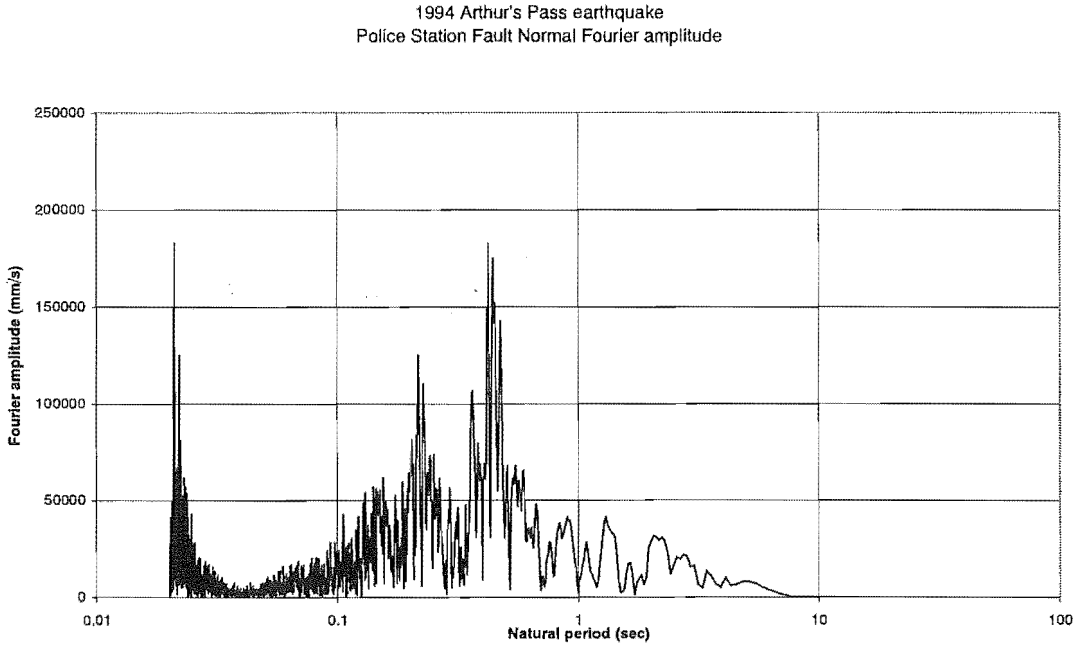

Figure 5-1 Arthur's Pass fault normal Fourier amplitudes

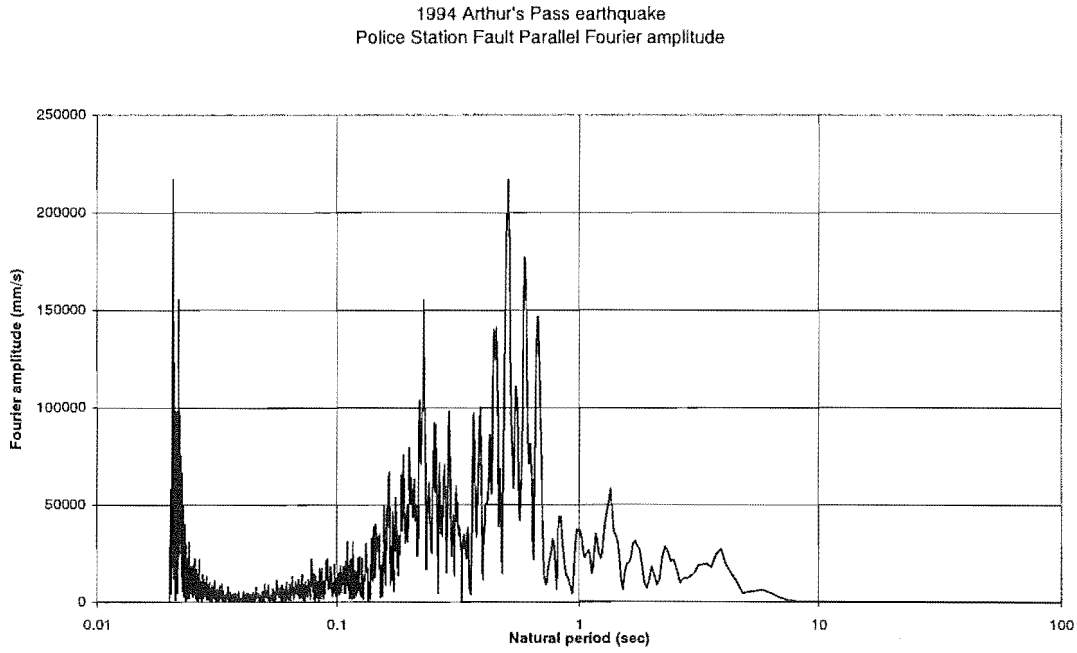

Figure 5-2 Arthur's Pass fault parallel Fourier amplitudes

At periods longer than around 0.8 seconds, the components exhibit similar Fourier amplitudes. Through the main part of the record, from about 0.4 to 0.8 seconds, the fault parallel direction clearly exhibits significantly greater Fourier amplitudes. These natural periods were not expected to generate significant differences in the two directions (Somerville et al., 1997).

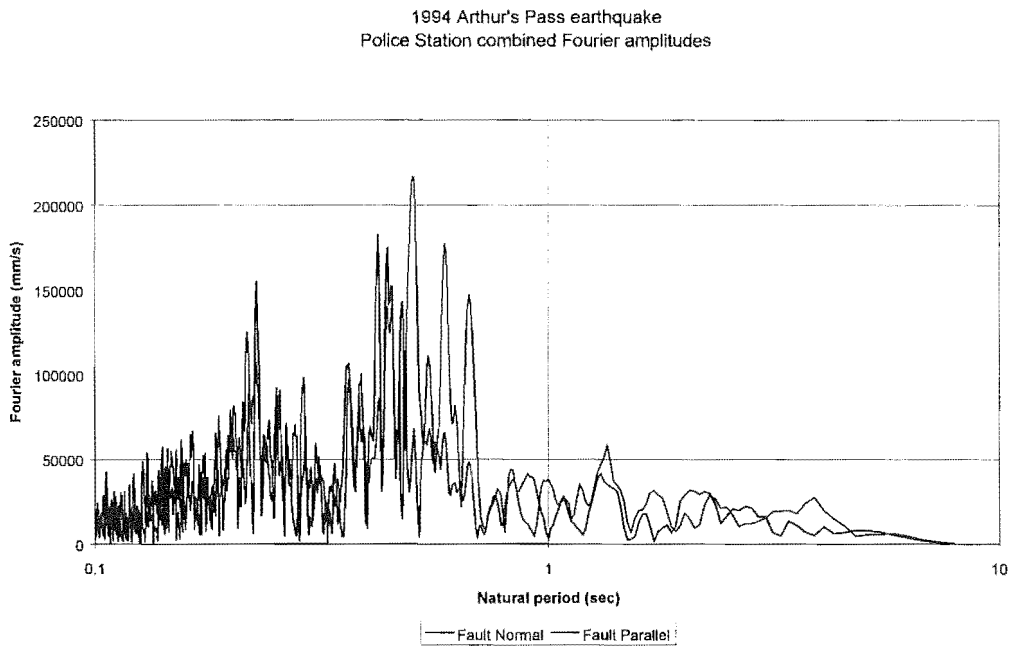

Figure 5-3 Arthur's Pass combined Fourier amplitudes

The average Fourier amplitude for different period ranges are compared, and presented in Table 5-1. The fault parallel direction at longer periods exhibits larger amplitudes, an observation that is inconsistent with forward rupture directivity effects. The fault normal direction is 13% lower in amplitude than the fault parallel for periods longer than 0.8 seconds. For the rest of the record the two directions exhibit similar Fourier amplitudes over the entire period range. Higher amplitude fault parallel Fourier amplitudes are consistent with results from Chapter 4, where the fault parallel ground motion intensities were generally stronger than the fault normal.

Average Fourier Amplitude:	FN	FP	% Difference
Entire	17892	17793	0.6
T>0.8	17542	20140	-12.9
T<0.25	16150	15175	6.4

Table 5-1 Arthur's Pass Fourier amplitudes

Figure 5-4, the ratio of fault normal and fault parallel Fourier amplitudes at Arthur's Pass, shows that the fault normal Fourier amplitude is slightly greater than the fault parallel for periods greater than 0.8 seconds. This results in a low FN/FP ratio, inconsistent with the presence of forward rupture directivity effects, where greater coherency, and thus a larger ratio is expected with increasing period.

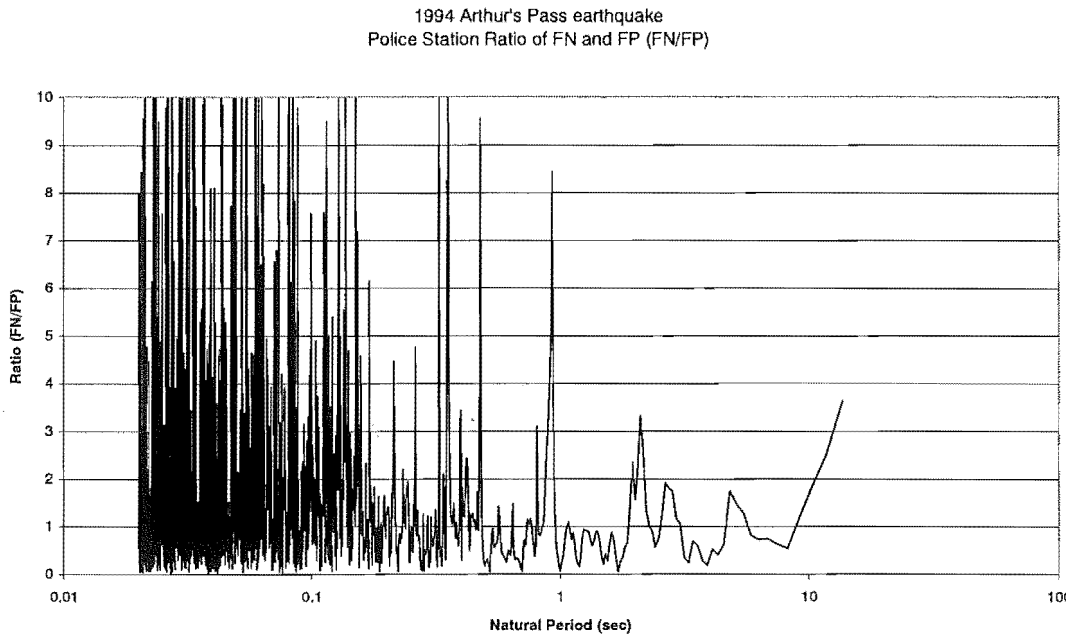

Figure 5-4 Arthur's Pass ratio of Fourier amplitudes

Figure 5-5, the plot of residuals shows a similar pattern to that of the ratios. At periods greater than 0.8 seconds the fault parallel Fourier amplitudes are significantly greater than the fault normal. The largest difference occurs at a period of 0.8 seconds. Over the entire period range considered, however, neither the fault normal nor fault parallel directions differs significantly (a difference of 0.6% is insignificant). A rupture on the assumed fault plane has therefore not generated significant forward rupture directivity effects at the Arthur's Pass site, a result that is consistent with what was expected.

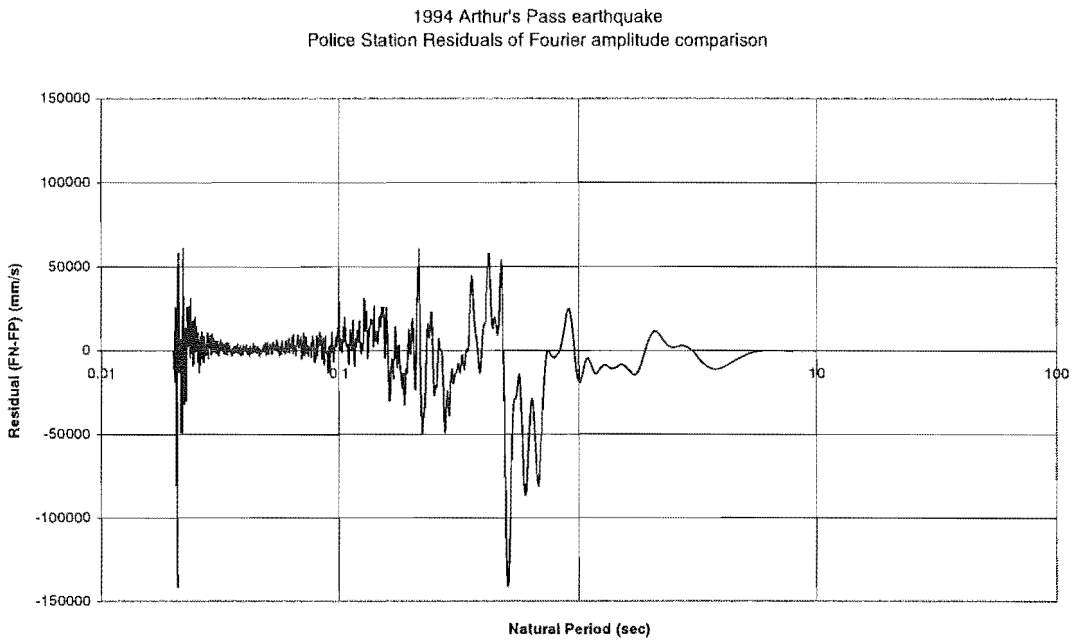

Figure 5-5 Arthur's Pass residuals of Fourier amplitudes

5.2 Flock Hill

The model applied in Chapter 8 predicts that the fault normal Fourier amplitudes will be larger than those of the fault parallel if the rupture occurred on the assumed fault plane. This is generally what is observed in Figures 5-6, 5-7 and 5-8, where the fault parallel component of the Fourier amplitudes is often smaller than the fault normal, especially at longer periods. The two records do have some differences, however, with the fault parallel direction exhibiting a large peak at a period of around 2 seconds. This peak may be due to the natural resonance of the site in the fault parallel direction. It also appears in the fault parallel response spectra.

The differences identified at this site are not as great as those found by Somerville (1996) in some Kobe or Northridge records. One possible reason for this is that the records used in his analysis were from sites that were significantly closer to the fault than the Flock Hill recording station, and located more directly in the path of the rupture front. In addition, the actual fault plane may differ from that used in the analysis.

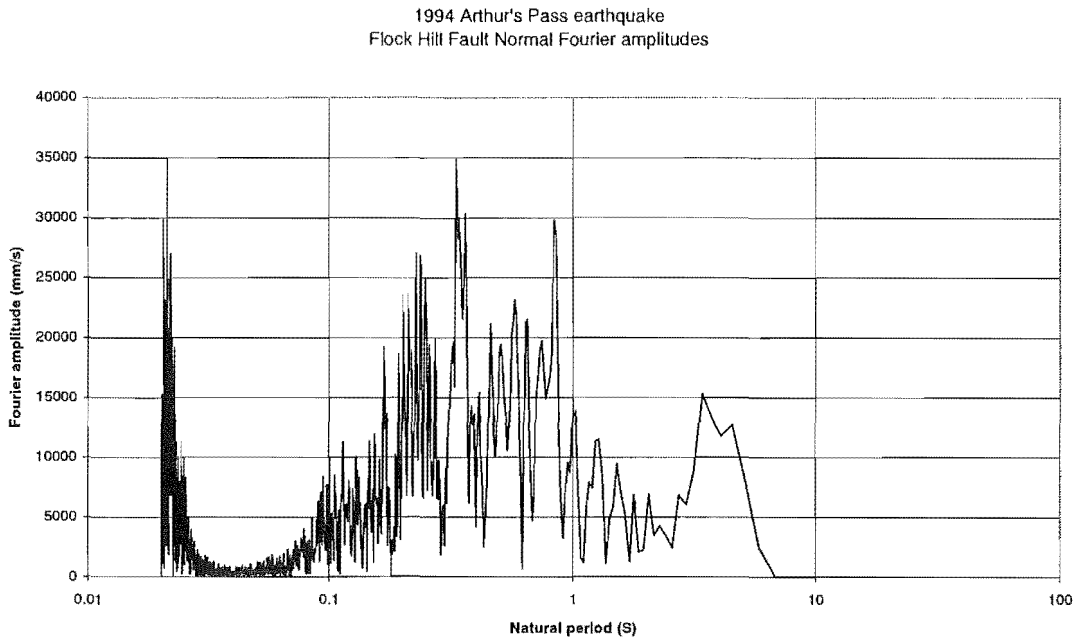

Figure 5-6 Flock Hill fault normal Fourier amplitudes

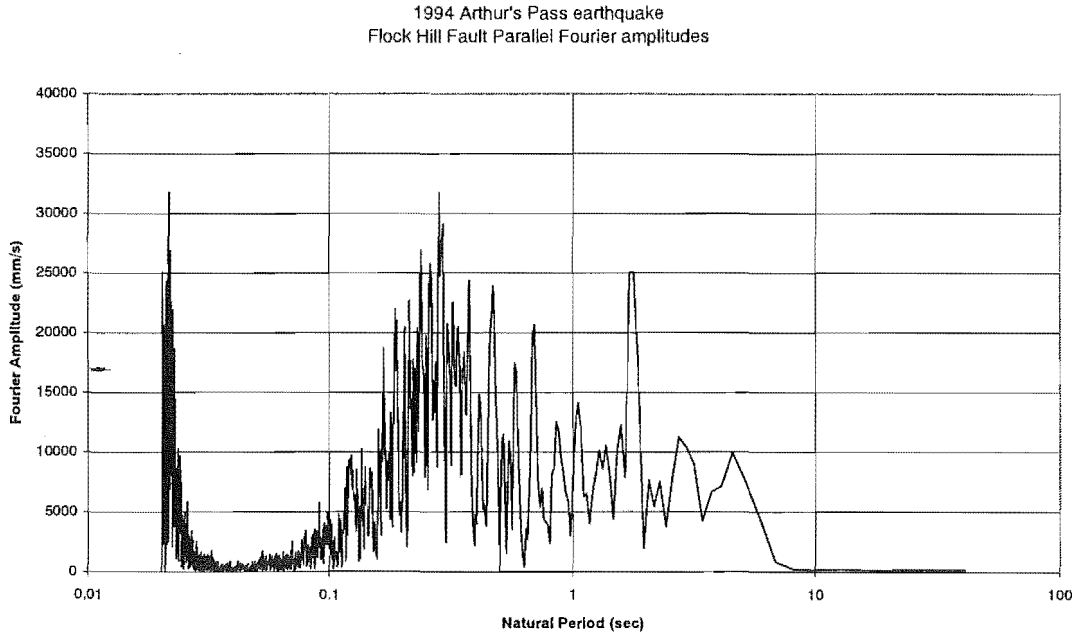

Figure 5-7 Flock Hill fault parallel Fourier amplitudes

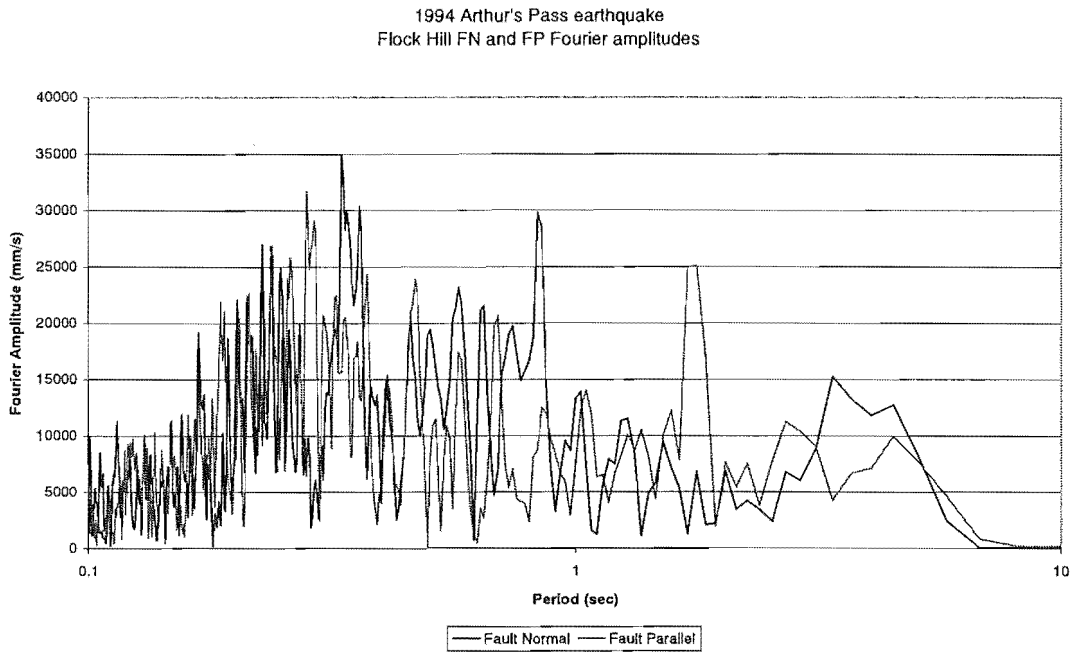

Figure 5-8 Flock Hill Fourier amplitudes

Table 5-2 shows the differences in Fourier amplitudes in the two directions. Over the entire record, fault normal amplitudes are 6% greater than the fault normal. This difference increases to 17% when periods longer than 0.8 seconds are considered, and is only 3% for periods less than 0.25 seconds. No noticeable difference is therefore present in the low period range of the Fourier spectra. These results could be construed to be indicative of coherency at longer periods, possibly due to forward rupture directivity effects. The model applied in Chapter 8 predicted larger fault normal than fault parallel components. This is consistent with these results.

Average Fourier Amplitude:	**FN**	**FP**	**% Difference**
Entire	4491	4219	6.4
T>0.8Sec	9006	7713	16.8
T<0.25Sec	9366	9139	2.5

Table 5-2 Flock Hill Fourier amplitudes

Figure 5-9 presents the ratio of the fault normal and fault parallel Fourier amplitudes. At periods longer than 0.8 seconds the fault normal component is generally larger than the fault parallel, resulting in ratios less than unity. This observation could indicate the presence of forward rupture directivity effects at the site.

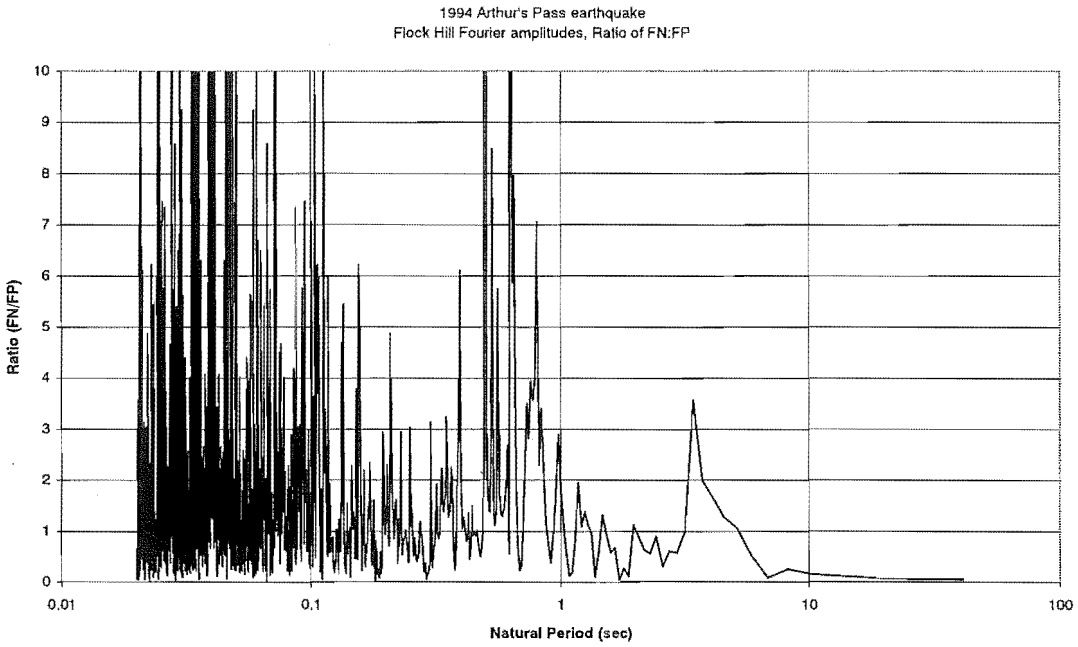

Figure 5-9 Flock Hill ratio of Fourier amplitudes

The residual Fourier amplitudes presented in Figure 5-10 do not show any clear pattern of coherent interference at longer periods. Table 5-2 has suggested that longer period Fourier amplitudes have larger amplitude fault normal components, and this was seen in Figure 5-9, but this difference is not clear in this representation.

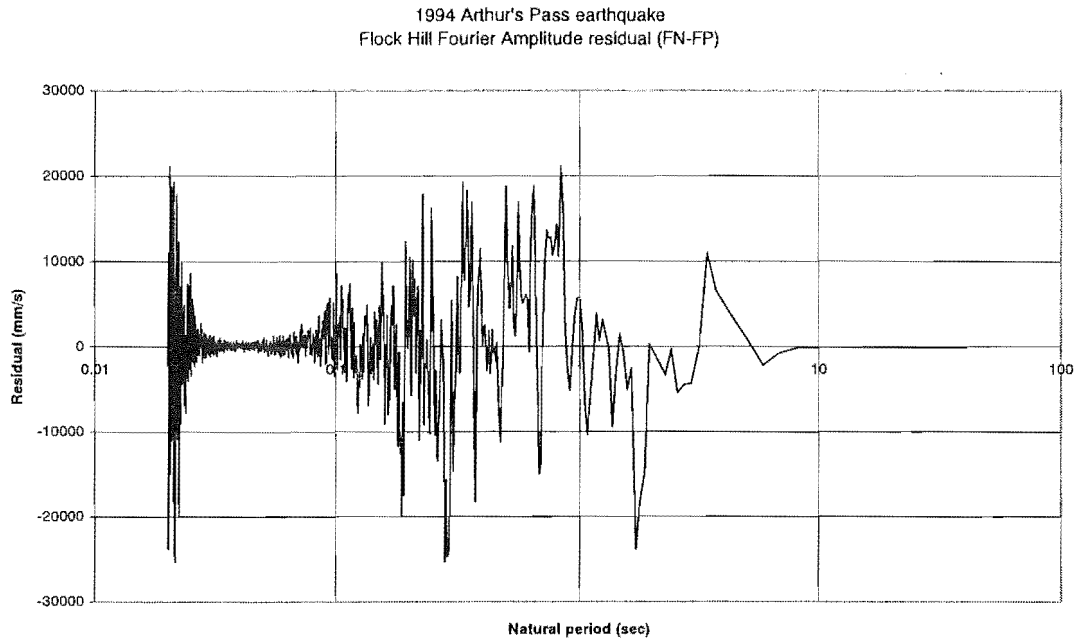

Figure 5-10 Flock Hill residual of Fourier amplitudes

5.3 Greymouth record

Figures 5-11 to 5-13 show that the fault normal Fourier amplitudes are significantly greater than the fault parallel. The period range longer than 1.0 seconds shows this clearly in Figure 5-13. The Greymouth site is strongly affected by site geometry and this is the most likely reason for the significant differences present. Path effects are expected to dominate the site input ground motion so much that fault geometry should have little effect. A full discussion of site effects at the Greymouth site is presented in Chapter 7.

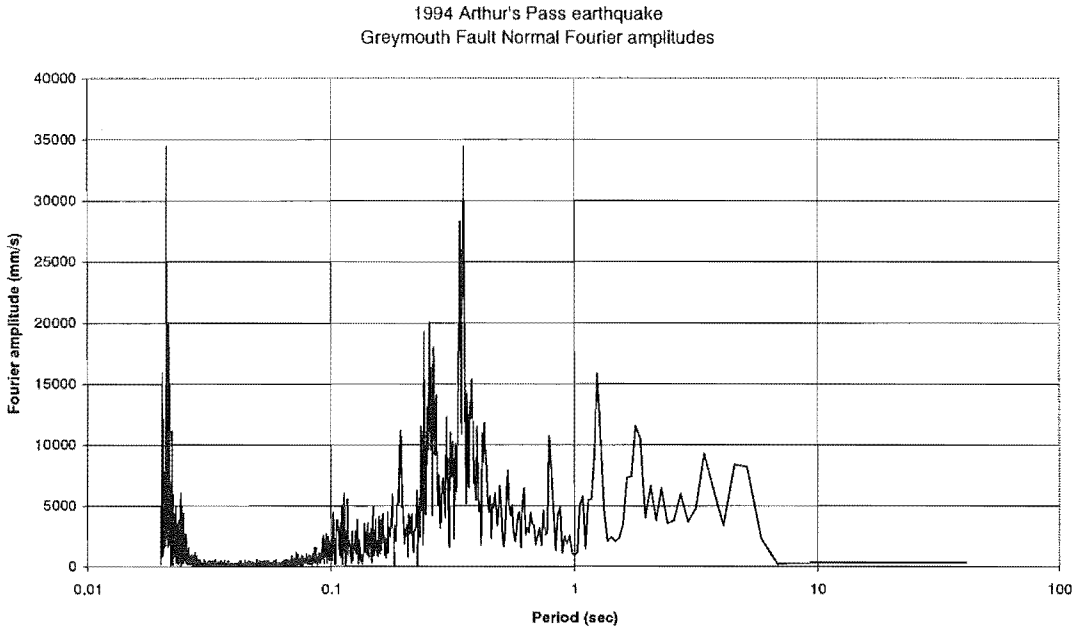

Figure 5-11 Greymouth fault normal Fourier amplitudes

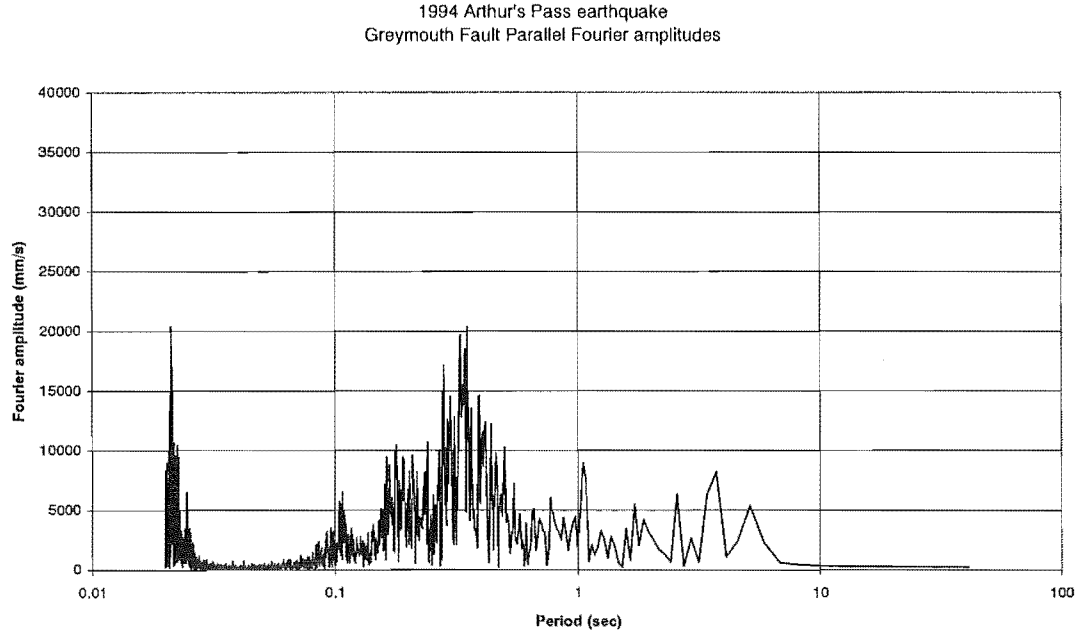

Figure 5-12 Greymouth fault parallel Fourier amplitudes

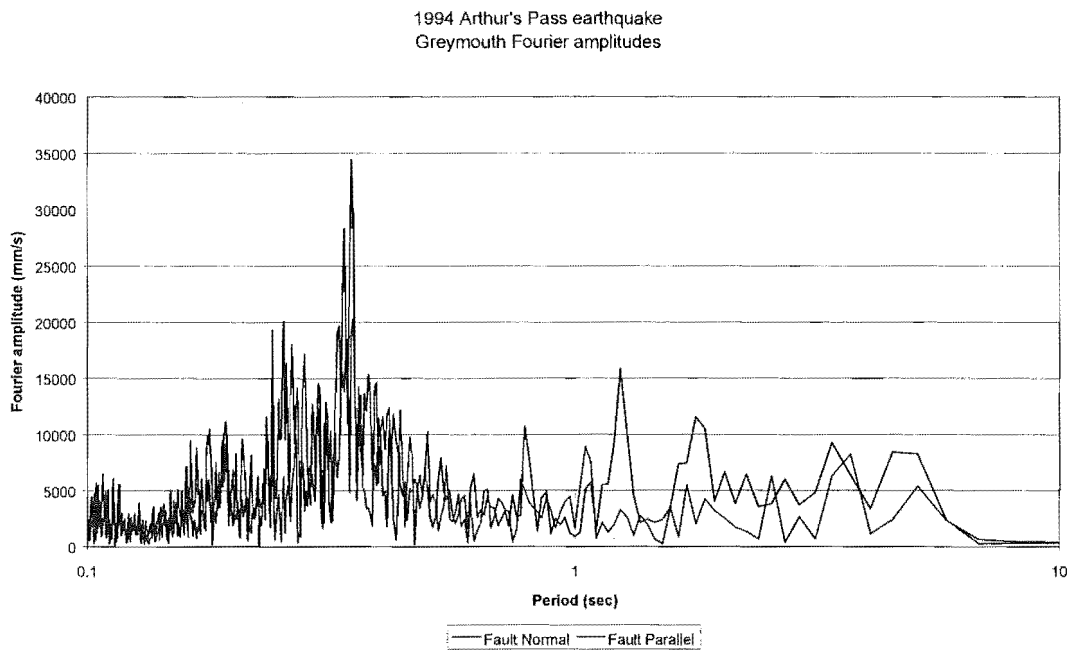

Figure 5-13 Greymouth Fourier amplitudes

Table 5-3 confirms the significant differences in the two directions at this site. The fault normal direction shows 49% greater shaking amplitude for periods greater than 0.8 seconds. This is a very large difference, and is most likely due to site effects. No differences are noticeable at short periods, where the natural period is less than 0.25 seconds.

Average Fourier Amplitude	FN	FP	% Difference
Entire	2034	1962	3.6
T>0.8	4515	2725	49.4
T<0.25	1604	1649	2.8

Table 5-3 Greymouth Fourier amplitudes

Figure 5-14 and Figure 5-15 show that long period Fourier amplitudes are greater in the fault normal direction. This is consistent with the results presented in Table 5-3. More information on the site effects that may have affected ground motion at the Greymouth site are presented in Chapter 7.

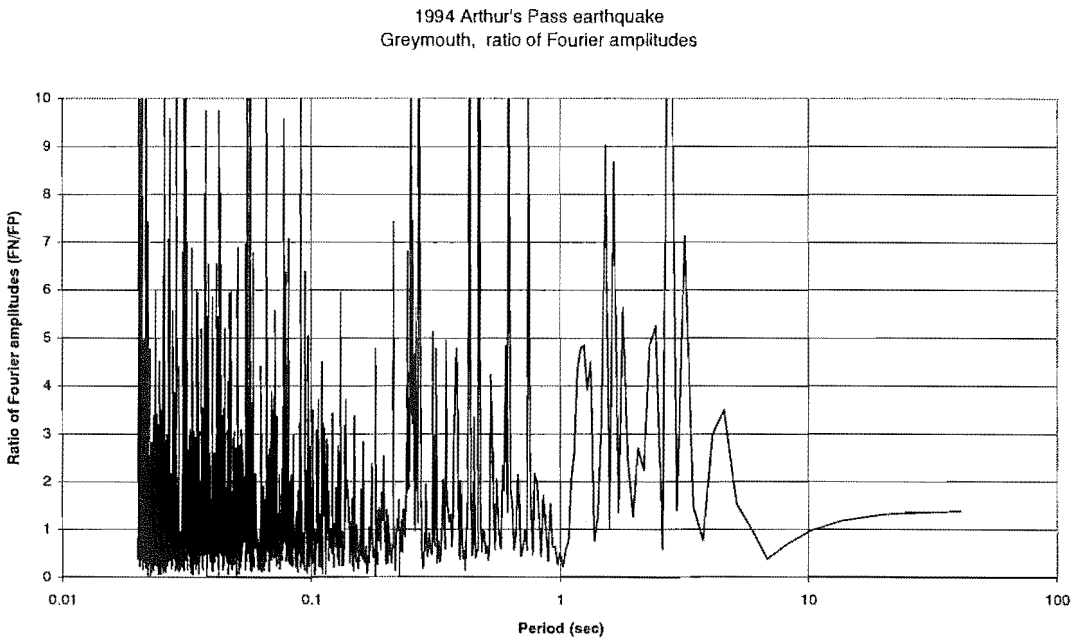

Figure 5-14 Greymouth ratios of Fourier amplitudes

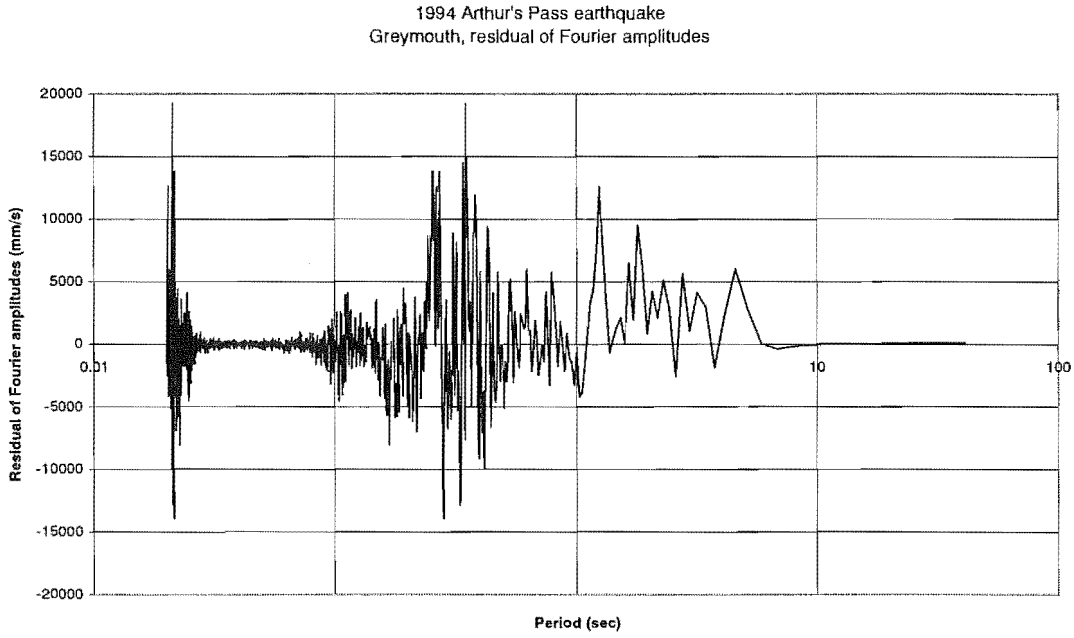

Figure 5-15 Greymouth residuals of Fourier amplitudes

6 Response Spectra

Fault normal and fault parallel acceleration records at different sites are used to generate 5% damped response spectra. The spectral acceleration, spectral velocity and spectral displacement were calculated from each acceleration record using the computer program SPECTRA. The spectra used have a natural period range of from 0.1 to 10 seconds at 0.05 second increments. As with the Fourier amplitude spectra, at longer natural periods the coherency of seismic waves was expected to increase. The amplitude of the response drops, however, as the period increases.

6.1 Arthur's Pass Police Station

6.1.1 Spectral acceleration

Figure 6-1 shows that the fault parallel spectral acceleration response is significantly greater than the fault normal below a period of 1.5 seconds. The peak spectral response, 14.3m/s^2 in the fault parallel direction is very high when compared to the 10.7m/s^2 peak in the fault normal direction. It is worth noting that this exceeds the peak design response of the New Zealand Standard, NZS 4203:1992, which specifies a peak response of 1g or 10 m/s^2 for rock sites. At the Arthur's Pass site, a site on soil type 'B', the largest response specified is 0.8g or 8 m/s^2. The peak response is therefore 75% greater than that specified by the code for that site.

Directivity effects usually predict that response at longer periods in the fault normal direction will be larger than the corresponding fault parallel response. Larger amplitudes in the fault parallel direction are consistent with the observations at the Arthur's Pass site in Chapters 4 and 5, the ground motion records and Fourier spectra.

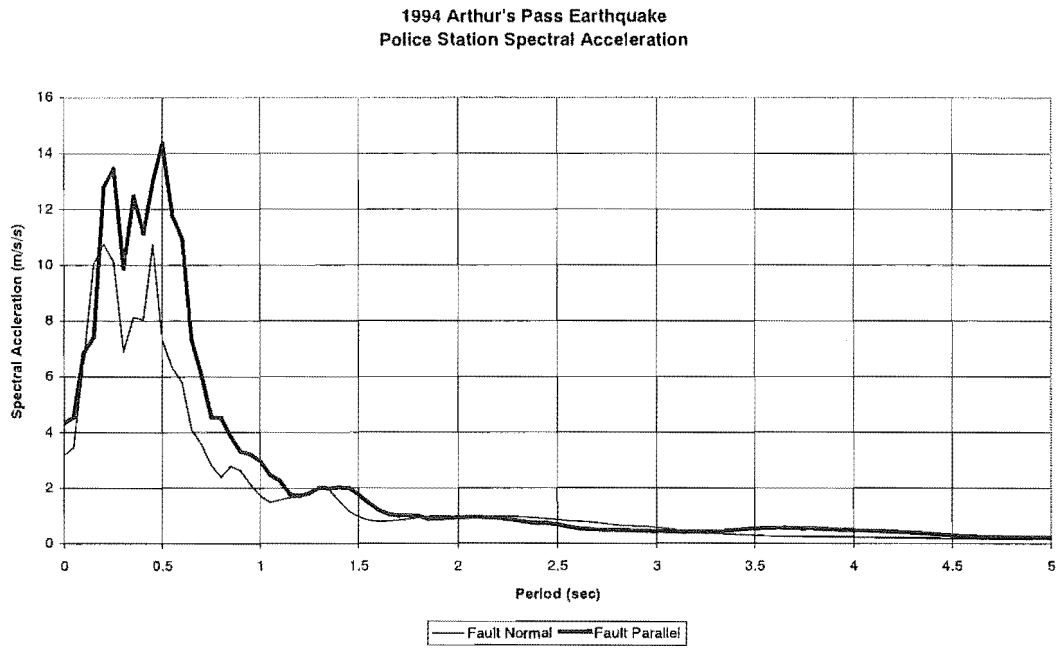

Figure 6-1 Arthur's Pass spectral acceleration

The ratio between fault normal and fault parallel spectral responses is shown in Figure 6-2. The differences in the fault normal and fault parallel acceleration response at longer periods are clear. At periods longer than 3.5 seconds the fault parallel acceleration response was significantly larger than the fault normal. The largest difference occurs at 2.7 seconds, while the smallest was located at a period of 3.7 seconds. These extreme ratios occur where there is a low amplitude of response, a result that highlights problems with using the ratio of the responses as an indicator.

All three spectral ratios are presented in the one chart as they are closely linked. The spectral acceleration and displacements are closely related, while the velocity follows the same general trend as the other two parameters. The peak ratios generally occur at a natural period of around 2.7 seconds, the smallest ratio at around 3.8 seconds. Throughout the longer period part of the response spectra, the fault normal response is larger than the fault parallel.

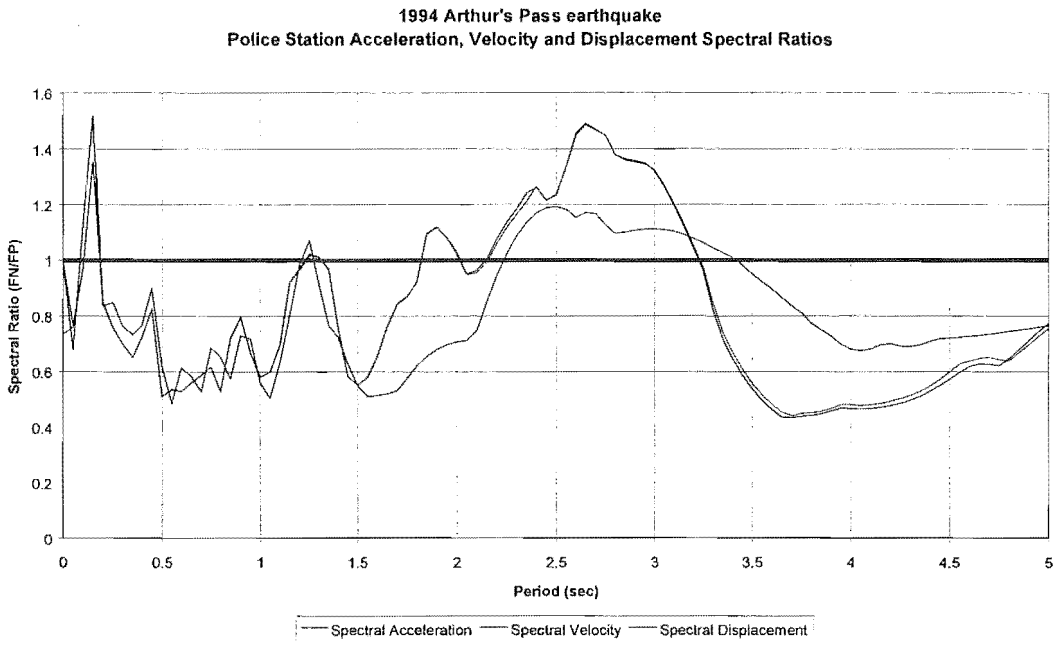

Figure 6-2 Arthur's Pass spectral ratios

The residual of the spectral accelerations, shown in Figure 6-3 clearly shows that the most significant differences in the two directions occur when the natural period is less than 2 seconds. While the graph of the ratio may suggest significant differences in the response at longer periods, these differences become largely irrelevant when the amplitude of the difference is considered. However, the ratio still shows significant, consistent differences in the two directions.

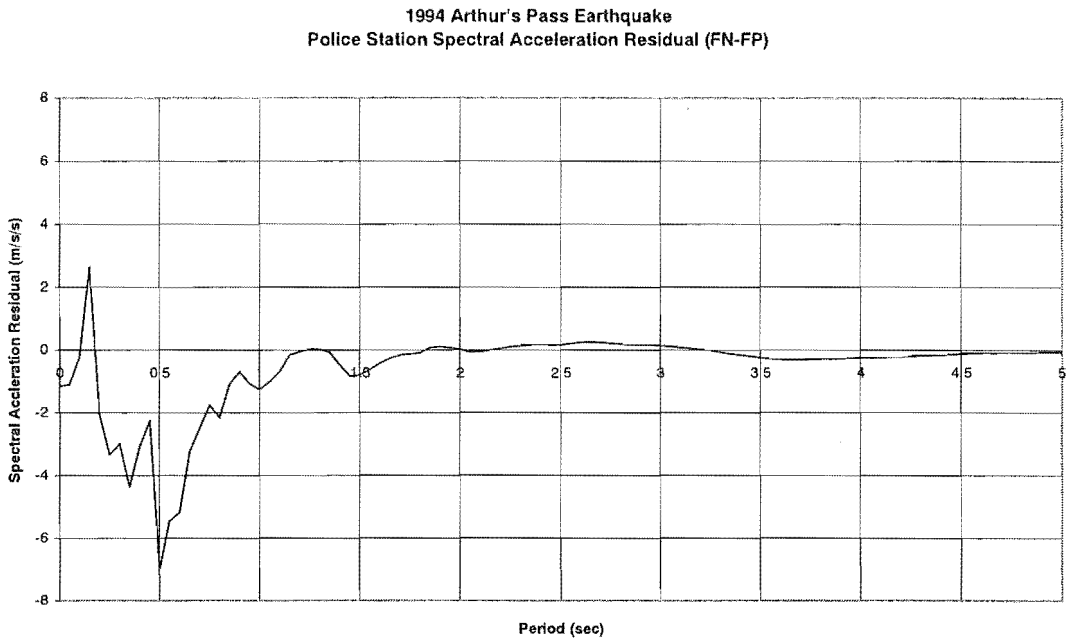

Figure 6-3 Arthur's Pass residuals of spectral acceleration

6.1.2 Spectral velocity

Differences at longer periods become more evident in the velocity response spectra shown in Figure 6-4. For more than 80% of the record the fault parallel response is larger than the fault normal. The fault normal amplification of response spectra by forward rupture directivity effects are not apparent at this site. The peak velocity, 10.6 m/s, is in the fault parallel direction and is 38% greater than the peak of 7.7 m/s in the fault normal direction. This is a substantial difference that could be significant in the design of structures in the area. The chart showing the ratio of the two values has been presented in Figure 6-2.

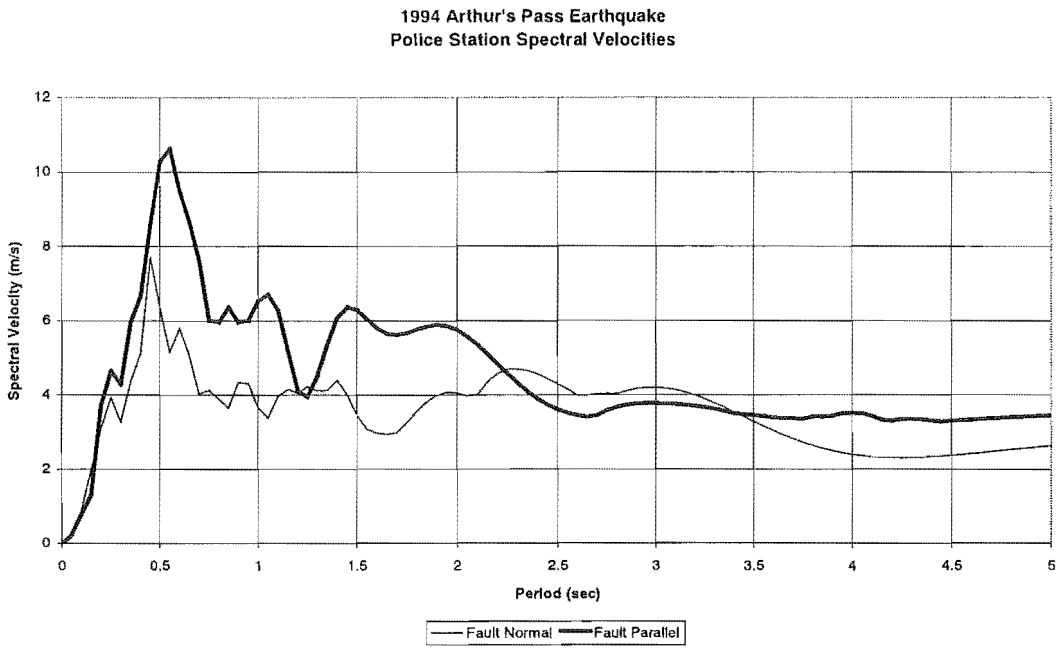

Figure 6-4 Arthur's Pass spectral velocity

6.1.3 Spectral displacement

Figure 6-5 shows the significant differences between the fault normal and fault parallel displacement responses at longer periods. The peak displacement response is 1.9m in the fault parallel direction, 46% larger than the peak displacement of 1.3m in the fault normal direction.

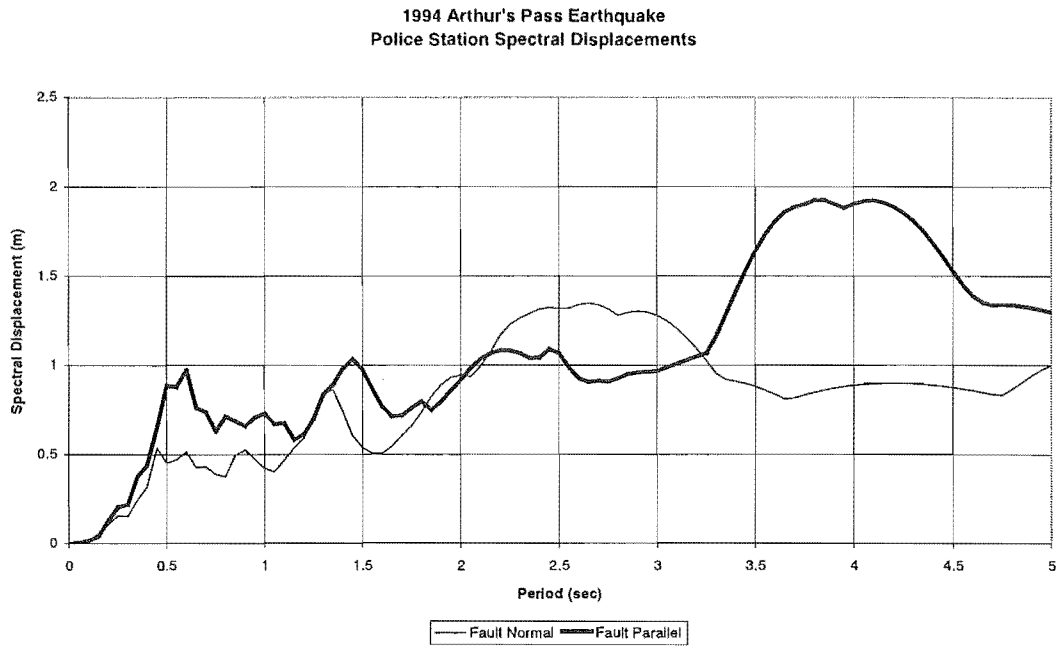

Figure 6-5 Arthur's Pass spectral displacements

6.2 Flock Hill

6.2.1 Spectral acceleration

Figure 6-6 shows that, except for the period range from 1.25 to 3.4 seconds, the fault normal response is greater than that of the fault parallel. Forward rupture directivity effects were expected to generate larger responses in the fault normal direction – this is consistent with what is observed here. The difference in response is significant at times, especially at periods just below 1 second. However, the peak spectral acceleration, 4.1 m/s/s in the fault normal direction is only marginally larger than the 3.8 m/s/s calculated in the fault parallel direction. The peak spectral acceleration was less than a third of that calculated from the Arthur's Pass record. The difference in the fault normal and fault parallel directions is subtle, but present, but is not as significant as that predicted by Somerville (1996).

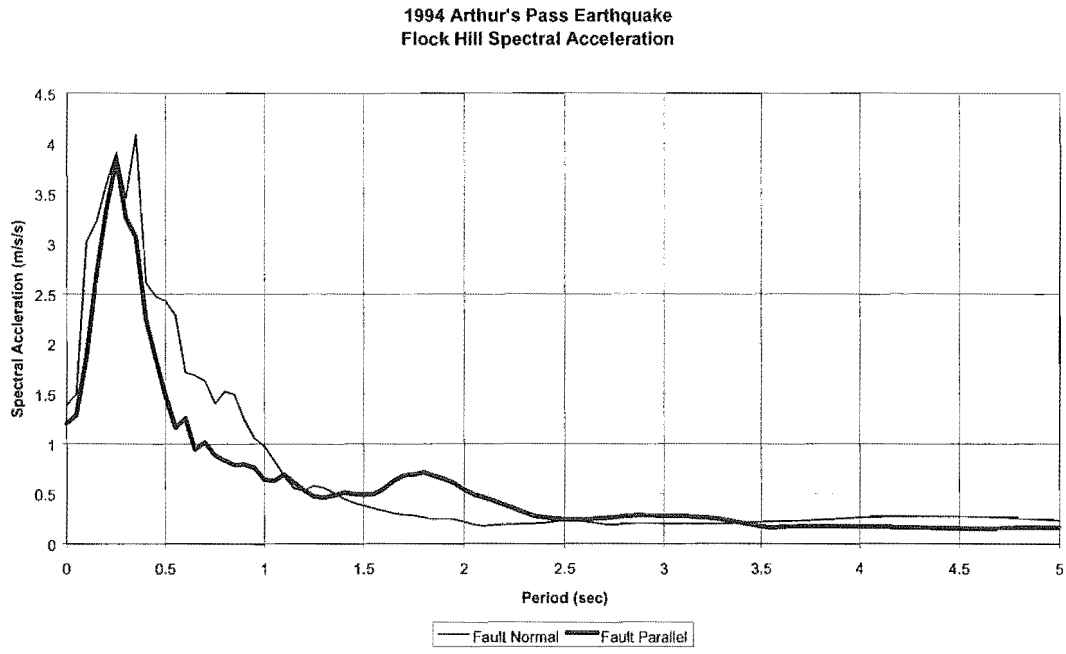

Figure 6-6 Flock Hill spectral acceleration

Slight differences in the fault normal and fault parallel directions are present in Figure 6-7, the ratio of the fault normal and fault parallel spectral acceleration response. 61% of values had a larger fault normal response. The difference in spectral acceleration is most significant at low periods, where the calculated response is large.

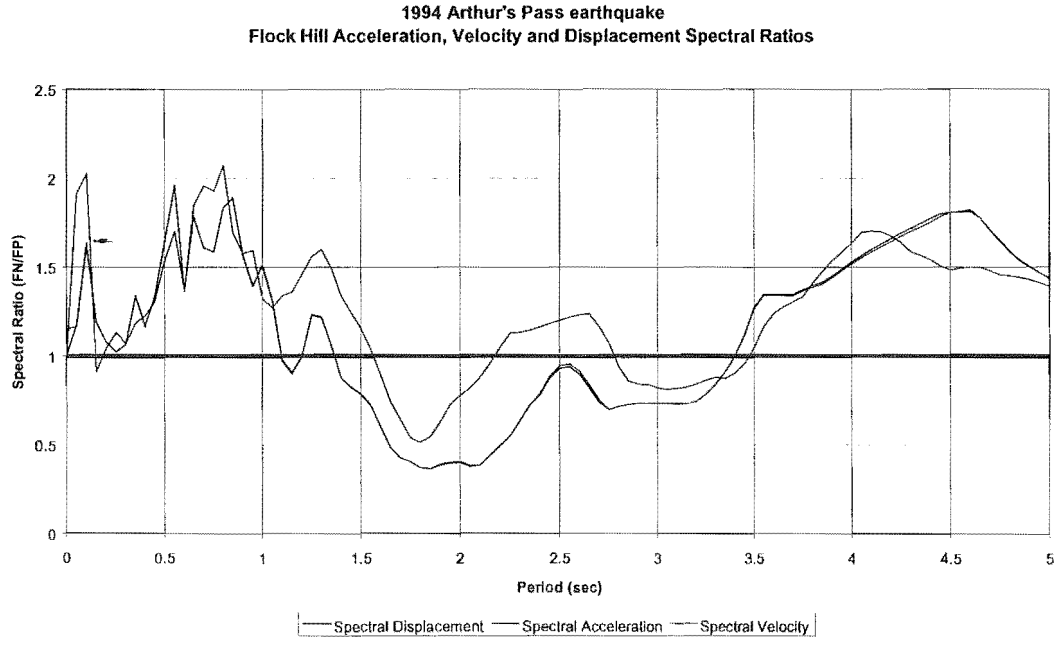

Figure 6-7 Flock Hill spectral ratios

6.2.2 Spectral velocity

Figure 6-8 shows the spectral velocity response from the Flock Hill station. Nearly 70% of the values are larger in the fault normal direction. The peak response, 2.4 m/s at a period of 1.8 seconds, is in the fault parallel direction. While the fault normal direction is is consistently larger, the peak velocity in the fault parallel direction is not consistent with forward rupture directivity effects. Forward rupture directivity effects should result in higher fault normal response. Thus, once again, there is conflicting information that makes the attempt to isolate directivity effects in this data difficult.

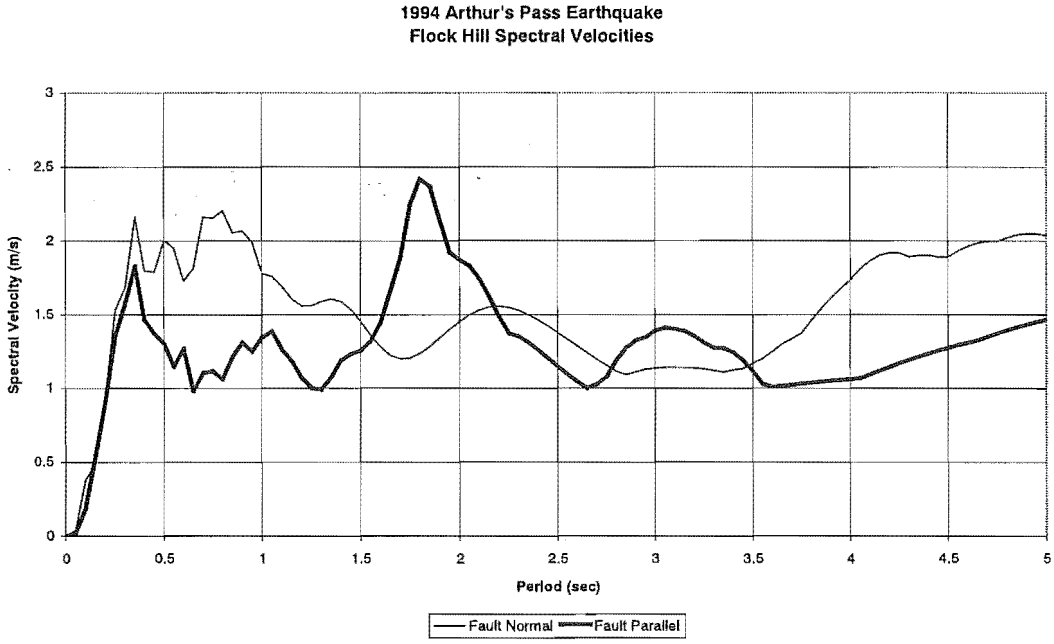

Figure 6-8 Flock Hill spectral velocities

6.2.3 Spectral displacement

Figure 6-9 shows that the peak spectral displacements in these records, 1.45m and 1.1m, are only slightly less than those recorded at the Arthur's Pass site, 1.3m and 1.9m. This is significant as the Flock Hill site is much further away from the fault than the Arthur's Pass Police Station, and experienced significantly lower accelerations, yet similar peak response displacements were generated. The

amplitude of the response at short periods is, however, significantly lower than that observed at the Arthur's Pass site. No ratio chart is presented, as it is effectively identical to Figure 6-7 Flock Hill spectral ratio.

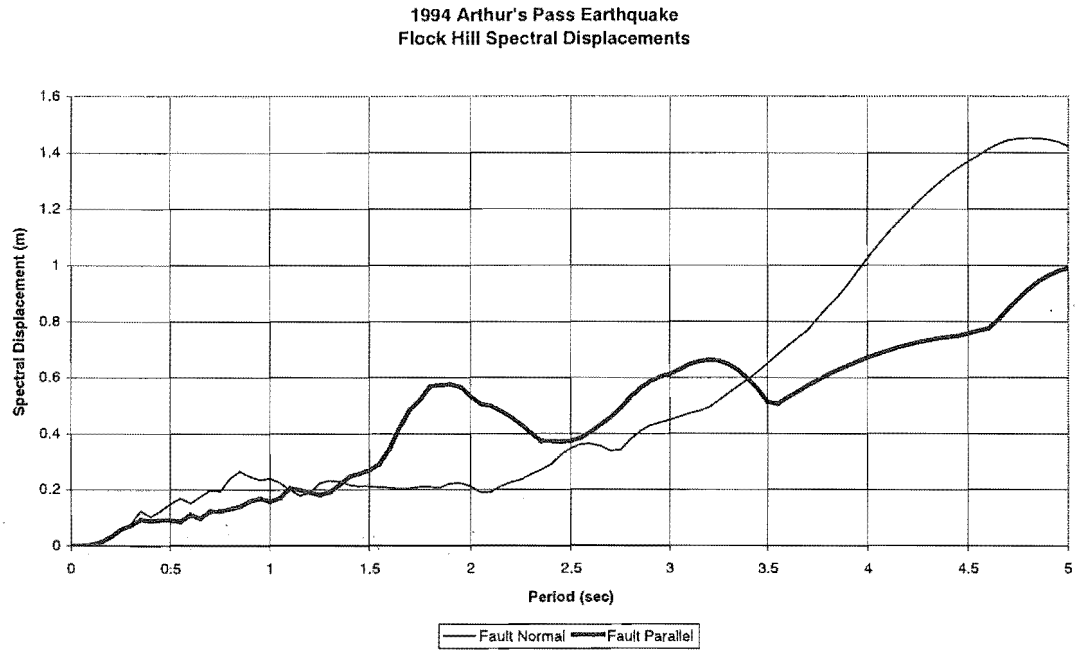

Figure 6-9 Flock Hill spectral displacement

6.3 Greymouth

6.3.1 Spectral acceleration

Figure 6-10, the calculated spectral acceleration, shows that the fault parallel direction exhibits consistently larger amplitude spectral accelerations than the fault normal. These are most probably related to site effects at Greymouth and will be discussed in Chapter 7. Peak spectral accelerations are just over 10% of those recorded at the Arthur's Pass site. This is less than expected from simple 1/r geometric spreading since the distance ratio is 11/57, compared with the 10% observed. The response at the site is low but there is significant anisotropy in shaking, possibly due to the site effects discussed in Chapter 7.

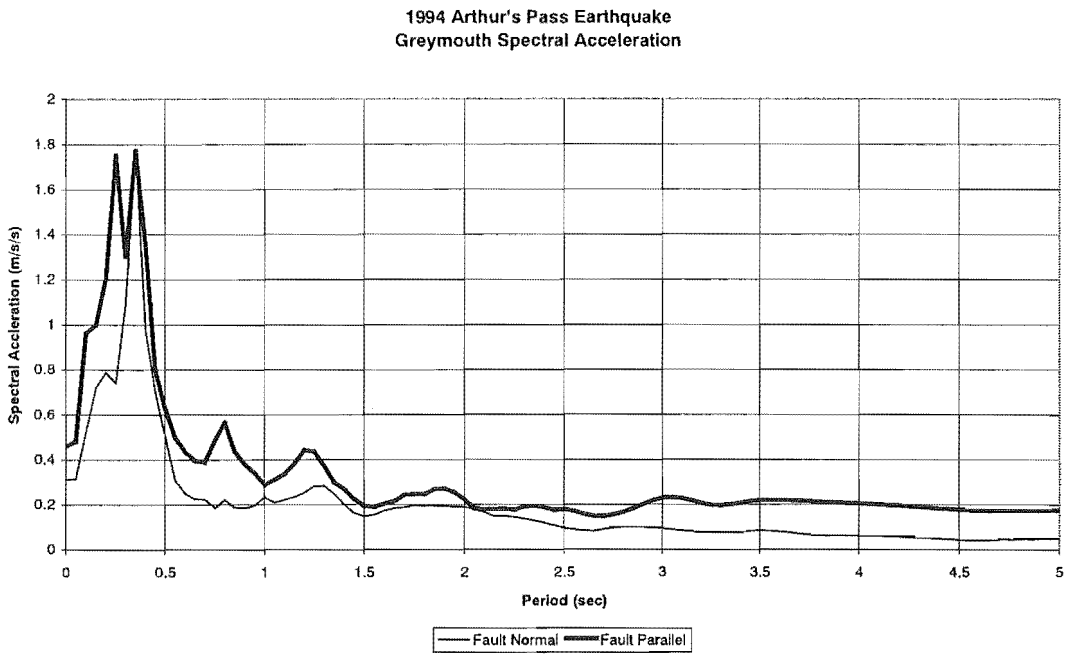

Figure 6-10 Greymouth spectral acceleration

The ratios presented in Figure 6-11 confirm the information in Figure 6-10, that the fault parallel direction exhibits significantly larger spectral acceleration amplitudes than the fault parallel. The difference in the two directions is so significant that the fault parallel response is greater than fault normal for the entire spectrum. Anisotropic shaking of this nature at such a distance from the epicentre is such that something other than fault geometry must be causing this unusual effect in the record. Site effects at Greymouth were thought to be the reason for this, but, as discussed later, this was not clearly identified.

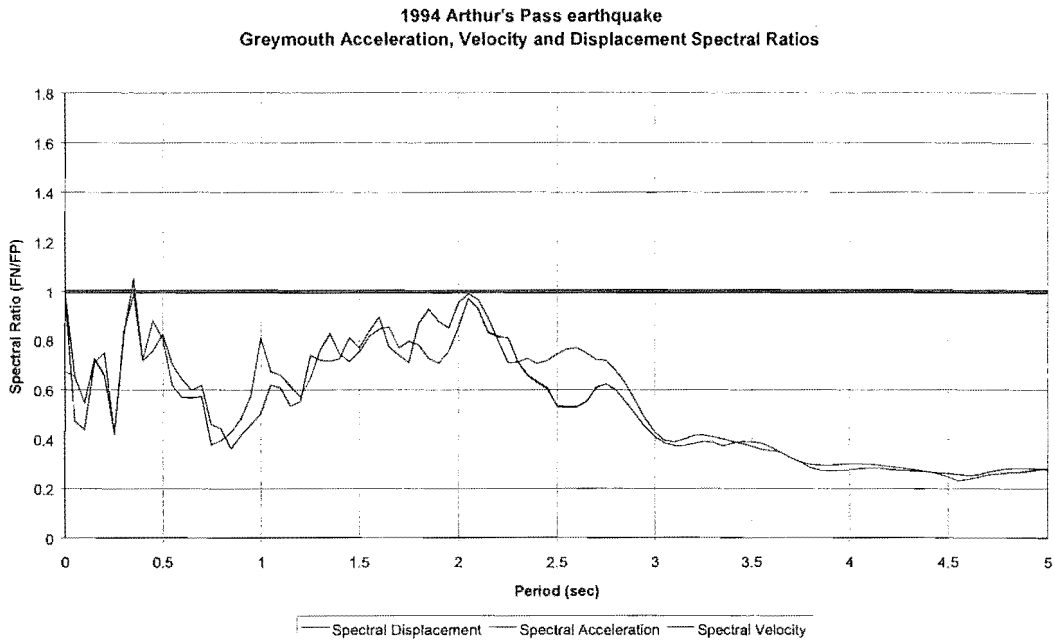

Figure 6-11 Greymouth spectral ratios

6.3.2 Spectral velocity

Figure 6-12 shows that again the fault parallel direction is significantly greater than the fault normal for effectively the entire record. This is expected as the ratio of the two components does not change significantly from the spectral acceleration chart. The difference in the two records again increases with increasing period to a peak at 6 seconds.

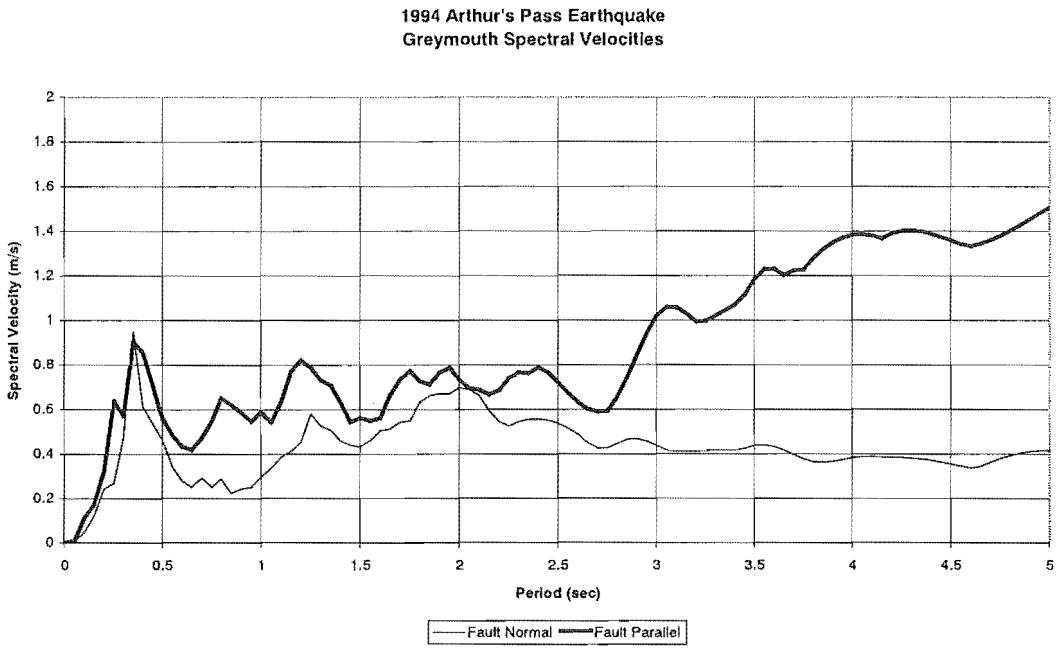

Figure 6-12 Greymouth spectral velocity

6.3.3 Spectral displacement

Spectral displacements for Greymouth are presented in Figure 6-13. The large fault parallel intensities at this site that were noted in sections 6.3.1 and 6.3.2 continues here. The difference increases with increasing period to a peak at 6 seconds

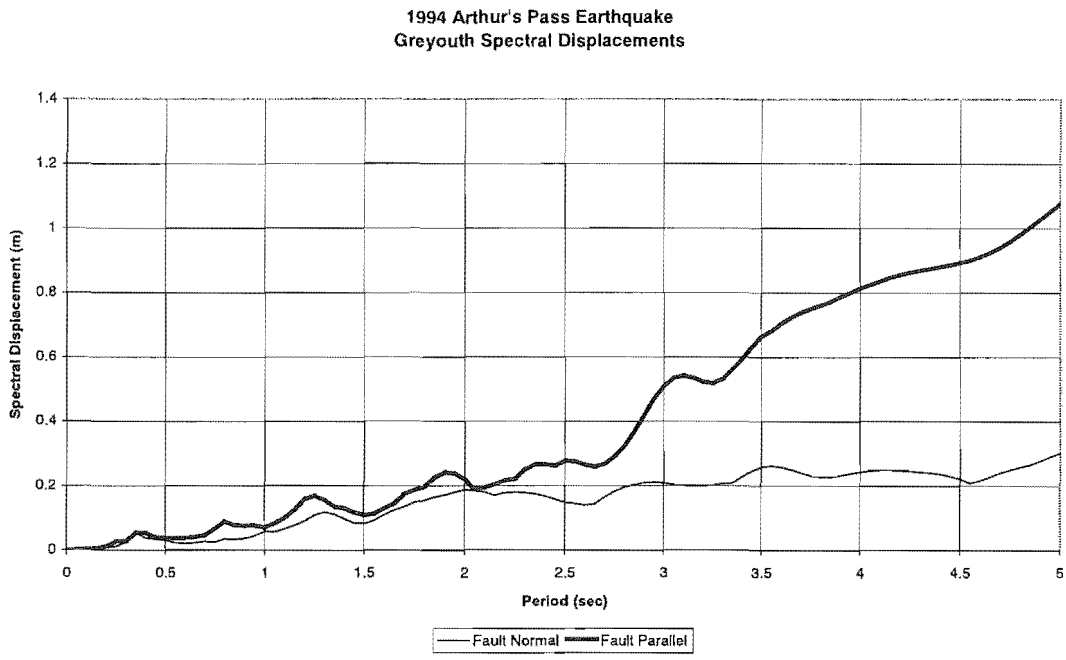

Figure 6-13 Greymouth spectral displacement

This difference in the Greymouth record is significant. The two directions are showing significantly different behaviour. The site effects are investigated in Chapter 7, but fail to show conclusively that there is resonance perpendicular to the shoreline. The reason for the significant differences cannot therefore easily be attributed to any one particular source.

7 Greymouth site effects

Clear, significant differences exist between the fault normal and fault parallel components of Greymouth's acceleration, velocity and displacement ground motions shown in Chapter 4. There are also significant differences in both the Fourier and response spectra. These differences have been presented in Chapters 5 and 6. The differences were initially thought to be due to site effects, and this chapter examines this proposition in more detail.

The Greymouth site is located on a wedge of sediment at the mouth of the Grey river, between the hills and the sea. On two opposing sides, north and south, the site is effectively open to the transmission of seismic energy. The other two sides, west and east, are bounded by the sea on one side and the mountains opposite. The direction that strikes parallel to the shoreline is henceforth referred to as the shore parallel direction; the direction perpendicular to the shore is referred to as the shore normal direction. Acceleration, velocity and displacement records are transformed to shore normal and shore parallel components, as described in Section 7.1, and analysed for anisotropic behaviour.

Seismic energy can be trapped in surficial soft layers (Lay and Wallace, 1995; Kramer, 1996). Once energy is trapped in the soft material at this site, it is constrained by the width of the thin strip in the shore normal direction, but is free to propagate in the shore parallel direction. This could result in significant shore normal resonance at the site as energy is constrained in the shore normal direction. The ground motion is analysed in the two directions (shore normal and shore parallel) in an attempt to evaluate the significance of this possible shore normal amplification.

Once again, the low amplitude of the acceleration records at the Greymouth site is highlighted. The amplitude of the ground motion records is low, and so may more easily be influenced by site effects.

7.1 Greymouth

The instrument orientations and equations used for the transformation to shore normal and shore parallel components from the principal instrument directions are presented below, in Tables 7-1 and 7-2. The shore normal and shore parallel directions are presented graphically in Figure 7-1.

	Recording directions	
Original instrument orientation	N00E = Principal orientation A	N90W = Principal orientation B
Shore normal/shore parallel	N15.5E = Shore Normal	N74.5W = Shore Parallel

Table 7-1 Directions considered at Greymouth

Site	**Principal Direction**		**Transformation Equations**	
	A	**B**	**Shore Normal**	**Shore Parallel**
Greymouth	N00E	N90W	ASin15.5 + BCos15.5	ACos15.5 – Bsin15.5

Table 7-2 Transformation to shore normal and shore parallel components

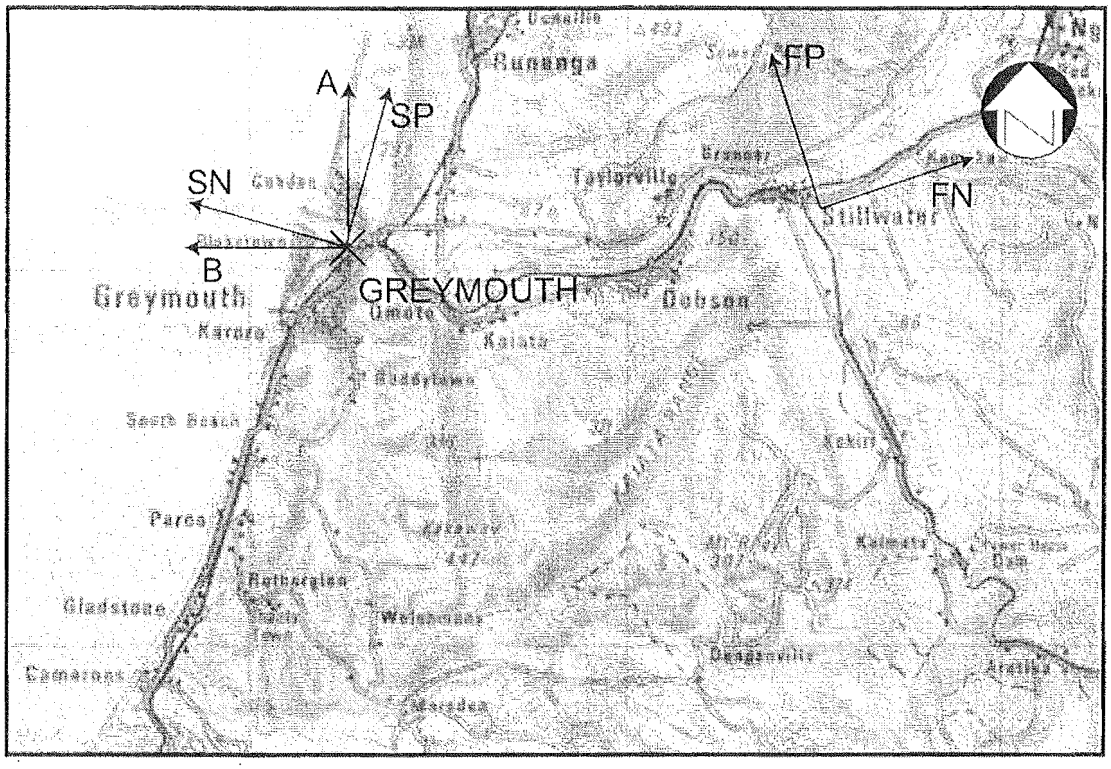

Figure 7-1 Greymouth site with shore normal and shore parallel orientations shown, as well as the principal instrument orientations (A and B)

7.1.1 Acceleration record

Figures 7-2 and 7-3 show that the shore normal component contains larger amplitude accelerations than the shore parallel. This difference is highlighted by the root-mean-square (RMS) accelerations of the two records. The shore normal RMS acceleration was 80 mm/s/s, significantly greater than the 71 mm/s/s exhibited by the shore parallel direction. As well as this, inspection of the two records suggests that the strong motion in the shore normal direction is both shorter and more intense than the shore parallel. This observation is supported by the durations presented in Table 7-3.

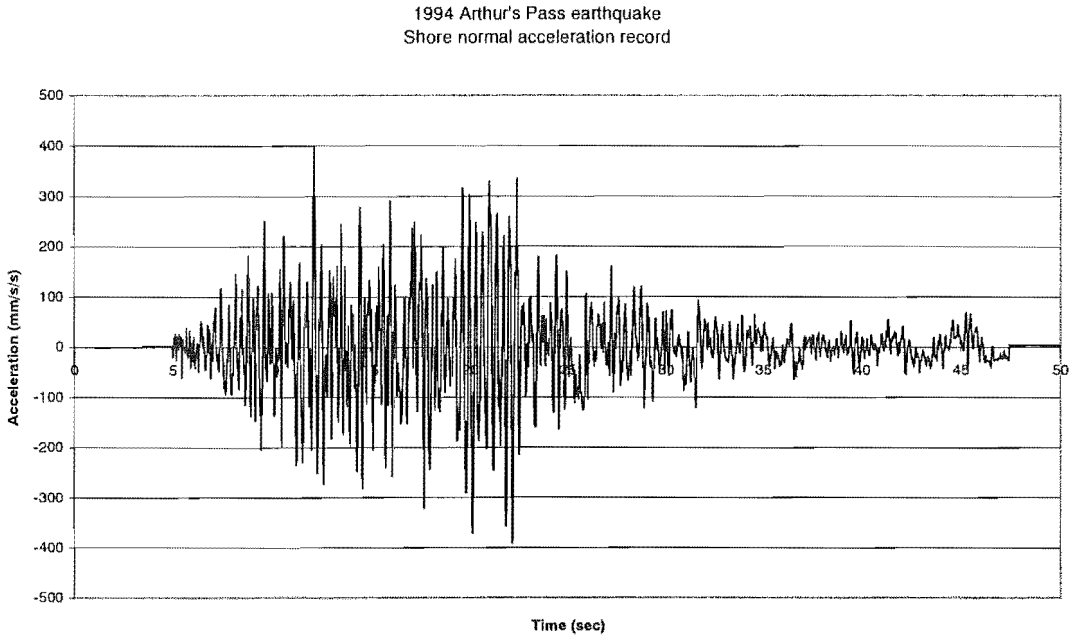

Figure 7-2 Greymouth shore normal acceleration record

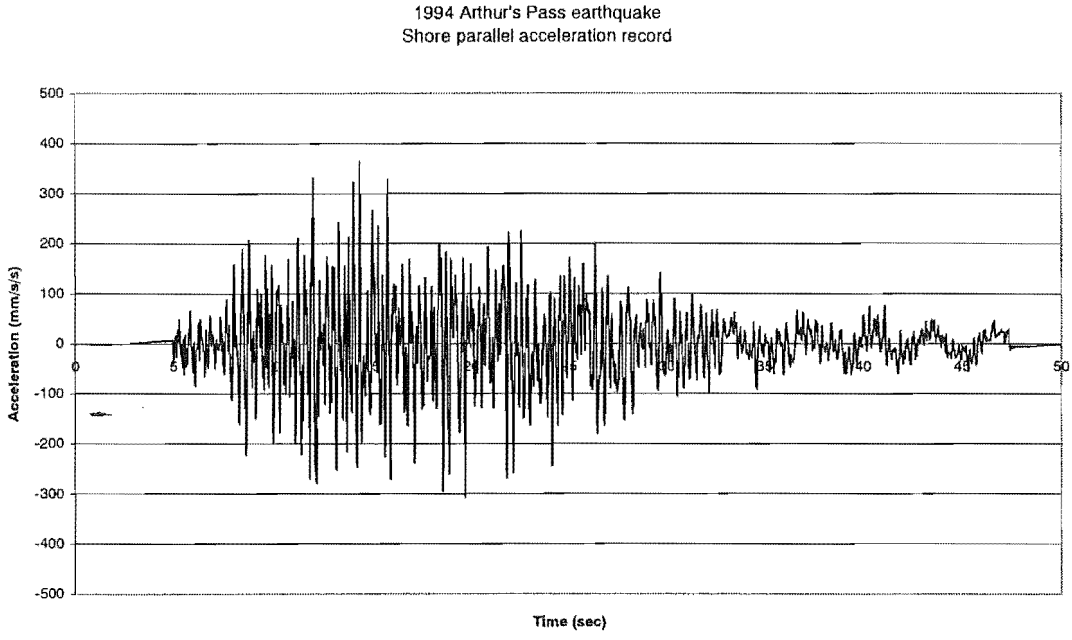

Figure 7-3 Greymouth shore parallel acceleration record

Table 7-3 shows that the shore normal duration is less than that of the shore parallel. Larger accelerations were observed in the shore normal component of the acceleration record. This suggests that the shore normal direction exhibited more intense shaking

than the shore parallel. The durations support the proposition that there is interference in the shore normal direction. The durations of both the shore normal and shore parallel directions differ more from the total than the fault normal and fault parallel.

Direction:	SN	SP	FN	FP	Total
Duration	19.26	22.76	21.10	21.80	21.10

Table 7-3 Greymouth strong motion durations

The differences between the shore normal and shore parallel acceleration amplitudes are presented in Figure 7-4. The shore normal acceleration amplitudes are consistently larger than the shore parallel. This result is consistent with the observations made concerning the acceleration and duration results. These amplitudes are compared to the fault normal and fault parallel sorted acceleration amplitudes to compare relative amplitude.

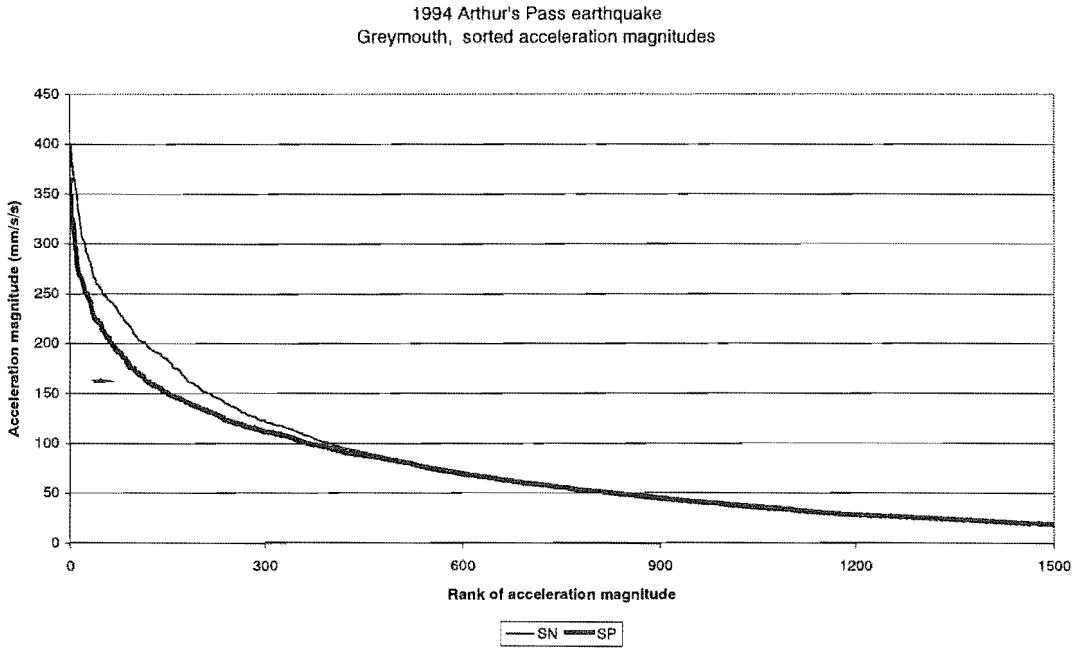

Figure 7-4 Greymouth sorted acceleration amplitudes

Figure 7-5 shows the shore normal and shore parallel acceleration amplitudes compared with the fault normal and fault parallel acceleration amplitudes. The largest accelerations recorded were in the fault normal direction. The two sets of axes being

compared (shore and fault normal and parallel) are distinct as they are oriented at approximately 45 degrees to each other. This is inconsistent with what was expected, as the shore normal direction was expected to exhibit a greater peak acceleration than the fault normal direction. This peak acceleration in the fault normal rather than the shore normal direction could either represent the random nature of the ground motion, or be an indication of flaws in the assessment of site effects.

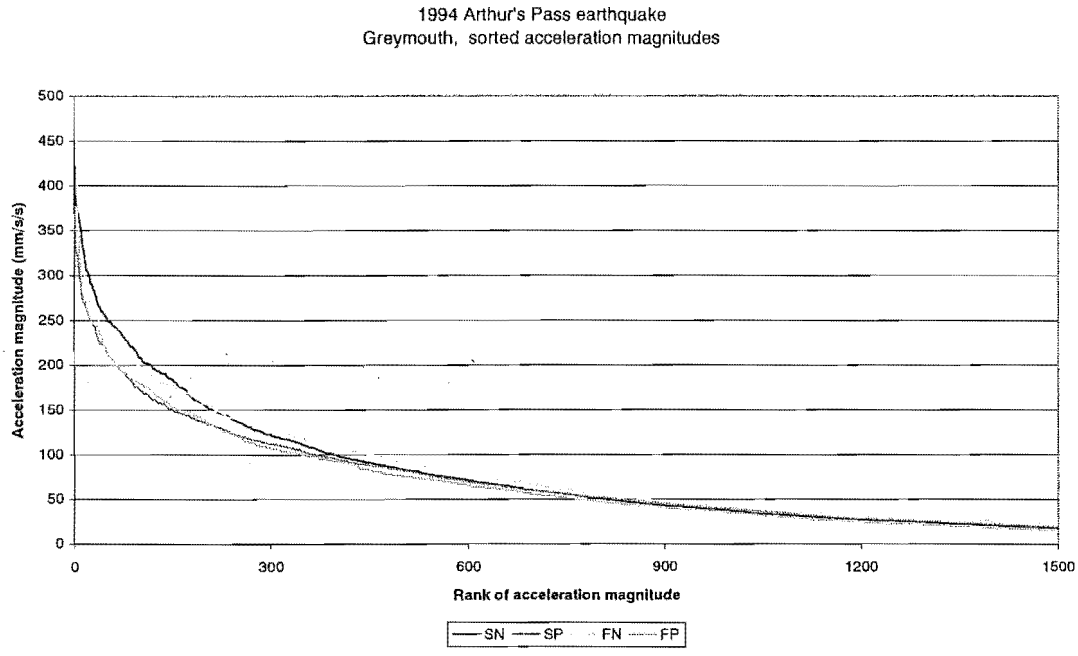

Figure 7-5 Greymouth sorted acceleration amplitudes

7.1.2 Velocity record

Figure 7-6 exhibits consistently higher velocities in the shore parallel direction. This is shown in the sorted accelerations, Figure 7-7, and is inconsistent with the results from section 7-4, where shore normal accelerations were significantly larger than shore parallel. While peak accelerations were larger in the shore normal direction, peak velocities are larger in the shore parallel. This response is inconsistent with the expected effects of site geometry. The Flock Hill site exhibited a similar trend of larger peak accelerations in one direction, and larger velocities in the other.

At the tail end of the record, between 40 and 50 seconds, some noticeably coherent velocity waveforms begin to appear. These waveforms are larger than the velocities in the 10 seconds leading up to this coherent part of the record. This coherency is investigated in section 7.1.3.

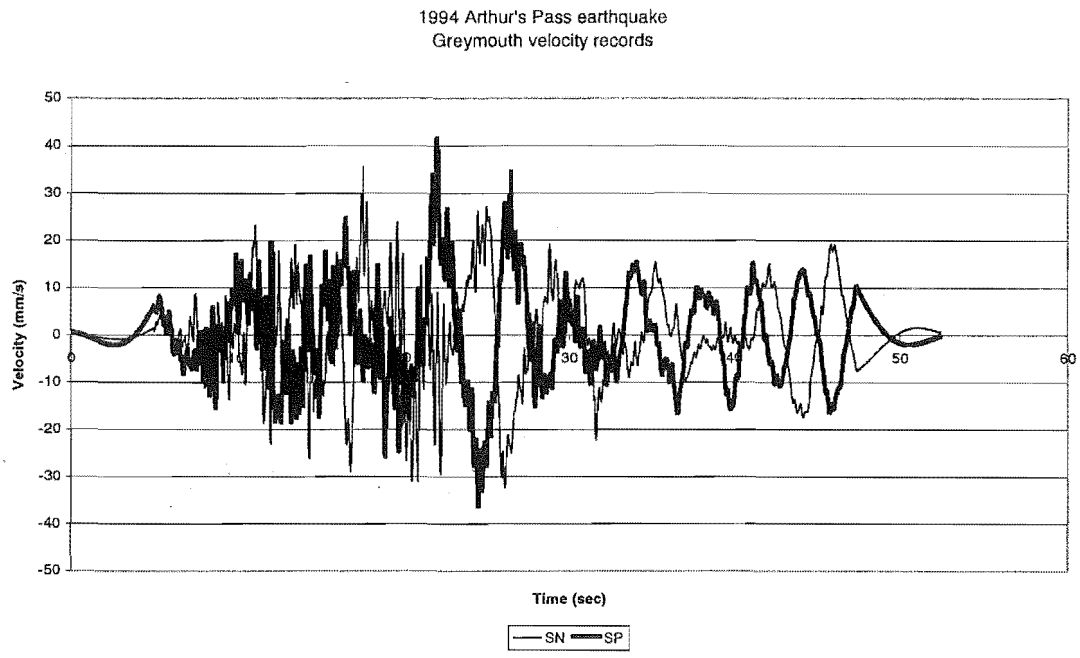

Figure 7-6 Greymouth velocity records

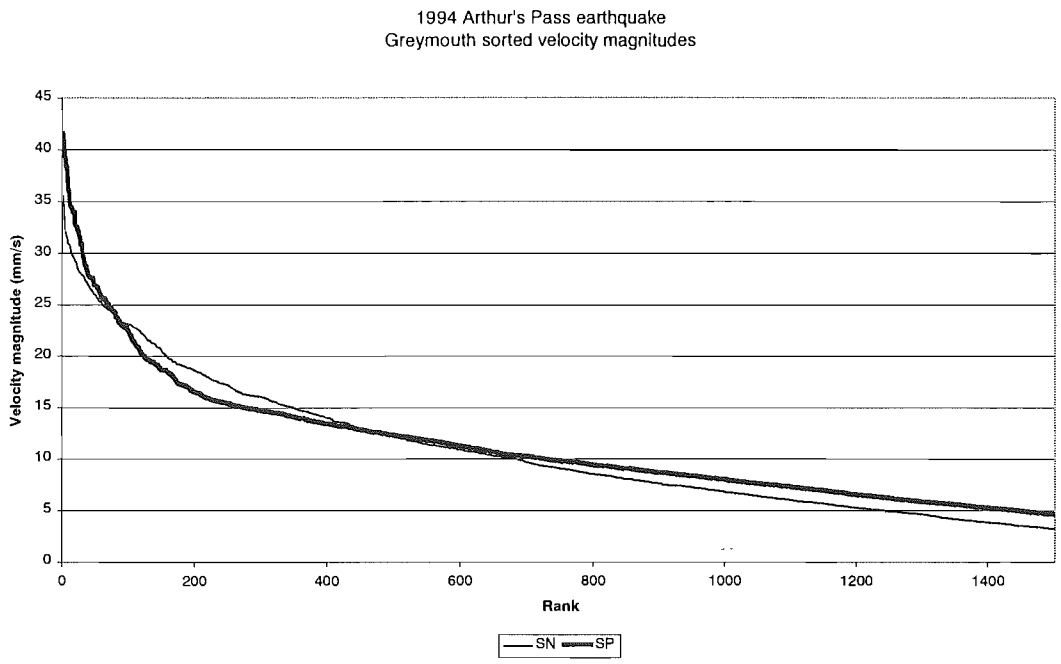

Figure 7-7 Greymouth sorted velocity records

7.1.3 Displacement record

Figure 7-8 shows the two components of ground motion in the shore normal and shore parallel direction. The two records appear to be largely the same, with both moving into what appears to be free vibration after the cessation of strong ground motion. The shore parallel record, in particular, shows this apparent harmonic motion clearly between 30 and 50 seconds. An approximate natural period of vibration of the surficial soil layers is estimated from this motion by fitting a harmonic curve to this part of the record in Figure 7-9. Another point of interest observed on the graph is the presence, in the shore normal direction, of an increase in displacement amplitude at a time of 46 seconds. This is associated with the same shape on the velocity chart, at the same time, that was observed in Figure 7-6. This increase is inconsistent with the presence of free, simple harmonic motion.

A simple sine wave fitted to shore parallel displacement data between 33 and 50 seconds yields a natural period of 3.15 seconds. The fitted sine wave is presented in Figure 7-9. Cousins (1996) states that the Greymouth instrument was situated on

loose to compact sandy gravel, up to 40m deep, and this estimate is used to assess the quality of the estimated fundamental period under assumed vertically incident shear waves. Kramer (1996) demonstrates that resonant frequencies of soil deposits with vertically incident shear waves are represented by Equation 7-1.

$$\omega_n \approx \frac{v_s}{H}\left(\frac{\pi}{2} + n\pi\right)$$ Equation 7-1 (From Kramer, 1996)

where n=0, 1, 2, ...,

ω_n = natural frequency of vibration being considered,

v_s = shear wave velocity,

H = thickness of material

The fundamental frequency is therefore presented in Equation 7-2, and the characteristic site period in Equation 7-3.

$$\omega_0 = \frac{\pi v_s}{2H}$$ Equation 7-2 (From Kramer, 1996)

$$T_s = \frac{2\pi}{\omega_0} = \frac{4H}{v_s}$$ Equation 7-3 (From Kramer, 1996)

Equation 7-4 (The application of Equation 7-3) demonstrates that, assuming a characteristic site period of 3.15 seconds (from the curve fitting exercise), and a depth of 40m, a shear wave velocity of 50.8m/s is required. This implies quite a soft material.

$$v_s = \frac{4H}{T_s} = \frac{4*40}{3.15} = 50.8\,m/s$$ Equation 7-4

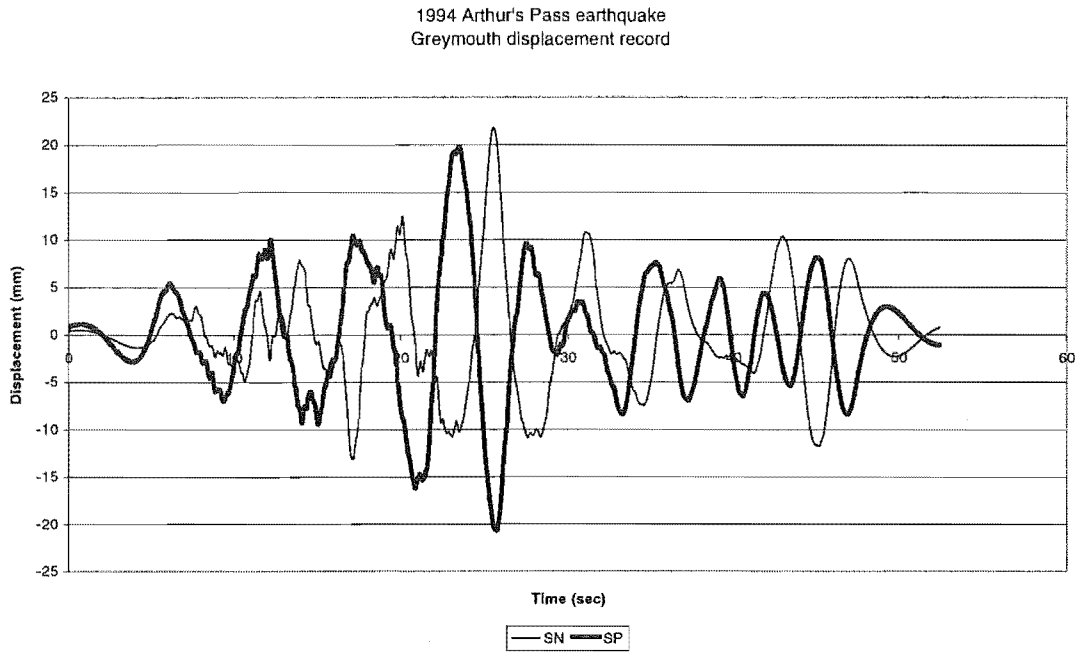

Figure 7-8 Greymouth displacement records

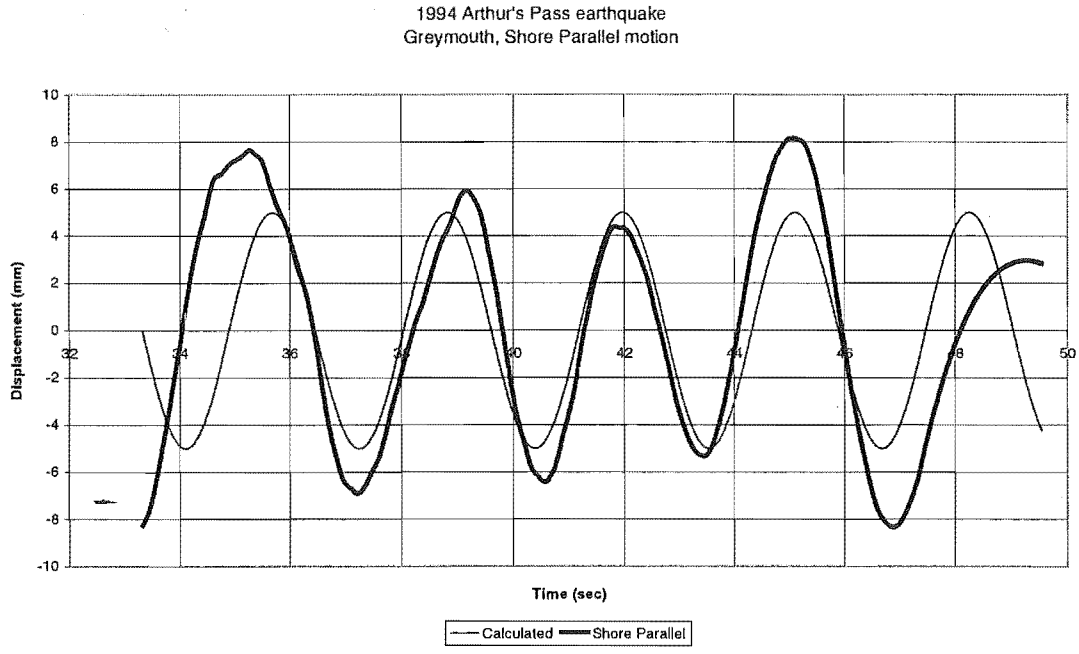

Figure 7-9 Greymouth shore parallel displacements with fitted sine curve

7.1.4 Spectral acceleration

Figure 7-10 shows the difference in spectral acceleration response in the two components. The peak shore normal response, 2.4 m/s^2 is nearly twice the shore

parallel peak of 1.3 m/s^2. These peak responses are located around a natural period of 0.35 seconds. The peak response was nearly 5 times greater than the recorded peak ground acceleration of 0.5 m/s^2. In 47% of periods considered, the shore normal spectral acceleration was greater than the shore parallel. The amplitude of the responses in the two directions is significantly different, however, with the shore normal clearly exhibiting a much larger response. This is consistent with the larger recorded accelerations in the shore normal direction. No noticeable peak was detected at a natural period of 3.15 seconds, the possible resonant frequency of the soft material at the site.

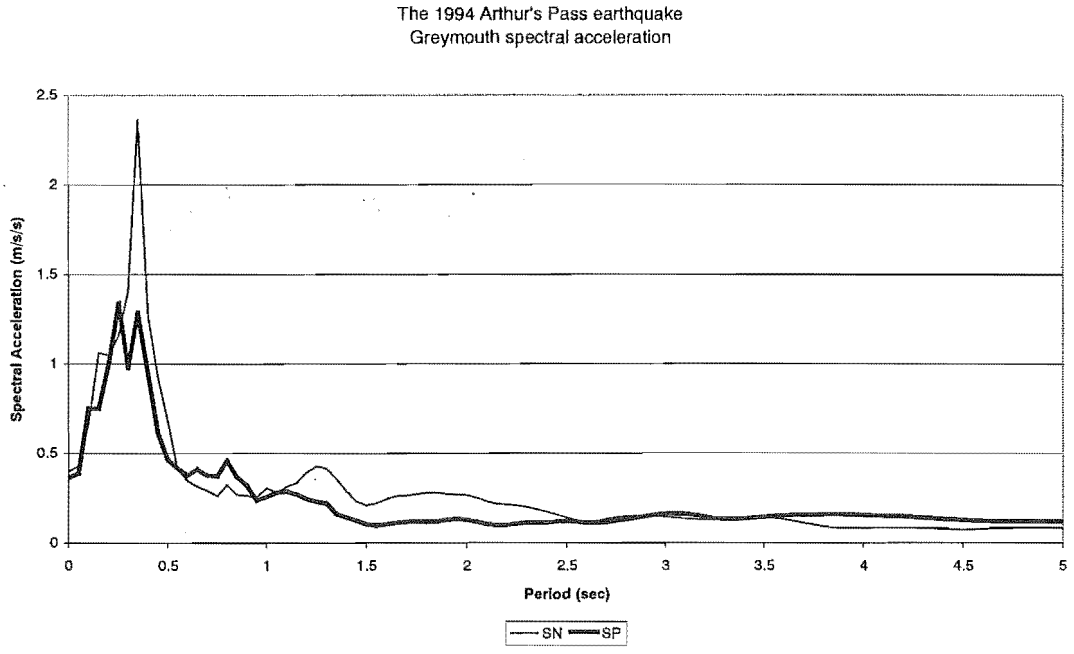

Figure 7-10 Greymouth spectral accelerations

7.1.5 Spectral velocity

The shore normal direction had a significantly larger peak response and larger amplitude accelerations. The same difference is not apparent in the velocity response chart, Figure 7-11. The shore normal direction exhibits significantly stronger motions over the period range 1.5 to 3.5 seconds, while the shore parallel response is stronger from 3.5 seconds to very long period motions. There is still a very large peak in the

shore normal direction at a period of 0.35 seconds, the same peak that was present in the spectral acceleration chart. Other response spectra do not show the same transmission of spikes from acceleration response to velocity response.

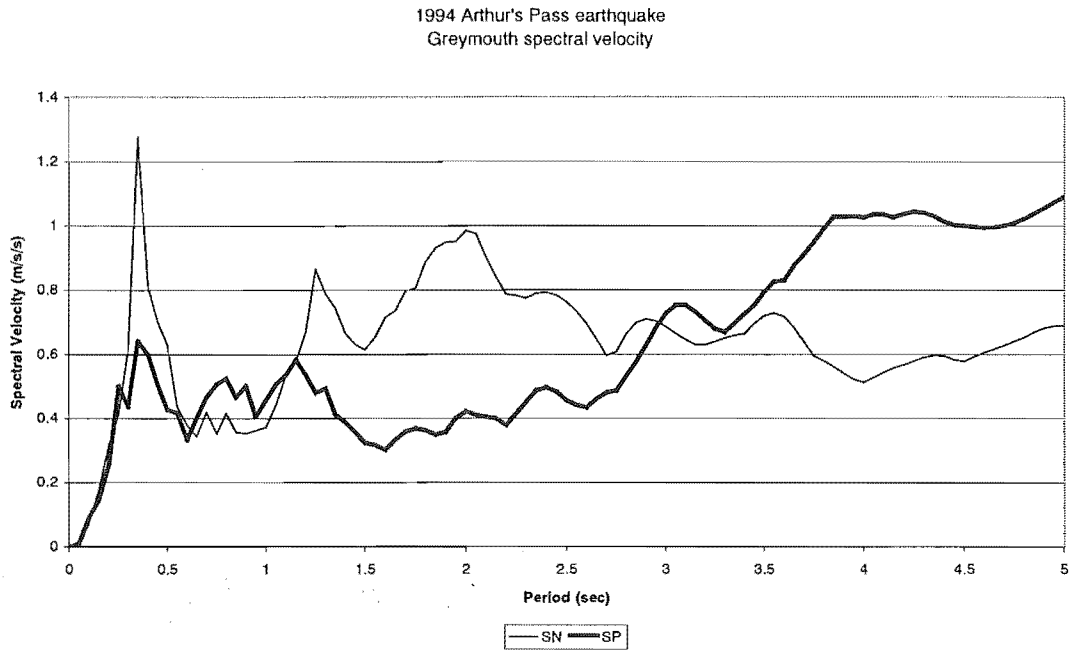

Figure 7-11 Greymouth spectral velocities

7.1.6 Spectral displacement

Figure 7-12 shows the spectral displacements calculated for Greymouth. The noticeable peak that was present in both the spectral acceleration and velocity charts is not present. The peak displacement response, 0.92m, occurs at a period of 6 seconds. There is a localised maximum in the shore normal direction at a period of 3.15 seconds, the same period that was estimated for the site's natural period. This could be evidence of resonance in the soil layers, but the peak does not appear in either the acceleration or velocity spectra.

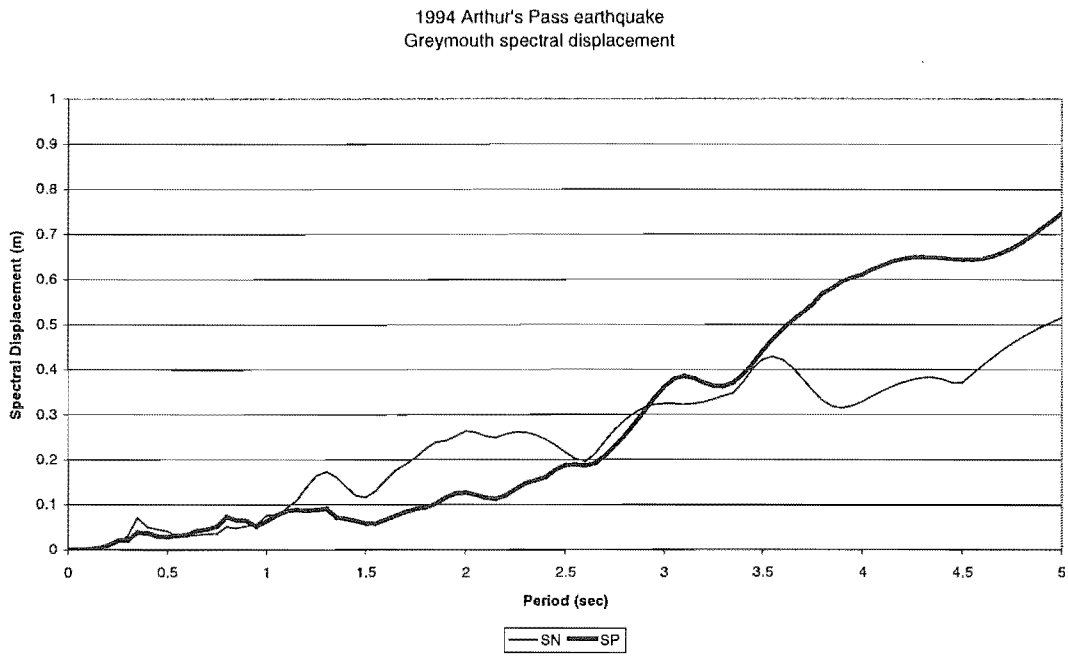

Figure 7-12 Greymouth spectral displacement

7.1.7 Comparison with Flock Hill

There are some comparisons that can be made between the Greymouth and Flock Hill sites. At these sites, the acceleration and velocity records, as well as spectral acceleration and velocity records, had peaks in different directions. This was not expected. The Flock Hill site was expected to show evidence of forward rupture directivity effects in the fault normal direction if the rupture occurred on the assumed fault plane. The Flock Hill larger peak velocity in the fault parallel direction is not usually associated with forward rupture directivity effects at the site. Ground motion records from Greymouth showed atypical, anisotropic response to an assumed isotropic input seismic energy. This was initially thought to be due to resonance in the shore normal direction, but the large peak velocity in the shore parallel direction causes problems in accepting this proposition.

7.2 Conclusions

The anisotropy noted at the site during the analysis of the fault normal and fault parallel components of the ground motion may have been explained by the site

geometry. Some observations at the site agreed with this. The significant differences in the peaks of the acceleration response spectra were an indicator that something significant may be affecting recorded ground motion the site. While the shore normal direction exhibited larger acceleration amplitudes than the shore parallel, these were not as large as the fault normal acceleration amplitudes (see Figure 7-5). In addition to this, the shore parallel direction exhibited larger peak velocities and similar displacements. These results are not consistent with resonance in the shore normal direction. The durations, shown in Table 7-3, are consistent with the expected results of shore normal resonance.

8 Rupture model

8.1 Modified shear wave version of the Haskell far field Fourier model

A modified version of the Haskell fault rupture model (Kasahara, 1981, Lay and Wallace, 1995) is used in the prediction of far field Fourier amplitudes at sites around the assumed fault plane. The model development is described in both texts, but is summarised here. The Haskell model (characterised by a ramp representing dislocation history) is modified by conversion to Fourier amplitudes of acceleration, rather than displacement. Only the shear wave version of the model is considered, for the reason given in section 8.1.1

The displacements due to a time varying force double couple in an homogenous elastic medium have been well documented (eg Kasahara, 1981; Lay and Wallace, 1995), hence the model development begins with these results. A force double couple, with magnitude M_0, is applied at the origin, and oriented along the X_1 and X_2 axes. These axes are shown in Figure 8-1.

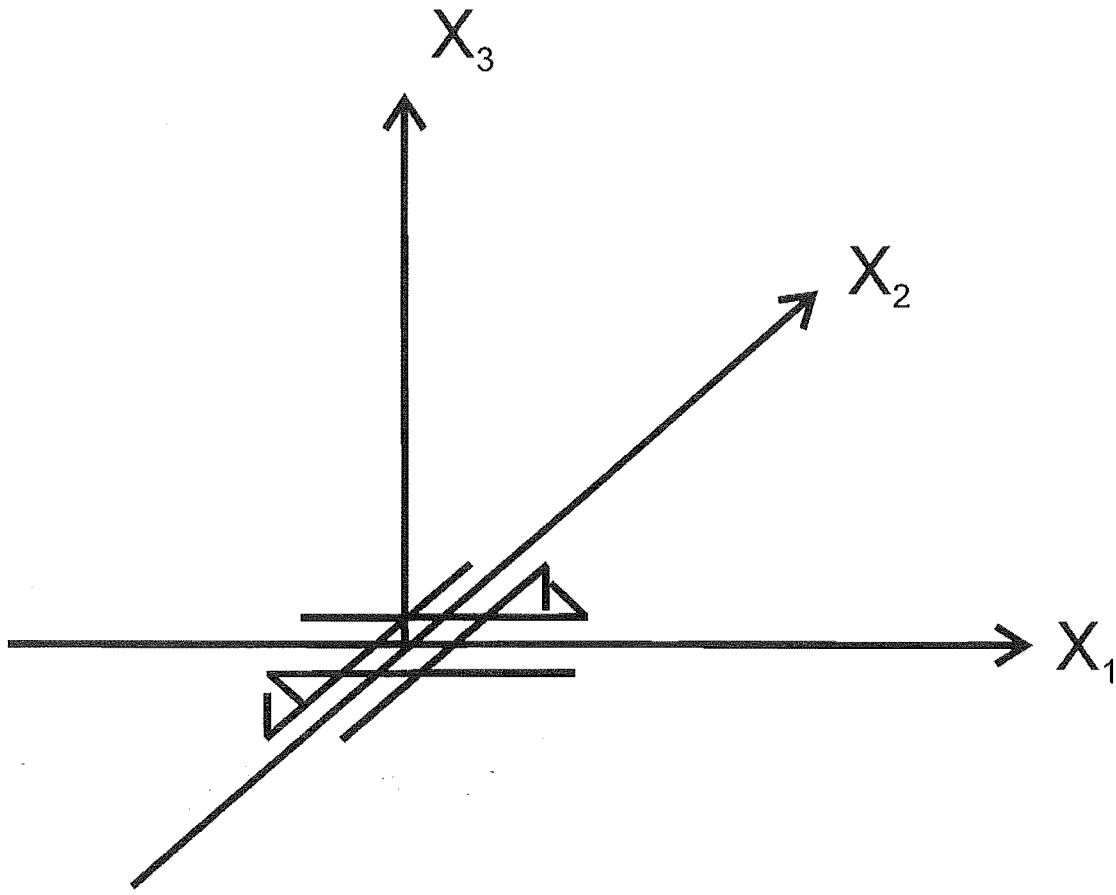

Figure 8-1 Stationary force double couple on X_1-X_2 plane

The far field displacements in the r, θ and ϕ directions are shown in Equations 8-1 to 8-3. Near field displacements have a series of additional terms that decay at rates of r^2 or greater, which are therefore ignored in this model which represents the gross properties of the earthquake rupture process. In the following sections, r is the distance from the origin, θ is the angle made in the X_1-X_2 plane, and ϕ is the angle made with the X_3 axis.

$$U_r(t) = \frac{\dot{M}(t - \frac{r}{C_p})}{4\pi\rho C_p^{\,3} r} Sin(2\theta)Sin(\phi) \qquad \text{Equation 8-1}$$

$$U_\phi(t) = \frac{\dot{M}(t - \frac{r}{C_s})}{4\pi\rho C_s^{\,3} r} Cos(\theta)Sin(\phi) \qquad \text{Equation 8-2}$$

$$U_\theta(t) = \frac{\dot{M}(t - \frac{r}{C_s})}{4\pi\rho Cs^3 r} Cos(2\theta) Sin(\phi)$$ Equation 8-3

The term in each displacement component, $\dot{M}(t - \frac{r}{C_s})$ represents the variation of the force with time. The lag between the force being applied, and a site experiencing it, is the $\frac{r}{C_s}$ function in the moment representation. The moment-time function can be roughly approximated as a linear ramp, as illustrated in Figure 8-2. Models that use ramps to represent dislocation histories are known as Haskell rupture models (Kasahara, 1981; Lay and Wallace, 1995). An example of the ramp used in the model is shown in Figure 8-2 below. Note that the differential of the displacement becomes a boxcar with a length equal to the rise time, t_r.

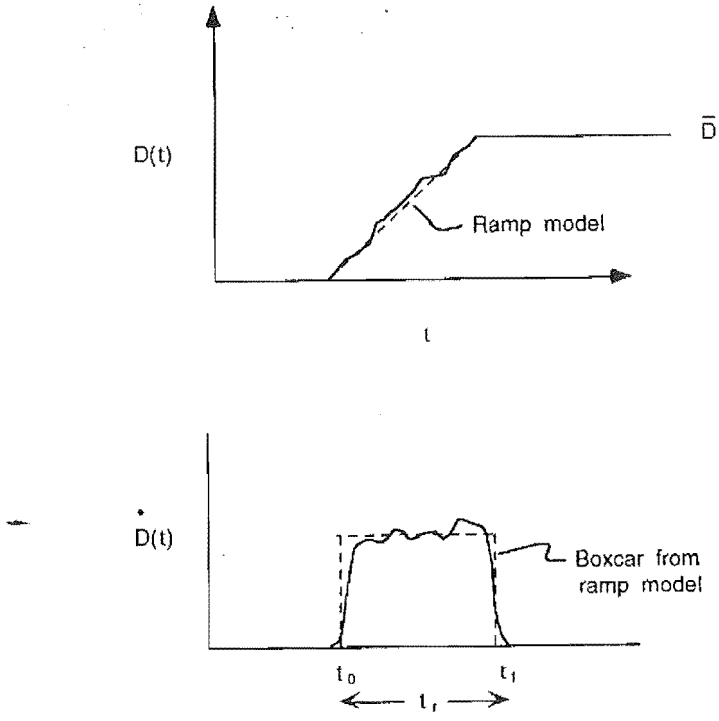

Figure 8-2 Ramp model used in model

Source: Lay and Wallace, 1995

$\overline{D}$ = average displacement

D(t) = displacement variation with time

t = time

As well as the nature of the displacement due to the application of the moments, there are directivity effects that must be considered around the fault plane. These, as discussed in Chapter 1, become significant when the speed of rupture propagation and shear wave are similar. The effects of directivity are represented by another boxcar, the length of which is the perceived duration of the earthquake. The perceived duration depends on the relative geometry of the source and site, and can be summarised by Equation 8-4, the apparent rupture duration. Note that the perceived time varies most significantly when the rupture propagation velocity, V and the shear wave speed, C_s, are similar.

$$t_c = \frac{L}{V}(1 - \frac{V}{C_s}\cos(\theta)) \qquad \text{Equation 8-4}$$

(Based on Lay and Wallace, 1995 and Kasahara, 1981)

Where:

t_c	=	Perceived rupture duration
L	=	Rupture length
V	=	Rupture propagation speed
C_s	=	Shear wave speed
θ	=	Angle between site and direction of rupture propagation

The source time functions shown previously (Equations 8-1 to 8-3) can represent the effect of fault movement as well as the nature of the slip occurring along the fault. The effect of fault movement is considered as a boxcar, very similar to that described for the slip time history function. The source time dislocation function can then be written as Equation 8-5.

$$u(t) = \frac{M_o(B(t;t_r) * B(t;t_c))}{4\pi\rho C_s^{\,3} r} \qquad \text{Equation 8-5}$$

where the boxcar of width t_r represents the dislocation history (ramp model) and the boxcar of width t_c represents the directional effects around the fault. The $*$ represents the convolution that occurs representing the interaction of the two effects. The heights of the boxcars are normalised to $1/t_r$ and $1/t_c$ respectively.

8.1.1 Shear wave energy

In this analysis only the displacements (and hence Fourier amplitudes) due to shear waves are considered. This is due to the relative energy – shear waves generally carry 96% of the earthquake energy. The energy carried in an elastic medium is proportional to the displacement squared. The displacements are related to shear wave speeds by Equations 8-6 and 8-7.

$$U_r \propto \frac{1}{C_p^{\,3}} \qquad \text{Equation 8-6}$$

$$U_\theta \propto \frac{1}{C_s^{\,3}} \qquad \text{Equation 8-7}$$

As well as this, if the approximation, $C_p \approx \sqrt{3}C_s$ is valid, the following is also true.

$$\frac{Amplitude\_of\_S\_wave}{Amplitude\_of\_P\_wave} = \frac{C_p^{\,3}}{C_s^{\,3}} = \sqrt{3}^3 = 5.2$$

Thus, the energy of S waves is $(5.2)^2 = 27$ times greater than the energy carried by P waves. The difference is so significant that only considering S waves in the analysis results in an adequate representation of the gross properties of the rupture.

The shear dislocation, represented by the force double couple, radiates energy anisotropically. The radiation pattern in the X_1-X_2 plane is presented in Equation 8-8, for P-waves, and Equation 8-9 for S-waves (Kasahara, 1981).

$$R_{\theta\phi} = \sin(2\theta) \qquad \text{Equation 8-8}$$

$$R_{\theta\phi} = \cos(2\theta) \qquad \text{Equation 8-9}$$

Where :

θ is the angle made with the principal axis (X_1) in the X_1-X_2 plane

$R_{\theta\phi}$ = Radiation pattern in the X_1-X_2 plane (varies from 0 to 1)

8.1.2 Fourier transform

The general form of the Fourier transform is defined as Equation 8-8. Here, g(t) is the displacement function u(t). The Fourier transform is therefore represented in Equation 8-9.

$$\Im\{g(t)\} = \int_{-\infty}^{\infty} e^{-i\omega t} g(t)dt \qquad \text{Equation 8-10}$$

$$\Im\{u(t)\} = \int_{-\infty}^{\infty} e^{-i\omega t} \frac{M_o(B(t;t_r) * B(t;t_c))}{4\pi\rho C_s{}^3 r} dt \qquad \text{Equation 8-11}$$

Convolution in Fourier transforms is resolved by simply multiplying the two Fourier transforms of the terms being convolved together. Boxcars generate Fourier terms of the form $\frac{\sin(\omega t/2)}{\omega t/2}$ (Lay and Wallace, 1995).

The Fourier amplitudes of the displacement function U_r are shown in Equation 8-12.

$$\left|\Im\{U_r(t)\}\right| = \frac{M_o \cos(2\theta)}{4\Pi\rho c_s{}^3 r} \left|\frac{\sin(\omega t_c(\theta)/2)}{\omega t_c(\theta)/2}\right| \left|\frac{\sin(\omega t_r/2)}{\omega t_r/2}\right| \qquad \text{Equation 8-12}$$

This is converted directly to a representation of Fourier amplitudes of acceleration by differentiating twice. The result is shown in Equation 8-13.

$$\left|\Im\{\ddot{U}_r(t)\}\right| = \frac{\omega^2 M_o \cos(2\theta)}{4\Pi\rho c_s{}^3 r} \left|\frac{\sin(\omega t_c(\theta)/2)}{\omega t_c(\theta)/2}\right| \left|\frac{\sin(\omega t_r/2)}{\omega t_r/2}\right| \qquad \text{Equation 8-13}$$

8.2 Application of source model

The source model developed in the previous section generates a Fourier amplitude and is dependent on a number of input parameters. Some parameters (M_o, C_s, V, t_r, ρ) are independent of the geometry and stay constant throughout the rupture. Other

parameters are are dynamic, and change over the course of the rupture, depending on the geometry of rupture and site. The variation of these variables is modelled using a numerical rather than an analytical approach, and is described below. The basis of the numerical analysis is the consideration of each 20m segment as a discrete slip surface with equal energy.

1. θ, r vary as the location of the rupture front moves relative to the site of interest. To model this, the fault is divided into small (20m) segments.
2. For each segment, a site-specific Fourier amplitude is calculated based on the distance between the segment and the source, and the direction of rupture relative to the site. This generates a Fourier amplitude that is dependent on the frequency selected.
3. The Fourier amplitudes generated in this way are averaged over the entire fault. In a later stage, each Fourier amplitude is divided into fault normal and fault parallel components, representing the assumed radiation pattern.

Table 8-1 shows the constants used in the model. The rupture velocities used in the model were selected based on the strong motion durations recorded at the Arthur's Pass and Flock Hill sites. The expected duration of ground motion at each site was based on the shear and rupture propagation velocities, and the source-site geometry. The velocities used in the model generated strong ground motion durations that were very close to those calculated at the two sites. The rupture propagation velocity is consistent with historic rupture velocities (Kasahara, 1981), while the crustal velocity agrees with published values (Robinson, 1986).

t_r	0.1	Seconds
M_o	10^6	Nm
V	2	km/s
C_s	3.25	km/s
ρ	2.1	t/m^3

Table 8-1 Constants used with model

t_r = Rise time

M_o = Moment magnitude

V = Rupture propagation velocity

C_s = Shear wave velocity in material

ρ = Material density

The rise time, 0.1 seconds, was selected arbitrarily at the time of model creation, is extremely short, and was selected to provide a larger proportion of high frequency components. This is a crude attempt to represent the variable progression of the rupture, and the subsequent high frequencies generated by short rise times. Abercrombie et al. (1998) calculated a rise time of between 5 and 6 seconds for the Arthur's Pass earthquake, but this information was not available at the time of modelling. A rise time of around 1.0 seconds is more common for events of this nature. Very low frequency terms are independent of the rise time, but the very short rise time will have an effect on medium and higher frequency terms. Despite these inaccuracies in some model input parameters, the model is used to compare intra-site and inter-site Fourier amplitudes.

The other parameters are independent of the geometery and are used in this analysis simply to scale the result (M_o was selected arbitrarily to allow direct comparison between sites of interest). Model outputs are used to compare relative amplitudes at and within sites, and so the absolute amplitudes generated are not analysed.

8.3 Model results

The relationship between the Fourier amplitudes calculated for the various sites can be seen in Figure 8-3. The Lake Coleridge site shows an extreme sensitivity to frequency variation. To a lesser extent, the Greymouth site exhibits some sensitivity to variations in frequency. The order of the amplitudes of calculated Fourier amplitudes at the four sites are consistent with their epicentral distance, as expected.

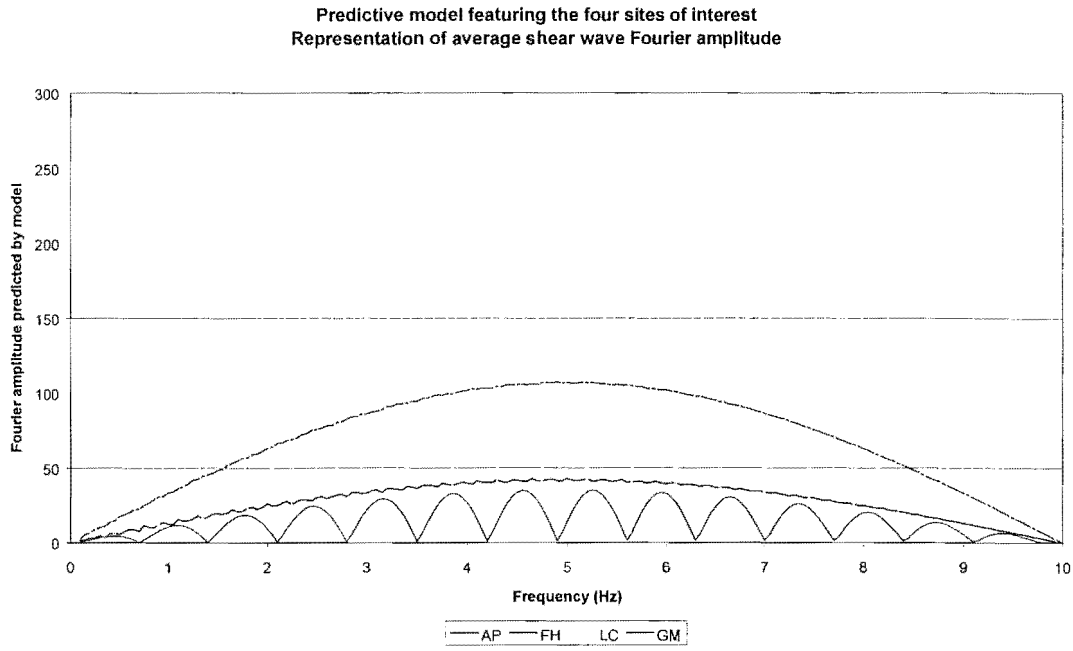

Figure 8-3 Fourier amplitudes at sites

The Lake Coleridge and Greymouth sites are located, respectively, almost directly in front of and behind the assumed rupture plane. The angle that they make with the moving rupture front does not change significantly. The frequency dependence of the Lake Coleridge and Greymouth sites are linked to the behaviour of the directional effects term representing the effect of fault movement in the rupture model.

Figure 8-4 shows the sensitivity of the predicted Fourier amplitude at sites to a variation in frequency, over the duration of the earthquake. Table 8-2 presents the variation of the directional effects term at two frequencies, 1Hz and 1.1Hz, over the angle range 0 to 1.2 radians, and this is depicted graphically in Figure 8-5.

The Greymouth site is largely unaffected by the change in frequency. The bearing from the moving fault rupture to the Greymouth site is relatively static. The bearing between the moving rupture and the Lake Coleridge site is also largely unchanged during the rupture, but, despite this, the frequency change results in a significantly different predicted Fourier amplitude. Differences in the predicted Fourier amplitude at the Arthur's Pass and Flock Hill results (as a result of the frequency change) are smaller, as these sites pass through different lobes of the directional effects term as the rupture front moves during the earthquake.

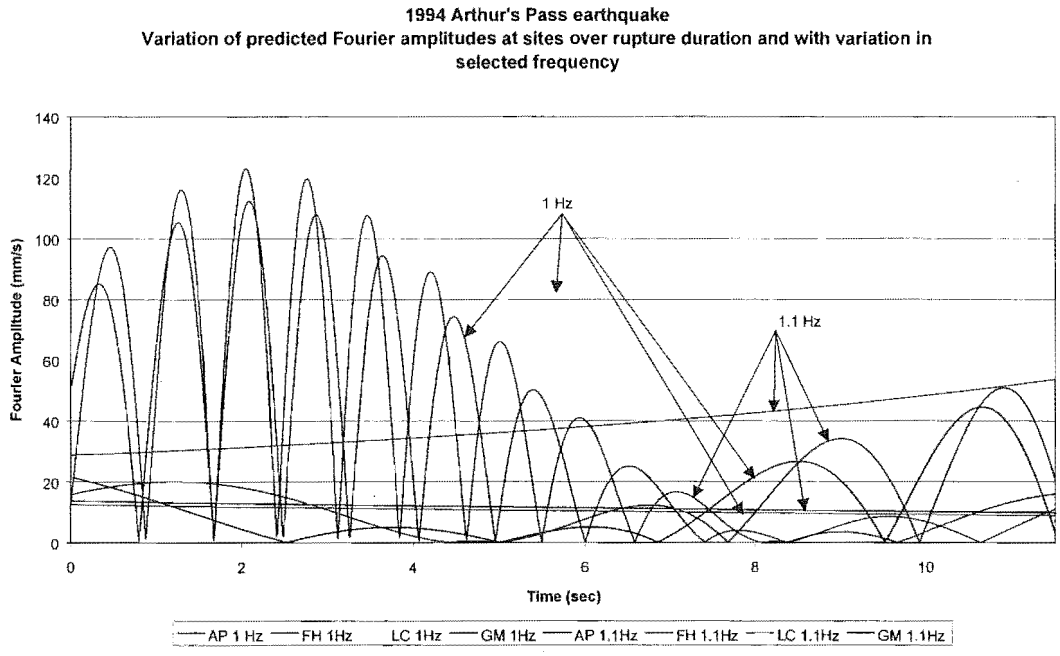

Figure 8-4 Effect of frequency change on predicted Fourier amplitude

Table 8-2, the variation of the directional effects term at various angles for the two frequencies considered, confirms the sensitivity of the directional effects term to frequency. At low angles, the directional effects term changes significantly from 1Hz to 1.1Hz. Larger angles are not affected as significantly, consistent with the results of Figure 8-4. Predicted Fourier amplitudes for the Lake Coleridge site, located almost directly in front of the rupture, are extremely sensitive to changes in frequency. This is consistent with the results presented in Table 8-2, and the sensitivity noted in Figure 8-3 is therefore attributed to the directional effects term. Conversely, the Greymouth site, located almost directly behind the rupture, is not as sensitive to frequency, which is consistent with the results presented in Figure 8-5.

θ (Radians)	1 Hz Avg	1.1 Hz Avg	% Difference
0.0-0.4	0.057	0.026	-54%
0.4-0.8	0.035	0.031	-11%
0.8-1.2	0.027	0.026	-04%

Table 8-2 Effect of frequency change on directivity effects term

The sensitivity of the directional effects term to frequency is highlighted in Figure 8-5, the amplitude of the directional effects term with varying radiation angle. At low frequencies (long periods), the directional effects term has a large amplitude, and a very large initial lobe. As the frequency increases, the amplitude of the directional effects term drops.

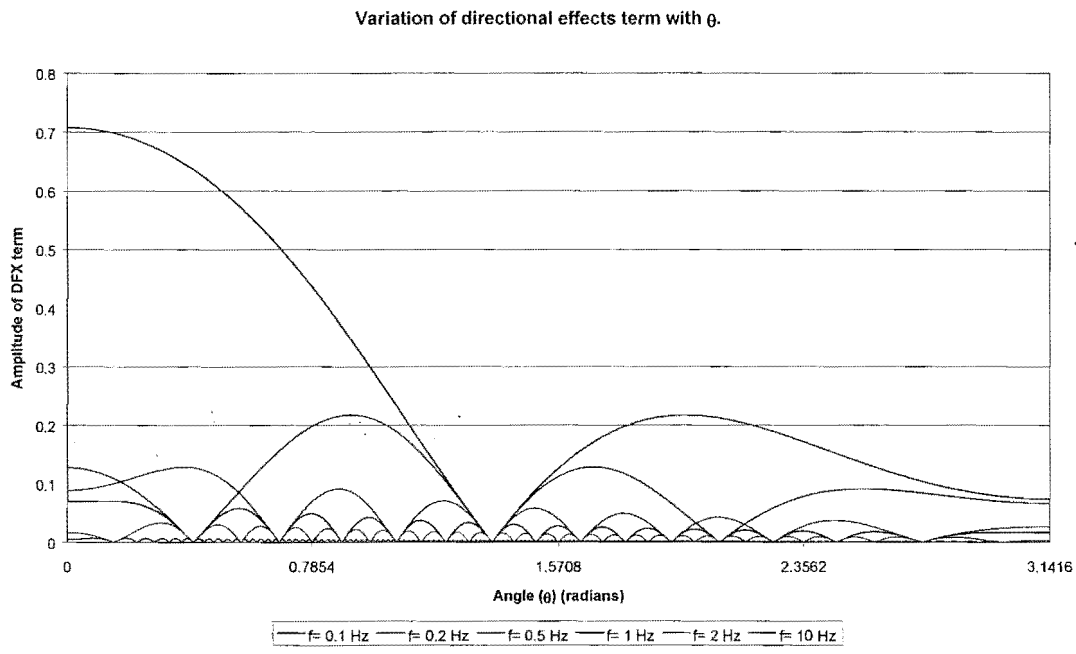

Figure 8-5 Model results at varying periods

8.3.1 Fault normal and fault parallel division

The polar radiation pattern for shear waves in the X_1-X_2 plane has been presented in section 8.1.1. The Fourier acceleration amplitudes radiate around the rupture in a similar fashion, and are transformed to fault normal and fault parallel components. The transformation method is presented graphically in Figure 8-6. This transformation is carried out for each location in the model, and comprises a vector transformation into fault normal and fault parallel components from a given direction. The direction from source to site varies during the rupture.

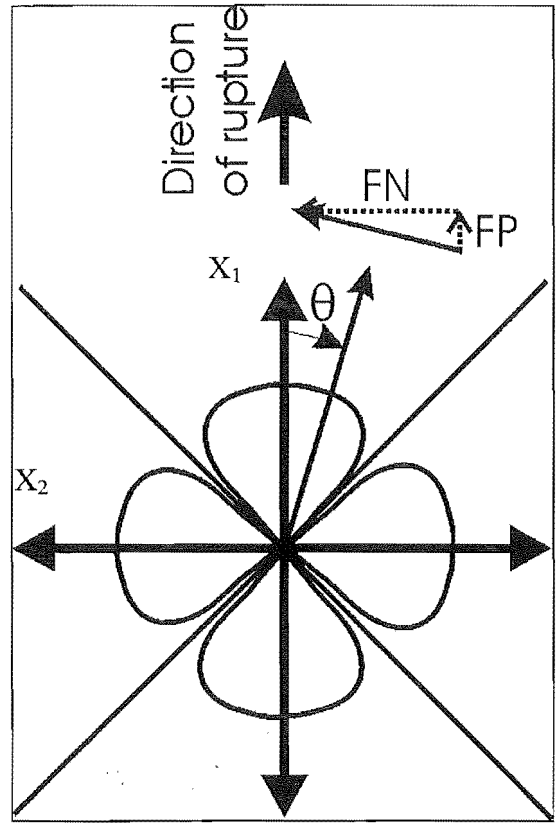

Figure 8-6 Plan view of shear wave radiation pattern in X_1-X_2 plane, and transformation to fault normal and fault parallel components.

Figure 8-7, fault normal and fault parallel Fourier amplitudes at sites plotted against frequency, shows that there is still significant frequency sensitivity in the Lake Coleridge and Greymouth results, consistent with the effect of the directional term. Figure 8-7 and Table 8-3 show that the Arthur's Pass site exhibits Fourier amplitudes that are larger in the fault parallel direction. This is consistent with the actual results recorded at the Arthur's Pass station. The Flock Hill results, on the other hand, do not agree with those predicted by the Fourier amplitude model. This disagreement could be due to the possible discrepancy between the assumed and the actual fault plane. Lake Coleridge exhibits a very large difference between the fault normal and fault parallel directions, consistent with what is observed on the scratch plate recorded there.

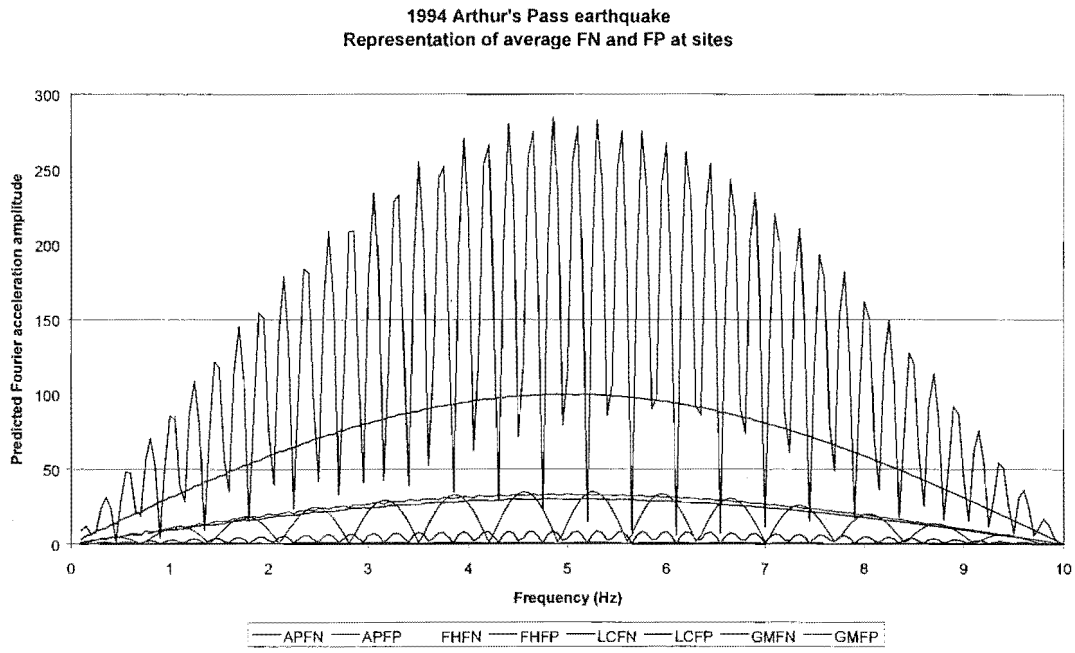

Figure 8-7 Fault normal and fault parallel Fourier amplitude at sites

	Calculated	Actual	Agreement
AP	FN < FP	FN < FP	Yes
FH	FN < FP	FN > FP	No
LC	FN >> FP	FN > FP	Yes

Table 8-3 Comparison of calculated and actual Fourier amplitudes

Figure 8-8 compares the actual Arthur's pass Fourier spectra with the predicted version generated by the model. The average of the predicted Fourier spectra was scaled to be the same as the average of the actual Fourier spectra. The two records have some similarities. The actual Arthur's Pass record shows a large peak between frequencies of 1.5 and 2.5 Hz, but exhibits a generally similar shape to the predicted results. The differences between the fault normal and fault parallel directions in the actual data are not as clear as those shown by the predicted Fourier amplitudes. The predicted fault normal Fourier amplitudes are generally less than those recorded, the fault parallel are generally larger than the actual.

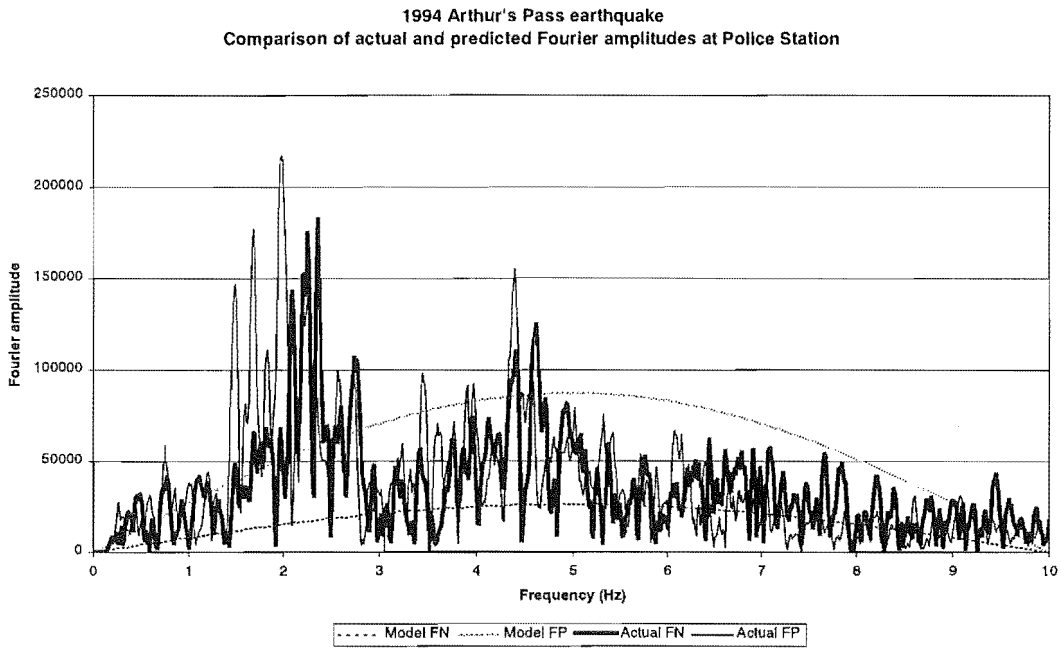

Figure 8-8 Arthur's Pass actual and predicted Fourier amplitudes

The actual and predicted Fourier amplitudes in the fault normal and fault parallel directions are shown in Figure 8-9. The shape of the actual Fourier amplitudes is generally larger than the predicted at lower frequencies, and smaller at high frequencies. This difference is probably due to the faster attenuation of the higher frequencies through material, an effect that is not considered in this model (Kramer, 1996). The short rise time, 0.1 seconds, used in the model has an effect on the felt influence at the site. The difference between the actual fault normal and fault parallel Fourier amplitudes is again not as large as the model predicts, an observation that was also true for the Arthur's Pass Fourier amplitudes.

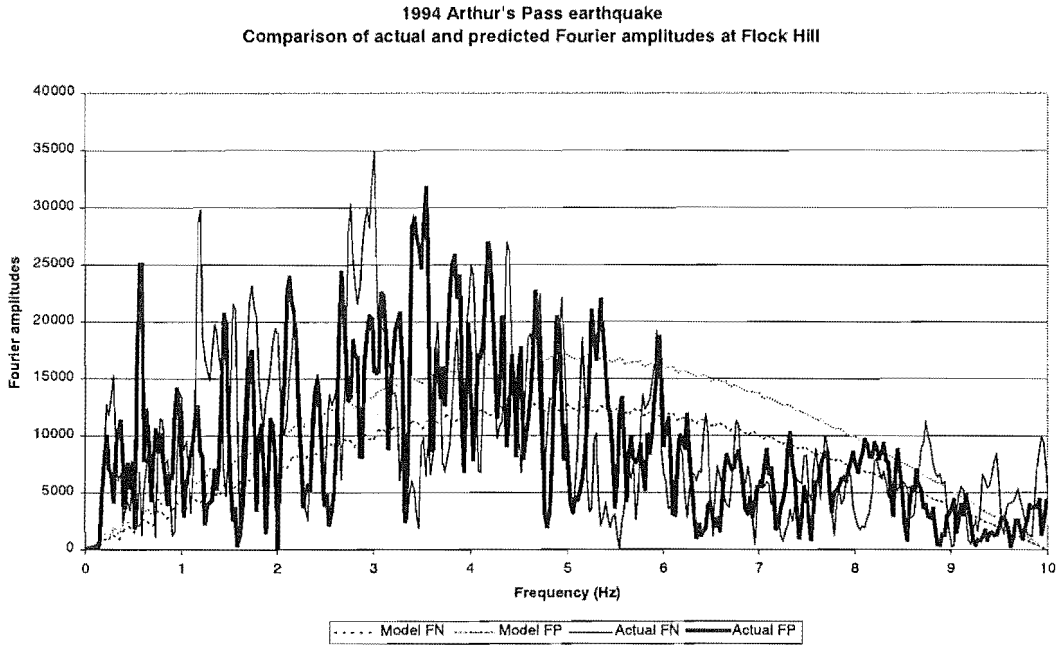

Figure 8-9 Flock Hill actual and predicted Fourier amplitudes

9 Conclusions

This thesis examined the anisotropy of strong ground motion records generated by the 1994 Arthur's Pass earthquake. Particular emphasis was placed on examining possible directivity effects in the near field. In order to achieve this, a fault plane was assumed, located along the spine of the aftershock pattern. The location of the assumed fault plane agreed with initial assessments of the rupture (Robinson et al., 1995, Arnadottir, 1995), and the earthquakes thought to be induced by the regional stress field (Robinson and McGinty, 1998), but disagreed with the revised results of Abercrombie et al. (1998).

The revised assessments of the rupture plane suggest that the assumed fault plane differed significantly from the actual fault plane. Despite this, some observations were consistent with directivity effects on the assumed fault plane. However, a number of observations were also inconsistent with results expected from a rupture on the assumed fault plane. Therefore, no conclusive evidence of directivity effects was identified at the sites considered in this analysis.

Analysis of the peak ground acceleration data set did not yield any evidence of directivity effects around the assumed fault plane. The Lake Coleridge scratch plate, located in the path of the assumed rupture, recorded a rectangular envelope of accelerations oriented in the assumed fault normal/fault parallel direction. Neither the direction, nor amplitude of the peak acceleration at the Lake Coleridge was consistent with the presence of forward rupture directivity effects that would be generated by the assumed faulting mechanism.

The Arthur's Pass Police Station recording showed higher intensities in the fault parallel direction than in the fault normal direction. Large fault parallel intensities were consistent with effects predicted by the far field Fourier amplitude model applied to the assumed fault plane. Current predictions of directivity effects are generally confined to an increase in intensities in the fault normal direction. The larger fault parallel intensities

may be significant, and could be considered, in the design of structures around known, active fault planes.

The Flock Hill site exhibited some properties that were consistent with expected forward rupture directivity effects from the assumed fault plane. The peak acceleration was in the fault normal direction, and located at the beginning of the strong motion record. However, the overall fault normal intensities were less than the fault parallel intensities, a result that was inconsistent with far field Fourier amplitudes predicted by the rupture model. The duration of strong ground motion at Flock Hill was less than that recorded at the Arthur's Pass Police Station, a result consistent with rupture propagation towards the southeast on the assumed fault plane.

Recordings from the Greymouth site were affected by a phenomenon that was not clearly identified in this thesis. These recordings were strongly anisotropic, and oriented in the fault normal direction. This pronounced anisotropy in the strong ground motion records was not attributed to fault geometry as the rupture was a significant distance from the site. The durations of the shore normal and shore parallel records at the site suggested that these results were consistent with the influence of the site geometry, but inconsistent with the peak parameters recorded at the site. It is therefore unlikely that the geometry of the surficial layers significantly influenced the anisotropy of the recorded ground motion.

A variant of the Haskell far field Fourier amplitude model was applied along the assumed rupture surface. Several results predicted by the model were consistent with the recorded results, despite possible inaccuracies in some input parameters. The model predicts a significantly larger fault parallel than fault normal response at the Arthur's Pass site. Existing models of directivity effects do not consider this amplification in the fault parallel direction when a site is located next to a fault surface, an intensification that can be significant in structural design.

There are clearly conflicting observations in this analysis. The conflicting results highlight the complex nature of strong ground motion analysis, and emphasize the need

for careful consideration of any conclusions drawn from the data set. Despite this qualifier, this thesis offers an analysis of strong ground motion generated by the Arthur's Pass earthquake, and an assessment of possible directivity effects around an assumed fault plane.

10 Reference List

Abercrombie, R E, Webb, T H, Robinson, R, McGinty, P J, Mori, J J , Beavan, R J, (1998) "The Enigma of the Arthur's Pass, New Zealand, Earthquake 1: Reconciling a Variety of Data for an Unusual Earthquake Sequence" in Robinson, R, Abercrombie, R E, Webb, T H, McGinty, P G, Arnadottir, T, Mori, J J, Beavan, R J, Reyners, M, (1998), "Seismotectonics of the Arthur's Pass earthquake of 18 June 1994", GNS Client Report 42655B July 1998

Abrahamson, N A, Silva, W J, (1997), "Empirical Response Spectral Acceleration Relations for Shallow Crustal Earthquakes", Seismological Research Letters Vol. 68, No. 1, January/February 1997, pp94-127

Archuleta, R, (1999), Lecture delivered in Geology Department, University of Canterbury, (August, 1999)

Arnadottir, T (1998), "Progress report from analysis of GPS data for the Earthquake Commission. December 1995" in Robinson, R, Abercrombie, R E, Webb, T H, McGinty, P G, Arnadottir, T, Mori, J J, Beavan, R J, Reyners, M, (1998) "Seismotectonics of the Arthur's Pass earthquake of 18 June 1994", GNS Client Report 42655B July 1998

Berrill, J B, (1975), "A study of high-frequency strong ground motion from the San Fernando earthquake", California Institute of Technology, Pasadena, California, 270p

Brune, J N, (1970), "Tectonic stress and the spectra of seismic shear waves from earthquakes", Journal of Geophysical research, Vol 75, pp 4997-5009

Cornell, C A, (1968), "Engineering seismic risk analysis", Bulletin of the Seismological Society of America, Vol. 58, pp 1583-1606

Cousins, W J, (1996), "Ground conditions at strong-motion recording sites in New Zealand", IGNS Report 96/33, 244p

Cousins, W J, Hefford, R T, Baguley, D E, O'Jane, S M, McVerry, G H, Porritt, T E, (1995), "Computer analyses of New Zealand earthquake accelerograms 9: the Arthur's Pass earthquake of 18 June 1994", Institute of Geological & Nuclear Science Report 95/32, 79p

Dowrick, D J, Rhoades, D A, (1999), "Attenuation of Modified Mercalli Intensity in the New Zealand Earthquakes", Bulletin of the New Zealand National Society for Earthquake Engineering, Vol 32, No 2, June 1999, pp55-89

IGNS study group, (1999), "Fault zone map", Personal communication, 1999, 2p

Kasahara, K, (1981), "Earthquake mechanics", Cambridge University Press, 248p

Kramer, S L, (1996), "Geotechnical Earthquake Engineering", Prentice-Hall Inc., 653p

Lay, T, Wallace, T C, (1995), "Modern Global Seismology", Academic Press, San Diego, California. 521p

Matuschka, T, Berryman, K R, O'Leary, A J, McVerry, G H, Mulholland, W M, Skinner, R I (1985), "New Zealand Seismic Hazard Analysis", Bulletin of the New Zealand National Society of Earthquake Engineering, Vol 18, No 4, pp313-322

McVerry, G H, Dowrick, Zhao, J X, (1995), "Attenuation of peak ground accelerations in New Zeland" Pacific Conference on Earthquake Engineering, Melbourne, 20-22 November, Vol. 2, pp 287-292

Peek, R, (1980), "Estimation of seismic risk for New Zealand : a seismicity model and preliminary design spectra", University of Canterbury, Civil Engineering Department, Research Report 80-21, 84p

Pettinga, J, (2000), Personal Communication

Robinson, R, (1986), "Seismicity, Structure and Tectonics of the Wellington Region, New Zealand", Geophysical Journal of the Royal Astronomical Society, Vol. 87, pp379-409

Robinson, R, McGinty, P J, (1998), "The Enigma of the Arthur's Pass, New Zealand, Earthquake, 2: The Aftershock Distribution and its Relation to Regional and Induced Stress Fields" in Robinson, R, Abercrombie, R E, Webb, T H, McGinty, P G, Arnadottir, T, Mori, J J, Beavan, R J, Reyners, M, (1998) "Seismotectonics of the Arthur's Pass earthquake of 18 June 1994", GNS Client Report 42655B July 1998

Robinson, R, Reyners, M, Webb, T, Arnadottir, T, Beavan, J, Cousins, J, Van Dissen, R, Pearson, C, (1995), "The M_w 6.7 Arthur's Pass Earthquake in the Southern Alps, New Zealand, June 18, 1994", Seismological Research Letters, Vol. 66, No. 2, March-April 1995, pp11-13

Smith, W D, Berryman, K R, (1983), "Revised estimates of earthquake hazard in New Zealand", Bulletin of the New Zealand National Society for Earthquake Engineering, Vol. 16, No. 4, December 1983

Smith, W D, (1995), "A Procedure for modelling near field earthquake intensities", Bulletin of the New Zealand National Society for Earthquake Engineering, Vol 28, No 3, September 1995

Somerville, P, (1996), "Forward rupture directivity in the Kobe and Northridge earthquakes, and implications for structural engineering", Proceedings of the International Workshop on Site Response subjected to Strong Earthquake Motions, Vol. 2, pp324-342

Somerville, P G, Smith, N F, Graves, R W, Abrahamson, N A, (1997), "Modification of Empirical Strong Ground Motion Attenuation Relations to Include the Amplitude and Duration Effects of Rupture Directivity", Seismological Research Letters, Vol 68, No. 1, January/February 1997, pp199- 222

Standards Association of New Zealand, (1992), "Code of practice for general structural design and design loadings of buildings : Metric units", New Zealand Standard 4203:1992

Stirling, M W, McVerry, G H, McGinty, P, (1999), Development of a new seismic hazard model for New Zealand", NZSEE Conference, Rotorua, March 1999, pp27-34

Van Dissen, R J, Berryman, K R, (1990), "Seismic hazard assessment of the Wellington-Hutt Valley segment of the Wellington Fault" New Zealand Geological Survey Client Report 90/24, 54p

Van Dissen, R J, Berryman, K R, Pettinga, J R, Hill, N L, (1992), Paleoseismicity of the Wellington-Hutt Valley segment of the Wellington Fault, North Island, New Zealand, New Zealand Journal of Geology & Geophysics, Vol 35, pp165-176, 1992

Yetton, M D, Wells, A, Traylen, N J, (1998), "The probability and consequences of the next Alpine Fault earthquake", EQC Research Report 95/193, March 1998, 161p

Appendix 1: Centroid-moment-tensor solutions

A number of different far-field Harvard Moment-Tensor solutions were calculated for the rupture event. Selected results are summarised below:

Results from:

1. Harvard
2. Iris
3. Seismological Research Letters
4. Abercrombie et al. (1998)

1: Source: *http://www.seismology.harvard.edu*

061894B SOUTH ISLAND, NEW ZEALAND

Date: 1994/ 6/18 Centroid Time: 3:25:25.2 GMT

Lat= -42.94 Lon= 171.47

Depth= 15.0 Half duration= 5.5

Centroid time minus hypocenter time: 5.7

Moment Tensor: Expo=26 0.710 0.270 -0.980 0.390 -0.260 -1.090

Mw = 6.7 mb = 6.2 Ms = 7.1 Scalar Moment = 1.45e+26

Fault plane: strike=68 dip=63 slip=150

Fault plane: strike=173 dip=64 slip=31

2: The ASCII version of the Harvard CMT (centroid-moment-tensor) solution follows.

Source:*http://www.iris.washington.edu/pub/CMT/MONTHLY/CMT_1994/CMT94.dek*

C061894B 06/18/94 03:25:19.5 -42.86 171.46 33.06.27.1SOUTH ISLAND, NEW ZEALAN↲

PDE BW:60156 45 MW:54118 135 DT= 5.7 0.1 -42.94 0.01 171.47 0.01 15.0 0.0↲

DUR 5.5 EX 26 0.71 0.01 0.27 0.01 -0.98 0.01 0.39 0.02 -0.26 0.03 -1.09 0.00↲

1.29 39 31 0.32 51 209 -1.61 1 300 1.45 68 63 150 173 64 31↲

The ASCII form is difficult to interpret. This form generates an earthquake strike of either 31° or 209°.

3: Source: Seismological Research Letters, Vol 66, Number 2 March-April 1995
June 18, 1994
03h25m15.8s, 42.96°S, 171.66°E, focal depth 14km from broadband displacement seismograms (GS). Some structural damage (VI) at Christchurch. Landslides blocked Highway 73 between Arthur's Pass and Christchurch. Felt throughout South Island and the southern part of the North Island. FOCAL MECHANISM from P-wave first motions is poorly controlled and corresponds to reverse faulting. The preferred fault plane is NP2. NP1: strike = 197°, dip = 60°, slip = 90°. NP2: strike = 17°, dip = 30°, slip = 90°. ...(report continues)...

4: Abercrombie et al. (1998) summarise 4 different body wave analyses. These analyses are presented in Table 1

Table 1

Source:	Strike	Dip	Rake
Harvard	173	64	31
NEIC	346	29	56
Zhang	351	82	56
Abercrombie et al.	221	47	112

Comment on all analyses:

Significantly different solutions were calculated by different organisations. The difference between the initially selected fault plane, along the backbone of the aftershocks, and the actual fault plane can be attributed to these conflicting solutions. It is worth noting that a significant period of study was required for a fault plane to be fixed that agreed with the observed aftershocks and stress drop.